STABILITY CHARACTERISTIC OF SUBSONIC BINARY AXISYMMETRIC COAXIAL JETS

Jhonatan Andrés Aguirre Manco

Doctorate Thesis of the Graduate Course in Engineering and Space Technology/Combustion and Propulsion, guided by Dr. Márcio Teixeira de Mendonça, approved in November 06, 2019.

URL of the original document:
<http://urlib.net/8JMKD3MGP3W34R/3UFNTF2>

INPE
São José dos Campos
2019

STABILITY CHARACTERISTIC OF SUBSONIC BINARY AXISYMMETRIC COAXIAL JETS

Jhonatan Andrés Aguirre Manco

Doctorate Thesis of the Graduate Course in Engineering and Space Technology/Combustion and Propulsion, guided by Dr. Márcio Teixeira de Mendonça, approved in November 06, 2019.

URL of the original document:
<http://urlib.net/8JMKD3MGP3W34R/3UFNTF2>

INPE

São José dos Campos

2019

Aluno (a): *Jhonatan Andres Aguirre Manco*

Título: **"STABILITY CHARACTERISTIC OF SUBSONIC BINARY AXISYMMETRIC COAXIAL JETS"**

em cumprimento ao requisito exigido para obtenção do Título de *Doutor(a)* em

Engenharia e Tecnologia Espaciais/Combustão e Propulsão
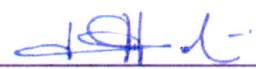
Dr.   Márcio Teixeira de Mendonça

Presidente / Orientador(a) / INPE / Cachoeira Paulista - SP

( ) *Participação por Video - Conferência*

(X) *Aprovado*   ( ) *Reprovado*

Dr.   Fernando Fachini Filho

Membro da Banca / INPE / Cachoeira Paulista - SP

( ) *Participação por Video - Conferência*

(X) *Aprovado*   ( ) *Reprovado*

Dr.   Roman Ivanovitch Savonov

Membro da Banca / INPE / Cachoeira Paulista - SP

( ) *Participação por Video - Conferência*

(X) *Aprovado*   ( ) *Reprovado*

Dr.   André Valdetaro Gomes Cavalieri

Convidado(a) / ITA / SJCampos - SP

( ) *Participação por Video - Conferência*

(X) *Aprovado*   ( ) *Reprovado*

Dr.   Leandro Franco de Souza

Convidado(a) / USP / São Carlos - SP

( ) *Participação por Video - Conferência*

(X) *Aprovado*   ( ) *Reprovado*

Este trabalho foi aprovado por:

( ) *maioria simples*

( ) *unanimidade*

São José dos Campos, 06 de novembro de 2019

I don't know anything, but I do know that everything is interesting if you go into
it deeply enough. " .

Richard Feynman

*A meus pais **Rafael** e **Maria**, à minha irmã **Sara**, à meu irmão **Juan Felipe** e à minha companheira de todos os dias **Liviany***

ACKNOWLEDGEMENTS

ABSTRACT

The performance of combustion systems in gas turbines and rocket engines depend strongly on the proper injection and mixing between fuel and oxidizer. The injection of propellants in these systems is performed using shear coaxial injectors that define the physical initial conditions for the combustion process. The hydrodynamic instabilities formed by the coaxial shear injector allow the mixing between the propellants through vorticity created by the instability of the shear layers. This work had as main objective the understanding of the stability characteristics of axisymmetric coaxial jets composed of different gases, specifically hydrogen and oxygen. To analyze the stability characteristics of coaxial binary jets the Linear Stability Theory (LST) and High Order Simulation (HOS) approaches were used. The LST has shown that the cases where the hydrogen was used as species in the inner jet $H_2 - O_2$ the amplification rates of Mode II are larger than the homogeneous coaxial jet, contrarily to what happens in $O_2 - H_2$ configuration. This agreed with the previous studies in a binary mixing layer, in which when the heavier species is in the lower velocity stream the amplification rates are larger, and vice versa. However For Mode I, the binary mixing layer results can not be extrapolated for a coaxial binary jet, once the confinement effect, caused by the finite quantity of species that can be placed in the inner jet, plays an important role. Using a low Mach number formulation, the compressible effects were neglected with the intention to show in the Less and Lin equation (compressible Rayleigh equation) where is the role of the species in the stability properties, which was called inertial effects. This formulation together with the compressible formulation also allows understanding the compressible effects caused by the different speed of sound of the species. Using High Order Simulations (HOS) of the Euler equation as second way to analyses the stability characteristics of coaxial binary jets, the main results of the LST were simulated in order to view different effects neglected by this theory, as: nonlinearities as modes interact, the used of realistic velocity and species profiles not based on canonical equations for the base flow and the visualization of the growth of the instabilities.

Keywords: Binary coaxial jets. Hydrodynamic stability. Euler equation. High order numerical simulation.

CARACTERÍSTICAS DE ESTABILIDADE DE JATOS COAXIAIS BINÁRIOS SUBSÔNICOS E AXISSIMÉTRICOS

RESUMO

O desempenho dos sistemas de combustão em turbinas a gás e motores foguete depende fortemente da injeção e mistura adequadas entre o combustível e o oxidante. A injeção dos propelentes nesses sistemas é realizada usando injetores coaxiais de cisalhamento, os quais definem as condições iniciais para o processo de combustão. As instabilidades hidrodinâmicas formadas pelo injetor de cisalhamento coaxial permitem a mistura entre os propelentes por meio da vorticidade gerada pela instabilidade das camadas de cisalhamento. Este trabalho tem como objetivo principal o entendimento das características de estabilidade de jatos coaxiais axissimétricos compostos por diferentes gases, especificamente hidrogênio e oxigênio. Para analisar as características de estabilidade dos jatos binários coaxiais, foram utilizadas as abordagens da Teoria da Estabilidade Linear (LST) e Simulação numérica de Alta Ordem (HOS). O LST mostrou que os casos em que o hidrogênio foi usado como espécie no jato interno H_2-O_2 as taxas de amplificação do Modo II são maiores que o jato coaxial homogêneo, ao contrário do que acontece na configuração do O_2-H_2. Isto concordou com os estudos anteriores realizados em camadas de mistura binária, nos quais quando as espécies mais pesadas estão na corrente de velocidade mais baixa, as taxas de amplificação são maiores e vice-versa. No entanto, no Modo I, os resultados da camada de mistura binária não podem ser extrapolados para um jato binário coaxial, uma vez que o efeito de confinamento, causado pela quantidade finita de espécies que podem ser colocadas no jato interno, desempenha um papel importante. Usando uma formulação de Mach baixo, os efeitos compressíveis foram desprezados com a intenção de mostrar na equação de Less e Lin (equação de Rayleigh compressível) onde está o papel das espécies nas características de estabilidade, chamados de efeitos inerciais. Esta formulação, juntamente com a formulação compressível, também permitiu compreender os efeitos compressíveis causados pelas diferentes velocidades do som das espécies. Utilizando simulações de alta ordem (HOS) das equações de Euler como segunda maneira de analisar as características de estabilidade de jatos binários coaxiais, foram simulados os principais resultados do LST para visualizar diferentes efeitos desprezados por essa teoria, como: não linearidades como a iteração entres os modos, o uso de um perfil de velocidade mais realista , perfis de espécies não baseados em equações canônicas para o escoamento base e a visualização do crescimento das instabilidades.

Palavras-chave: Jatos coaxiais binário. Estabilidade Hidrodinâmica. Equações de Euler. Simulação de alta ordem.

LIST OF FIGURES

xvi

xvii

LIST OF TABLES

CONTENTS

1 INTRODUCTION

The performance of combustion systems in gas turbines and rocket engines depends strongly on the proper injection and mixing between fuel and oxidizer. The injection of propellants in these systems is performed using shear coaxial injectors that define the physical initial conditions for the combustion process and are the most important initial conditions for the ignition behavior and the flame stability.

Figure 1.1 shows injection plate used in the main engine of the ARIANE 6, the newest launch vehicle designed by the ESA (European Space Agency) and the ARIANE group. This device is formed by multiple shear coaxial injectors, 122 in total, where each have the role of mixing the oxygen and the hydrogen. A sectional view of this kind of injector is presented in Figure 1.1b, which is used to mix liquid oxygen (LOX) and gaseous hydrogen (GH_2), both in the super critical state in the coaxial injector. Other rockets like the Vulcan, the engine of the space shuttle and the engine of the ARIANE 5 also used this kind of injector.

Figure 1.1 - Coaxial Shear Injector.

(a) Injector Plate, ARIANE 6. There are 122 shear coaxial injectors. Source: EOS GmbH
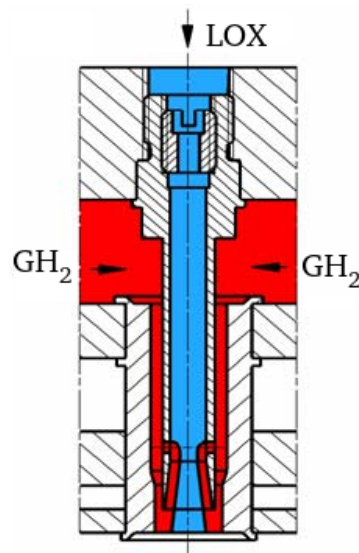
(b) Single shear coaxial injector(HAIDN, 2008)

The main objective of a shear coaxial injector is propellant atomization, a critical

condition to predict the combustor performance and stability. Besides, the size of the combustion chamber is determined by the length necessary to mix the fuel and the oxidizer.

The hydrodynamic instabilities formed by the coaxial shear injector allow the mixing between the propellants through vorticity, which is able to improve the mixing between reactants. This mixture process is outlined in Figure 1.2. Each species that leves the injector create a shear interface which is unstable to small perturbation. The disturbance on the shear layer, modifies the flow, as it flows over a wavy streamline creating regions of high and low pressure, a force inbalance, that is responsible for the increase in the magnitude of the initial small perturbation. The perturbation growth is noted as high vorticity structures, known as Kelvin-Helmholtz instability waves, which are the responsible for the mixing of the fuel and the oxidizer before the combustion process. This process of formation of the Kelvin-Helmholtz instabilities is known as Ackeret's explanation. However, the Kelvin-Helmholtz instabilities can cause disturbances in the heat release through oscillations in the flame front. The unsteady heat release and vortex paring excite acoustic modes that may resonate with the natural frequencies of the combustor leading to its destruction. The dynamics of the flow inside the combustor is related to acoustic, hydrodynamic and thermal disturbances.

Figure 1.2 - Mixing process between oxidizer and fuel in a shear coaxial injector produced by the Kelvin-Helmholtz instability.
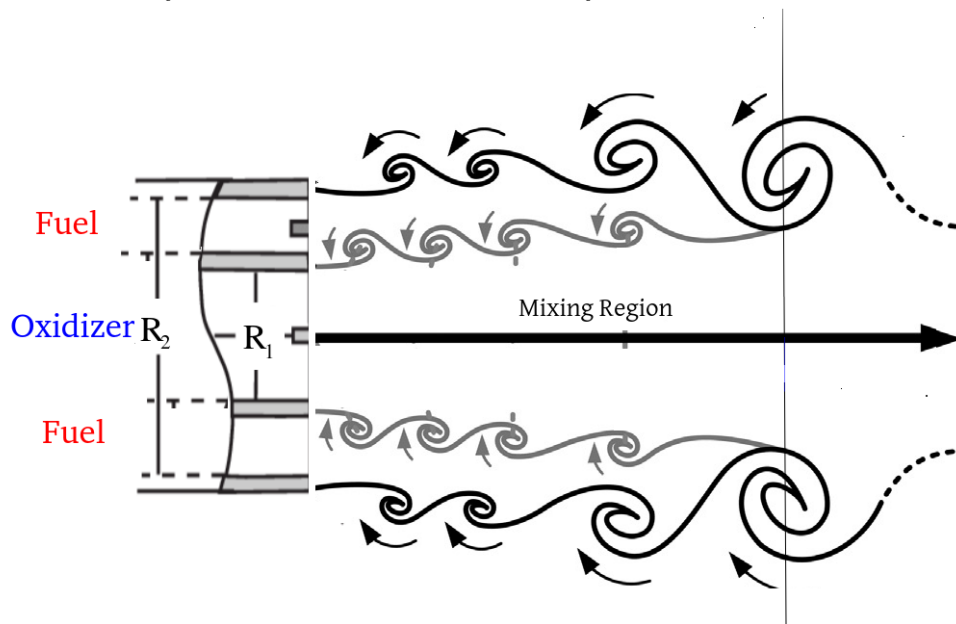
A stability analysis in this propulsive device furnishes the frequencies, phase velocity, group velocities, wavelengths and amplification rates of the disturbances that propagate inside the combustion chamber of a rocket engine. The study of these parameters aid to improve the mixing and can be used to avoid the destructive instabilities and to reduce the size of the combustion chamber.

The next chapter will present the main investigations related to linear stability analysis on the formation of the Kelvin-Helmholtz in a homogeneous gas coaxial configuration, as well as the works in binary gases using a mixing layer.

The study of linear stability analyses of binary gases using a coaxial configuration is the main objective of this work.

2 RELEVANT PREVIOUS RESEARCH

Experimental works presented by Schumaker and Driscoll (2007) and Schumaker and Driscoll (2012) evaluated the overall mixing efficiency using stoichiometic mixing length L_s, which is the distance over the jet axis where two fluids of different species have mixed in a defined concentration, for different velocity and radio ratios of the coaxial injectors using in a combustion chamber.

Other experimental investigation was made by Tani et al. (2015), who examined the geometric characteristics as the length, the taper angle and the wall thickness of the shear coaxial injector at super critical pressures.

Experiments are hard to setup and very expensive, therefore any effort to build a numerical tool that reproduce the processing of mixing of chemical species helps to understand the mixing process in high speed flows in combustors.

One of the first works describing the instability characteristics of incompressible coaxial jets using local inviscid liner stability analysis was presented by Talamelli and Gavarini (2006), however many works such as performed by Crow and Champagne (1971), Michalke (1984), and Monkewitz and SOHN (1988) had identified the main parameter involved in a single jet stability. In the work of Talamelli and Gavarini (2006) the role of the thickness of the duct wall that separates the stream of the same species was studied, as well as the velocity ratios. An absolute instability was found for a limited range of velocity ratios and thickness of the shear layer.

The more recent studies of coaxial jets stability characteristics address to the current necessity of the aerospace industry to reduce the noise of bypass jet engines, formed by a hot stream coming from the combustion chamber and a cold stream coming from the fan.

A linear stability analysis in inviscid and compressible coaxial jets with continuous velocity and temperature profile was performed by Perrault-Joncas and Maslowe (2008) focusing in shear flows with velocity and temperature similar to the exhaust of aircraft turbofan engines. This study investigated several factors that influence the stability of coaxial jets as: diameter radio and velocity radio between the primary and the second stream. Also it was interest in the difference in the results between 2D Bickley jet and axisymmetric coaxial jets.

Recently Gloor et al. (2013) published a study on the stability and acoustic characteristics of compressible viscous coaxial jets. The study investigated the parameters

that influence the development of hydrodynamic instabilities such as the Reynolds number, Mach number, momentum thickness. As Perrault-Joncas and Maslowe (2008), they studied the ration between the velocities and temperatures of the streams. Gloor et al. (2013) highlighted the importance of the acoustic modes, which are important for the study of the jet noise. This part of the study also allows to understand the possible iteration mechanisms between the Kelvin-Helmholtz instability and the acoustic modes. However for the study of the acoustic properties, an appropriated implementation of boundary condition was not evident. Gloor et al. (2013) did not implement far-field boundary conditions. When the acoustic is one of the problems to be addressed, the correct use of non-reflection boundary conditions is necessary to avoid spurious modes in the solution of the stability equation.

The latest investigation trying to analyze the stability characteristics for coaxial jets using spatial-temporal linear analysis is due to Balestra et al. (2015). That work explores the influence of the temperature and the velocity ratio to describe the process of transition between convective and global instability.

Binary shear layers like mixing layers were studied mainly by Kozusko et al. (1996b), due to the necessity to analyze experimental investigations. It was shown that the species that form the mixing layer have a significant effect on its growth rates, it is the density ratio, and can be more significant than compressibility. Kozusko et al. (1996b) qualified analytically the effects of density ratio, using different species, in the stability of a binary mixing layer and compared the results with a single gas or homogeneous mixing layer. The results of this work showed that the stability characteristics like the neutral modes, and the unstable modes are altered by the composition of the mixing layer produced by changing the molecular weight of the mixture. Further, the investigation conclude that when the heavier gas is on the slowest stream the growth rates are greater and evidence the opposite when the heavier gas in the fastest stream that growth rates are smaller.

Another conclusion of Kozusko et al. (1996a) works is on the importance of the model used to calculated the molecular properties and they recommended the use of the formulates from kinetic theory or use experimental values, instead of Chapman's and Sutherland's laws. This change considerably the growth rates and the range of unstable frequencies. They also explored variable properties in binary mixing layer, when nonconstant Lewis and Prandtl number are used.

A final conclusion of Kozusko et al. (1996b) is the insensibility of the growth rates to the convective Mach number (M_c) for binary mixing layer and they proposed

that once the stability characteristics for a binary mixing layer was determine in zero Mach number regime, the compressible effects can be predictable, decreasing the amplification rates as the convective Mach number increases. This is clear for $M_c < 1$. When the convective Mach number is juts greater than one, their effects determine the behavior of the compressible mixing layer.

A temporal linear stability analysis in a three dimensions compressible binary shear layer, as well as a direct numerical simulation was performed by Fedioun and Lardjane (2005). In this investigation density radios from 1 to 32 associated with different species at different temperatures are evaluated at high velocities, with M_c up to 2. The extreme cases evaluated were $O_2 - N_2$ and $O_2 - H_2$ for $M_c > 0.6$, with nearly the same maximum amplification factor but different most amplified wavelengths and phase velocity. This does not happen in lower convective Mach, when the system $O_2 - N_2$ present the maximum amplification factor, decreasing around 25% to 30% for the M_c range at the angle of propagation $\theta = 0$. Further an empirical model was development to predict the stability properties within 5% error starting with the incompressible solution as recomended by Kozusko et al. (1996b).

Salemi (2006), Salemi and Mendonca (2008) used linear hydrodynamic stability theory to study binary mixing layers in compressible flow, where the base flow was given by the similarity solution of the boundary layer equations.

Using linear stability theory and the direct numerical simulations Manco (2014), Manco et al. (2015) studied binary mixing layers stability modified by jets and wakes of different species. The vortical structures development of the resulting flow due to the interaction of mixing layers, jets and wakes is also considered in that study. In the results the stability characteristics are shown not only by the modification of jets and wakes of the base flow but also by the use of binary mixing layer formed by several species.

This thesis extends the study on coaxial jets of Perrault-Joncas and Maslowe (2008) in different aspects, (i) the base flow is now composed of two different chemical species in the inner and outer jets and ii) a direct numerical simulation is used to view the vortical structures development by instabilities.

3 GOALS AND OBJECTIVES

The thesis has as main objective the better understanding of the stability characteristics of the axisymmetric coaxial jet composed of two different gases, more specifically oxygen and hydrogen, in their mixing process.

The following specifics objectives are considered:

a) Study the stability characteristics of an axissymetric homogeneous coaxial jets when the radii ratio Γ and the velocity ratio r are modified using the inviscid Linear Stability Theory.

b) Study the stability characteristics of an axyssimetric coaxial jets formed by two species, oxygen and hydrogen, when the radii ratio Γ, the velocity ratio r and the position of the species are changed using the inviscid Linear Stability Theory.

c) Study the stability characteristics and observe the vortical structures of an axyssimetric homogeneous coaxial jets when the radii ratio Γ and the velocity ratio r are change using a High order numerical simulation.

d) Study the stability characteristics and observe the vortical structures of an axyssimetric coaxial jets formed by two species, oxygen and hydrogen, when the radii ratio Γ, the velocity ratio r and the position of the species are change using a High order numerical simulation.

Despite the fact that the stability characteristics that will be presented in this work concern only to gas mixture of oxygen and hydrogen present in rocket combustion chamber the main objective is to developments a tool to evaluate the mixing process between several gases.

4 FORMULATION

This chapter presents the mathematical model and used to describe a coaxial binary jets and discusses some of the physical aspects of the problem.

4.1 Conservation equations

To begin the mathematical formulation that represents a binary coaxial jet it is necessary to know what kind of equation will be used to modeled it. To this end an important dimensionless number is used. This number is known as the Knudsen number, Kn, defined as $Kn = \lambda/L$ where λ represents the mean free path of the molecules in the flow and L is a characteristics length representative to the problem. In the coaxial jet problem a characteristic length can be considered as the relation $L_s \equiv Z_0/R_0$, that as will be considered later, Z_0 is the spatial characteristic scale used to measured the axial direction of the coaxial jet and R_0 is spacial characteristic scale in radial direction. This relation, L_s also measure the slenderness of the coaxial jet.

If the coaxial jet is considered as a mixture of air, a Knudsen number of order of the unity is achieved when $L \approx 64nm$. In this study is a very small number in relation to the radii of the coaxial injectors used in rockets engines approximately of $5cm$. In conclusion, to study of a coaxial binary jets will be possible assume that the particles that composes it can be treat as continuous medium and therefore use the Navier-Stokes equation.

Being more specific the Navier-Stokes equation for compressible, thermally perfect gas with no heat addition and without externals forces will be used to model a coaxial binary jet.

In dimensional form the Navier-Stokes equation, represent by (˜) over the variables, are:

$$\frac{D\tilde{\rho}}{D\tilde{t}} + \tilde{\rho}\tilde{\nabla} \cdot \tilde{\mathbf{u}} = 0, \tag{4.1}$$

$$\tilde{\rho}\frac{\tilde{D}\tilde{Y}_i}{\tilde{D}\tilde{t}} = \tilde{\nabla} \cdot (\tilde{\rho}\tilde{\mathcal{D}}_{im}\tilde{\nabla}\tilde{Y}_i), \tag{4.2}$$

$$\tilde{\rho}\frac{\tilde{D}\tilde{\mathbf{u}}}{\tilde{D}\tilde{t}} = -\tilde{\nabla}\tilde{p} + \tilde{\nabla}\cdot\tilde{\boldsymbol{\tau}}, \tag{4.3}$$

and

$$\tilde{\rho}\frac{\tilde{D}\tilde{E}}{\tilde{D}\tilde{t}} = -\tilde{\nabla}\cdot(\tilde{p}\tilde{\mathbf{u}}) + \tilde{\nabla}\cdot(\tilde{\boldsymbol{\tau}}\cdot\tilde{\mathbf{u}}) + \tilde{\nabla}\cdot(\tilde{k}\tilde{\nabla}\tilde{T}) - \tilde{\nabla}\cdot\sum_i\tilde{\rho}_i\tilde{\mathbf{U}}_i\tilde{h}_i, \tag{4.4}$$

where $\tilde{D}\alpha/\tilde{D}\tilde{t} = \partial\alpha/\partial\tilde{t} + \tilde{\mathbf{u}}\cdot\tilde{\nabla}\alpha$ represent the total derivative, being α the density $\tilde{\rho}$, the velocity vector $\tilde{\mathbf{u}}$, the mass fraction $\tilde{Y}_i$ of a species i or the total energy $\tilde{E}$, the variables presented in the Navier-Stokes equations.

To know the state of gas mixture and gas species i, the ideal gas law was used for both, so that

$$\tilde{p} = \tilde{\rho}\tilde{R}\tilde{T} \quad \text{and} \quad \tilde{p}_i = \tilde{\rho}_i\tilde{R}_i\tilde{T}, \tag{4.5}$$

where $\tilde{p} = \sum\tilde{p}_i$, using the Dalton's law of the partial pressures.

The parameters $\tilde{k}$, $\tilde{\mathcal{D}}_i$ and $\tilde{\mu}$ represent the transport coefficient of heat, mass and momentum of the gas mixture that form the coaxial jet, which are function of the temperature $\tilde{T}$.

$\tilde{\mathcal{D}}_{im}$ the multicomponent diffusion coefficient of the species i in the gas mixture can be defined as

$$\tilde{\mathcal{D}}_{im} = (1 - X_i)\Big/\sum_j X_j\tilde{\mathcal{D}}_{ij}, \tag{4.6}$$

where the X_i is the mole fraction of species i and $\tilde{\mathcal{D}}_{ij}$ is the binary diffusion coefficient for the diffusion of species i into the species j.

The dynamic viscosity in the gas mixture is given by the Wilkes's rule

$$\tilde{\mu} = \sum_i\frac{X_i\tilde{\mu}_i}{\sum_j X_j\phi_{ij}}, \tag{4.7}$$

with

$$\phi_{ij} = \frac{1}{\sqrt{8}} \left(1 + \frac{\tilde{\mathcal{M}}_i}{\tilde{\mathcal{M}}_j} \right)^{1/2} \left[1 + \left(\frac{\tilde{\mu}_i}{\tilde{\mu}_j} \right)^{1/2} \left(\frac{\tilde{\mathcal{M}}_j}{\tilde{\mathcal{M}}_i} \right)^{1/4} \right]^2, \tag{4.8}$$

where $\tilde{\mu}_i$ is the dynamics coefficient for each species i in the gas mixture and $\mathcal{M}_i$ is the molecular weight of the species i.

In the same way and using the same rule, the thermal conductivity of the gas mixture is given by

$$\tilde{k} = \sum_i \frac{X_i \tilde{k}_i}{\sum_j X_j \phi_{ij}}, \tag{4.9}$$

with

$$\phi_{ij} = \frac{1}{\sqrt{8}} \left(1 + \frac{\tilde{\mathcal{M}}_i}{\tilde{\mathcal{M}}_j} \right)^{1/2} \left[1 + \left(\frac{\tilde{k}_i}{\tilde{k}_j} \right)^{1/2} \left(\frac{\tilde{\mathcal{M}}_j}{\tilde{\mathcal{M}}_i} \right)^{1/4} \right]^2. \tag{4.10}$$

The dimensional Stress Tensor $\tilde{\boldsymbol{\tau}}$ is defined as

$$\tilde{\boldsymbol{\tau}} = \tilde{\mu} \left(-\frac{2}{3} \boldsymbol{I} \tilde{\nabla} \cdot \tilde{\mathbf{u}} + \tilde{\nabla} \tilde{\mathbf{u}} + (\tilde{\nabla} \tilde{\mathbf{u}})^T \right). \tag{4.11}$$

The definition of the operations with $\tilde{\nabla}$ operator will be according to the problem of the coaxial jets, *i.e.* in cylindrical coordinates $(r\mathbf{e}_r, \theta\mathbf{e}_\theta, z\mathbf{e}_z)$. Using a vector $\boldsymbol{\alpha} = \alpha_1 \mathbf{e}_r + \alpha_2 \mathbf{e}_\theta + \alpha_3 \mathbf{e}_z$ and scalar α, the gradient and divergence operation can be defined as

$$\tilde{\nabla} \alpha = \frac{\partial \alpha}{\partial \tilde{r}} \mathbf{e}_r + \frac{1}{\tilde{r}} \frac{\partial \alpha}{\partial \tilde{\theta}} \mathbf{e}_\theta + \frac{\partial \alpha}{\partial \tilde{z}} \mathbf{e}_z \tag{4.12}$$

and

$$\tilde{\nabla} \cdot \boldsymbol{\alpha} = \frac{1}{\tilde{r}} \left[\frac{\partial (\tilde{r} \alpha_1)}{\partial \tilde{r}} + \frac{\partial \alpha_2}{\partial \tilde{\theta}} + \frac{\partial (\tilde{r} \alpha_3)}{\partial \tilde{z}} \right]. \tag{4.13}$$

In Appendix the mathematical operators used in cylindrical Navier-Stokes equations are defined.

4.1.1 Special form of the energy equation

In this work several forms of the energy equation will be used Kundu et al. (2015), in this section they are introduced.

Beginning with the total energy equation

$$\tilde{\rho}\frac{\tilde{D}\tilde{E}}{\tilde{D}\tilde{t}} = -\tilde{\nabla}\cdot(\tilde{p}\tilde{\mathbf{u}}) + \tilde{\nabla}\cdot(\tilde{\boldsymbol{\tau}}\cdot\tilde{\mathbf{u}}) + \tilde{\nabla}\cdot(\tilde{k}\tilde{\nabla}\tilde{T}) - \tilde{\nabla}\cdot\sum_i\tilde{\rho}_i\tilde{\mathbf{U}}_i\tilde{h}_i, \tag{4.14}$$

with

$$\tilde{\rho}\tilde{E} = \tilde{\rho}\tilde{e} + \tilde{\rho}\frac{1}{2}|\tilde{\mathbf{u}}|^2, \tag{4.15}$$

where $\tilde{e}$ is the internal energy per unit of mass per unit of volume and $|\tilde{\mathbf{u}}|^2/2$ is the kinetic energy per unit of mass and per unit of volume.

Using the enthalpy definition $\tilde{h} = \tilde{e} + \tilde{p}/\tilde{\rho}$, the energy equation is given by

$$\tilde{\rho}\frac{\tilde{D}\tilde{h}}{\tilde{D}\tilde{t}} = \tilde{\rho}\frac{\tilde{D}\tilde{E}}{\tilde{D}\tilde{t}} - \tilde{\rho}\frac{\tilde{D}\left(|\tilde{\mathbf{u}}|^2/2\right)}{\tilde{D}\tilde{t}} + \frac{\tilde{D}\tilde{p}}{\tilde{D}\tilde{t}} - \frac{\tilde{p}}{\tilde{\rho}}\frac{\tilde{D}\tilde{\rho}}{\tilde{D}\tilde{t}}. \tag{4.16}$$

The kinetic energy conservation equation can be obtained taking the dot product between the velocity vector $\tilde{\mathbf{u}}$ and the momentum equation 4.3

$$\tilde{\mathbf{u}}\cdot\tilde{\rho}\frac{\tilde{D}\tilde{\mathbf{u}}}{\tilde{D}\tilde{t}} = \tilde{\rho}\frac{\tilde{D}|\tilde{\mathbf{u}}|^2/2}{\tilde{D}\tilde{t}} = -\tilde{\mathbf{u}}\cdot\tilde{\nabla}\tilde{p} + \tilde{\mathbf{u}}\cdot(\tilde{\nabla}\cdot\tilde{\boldsymbol{\tau}}). \tag{4.17}$$

Then using it in 4.16, results

$$\tilde{\rho}\frac{\tilde{D}\tilde{h}}{\tilde{D}\tilde{t}} = -\frac{\tilde{p}}{\tilde{\rho}}\left(\tilde{\rho}\tilde{\nabla}\cdot\tilde{\mathbf{u}} + \frac{\tilde{D}\tilde{\rho}}{\tilde{D}\tilde{t}}\right) + \tilde{\boldsymbol{\tau}}:\tilde{\nabla}\tilde{\mathbf{u}} + \tilde{\nabla}\cdot(\tilde{k}\tilde{\nabla}\tilde{T}) + \frac{\tilde{D}\tilde{p}}{\tilde{D}\tilde{t}} - \tilde{\nabla}\cdot\sum_i\tilde{\rho}_i\tilde{U}_i\tilde{h}_i. \tag{4.18}$$

The terms in brackets can be recognized as the conservation of mass equation 4.1,

then

$$\tilde{\rho}\frac{\tilde{D}\tilde{h}}{\tilde{D}\tilde{t}} = \frac{\tilde{D}\tilde{p}}{\tilde{D}\tilde{t}} + \tilde{\boldsymbol{\tau}} : \tilde{\nabla}\tilde{\mathbf{u}} + \tilde{\nabla} \cdot (\tilde{k}\tilde{\nabla}\tilde{T}) - \tilde{\nabla} \cdot \sum_i \tilde{\rho}_i \tilde{U}_i \tilde{h}_i. \tag{4.19}$$

The diffusion velocity of species i, $\mathbf{U}_i$, is defined as

$$\tilde{\rho}_i \tilde{\mathbf{U}}_i = -\tilde{\rho}\tilde{\mathcal{D}}_{im}\tilde{\nabla}\tilde{Y}_i, \tag{4.20}$$

replacing it in the the enthalpy equation 4.19, results

$$\tilde{\rho}\frac{\tilde{D}\tilde{h}}{\tilde{D}\tilde{t}} = \frac{\tilde{D}\tilde{p}}{\tilde{D}\tilde{t}} + \tilde{\boldsymbol{\tau}} : \tilde{\nabla}\tilde{\mathbf{u}} + \tilde{\nabla} \cdot (\tilde{k}\tilde{\nabla}\tilde{T}) + \tilde{\nabla} \cdot \sum_i \tilde{\rho}\tilde{\mathcal{D}}_{im}\tilde{\nabla}\tilde{Y}_i \tilde{h}_i, \tag{4.21}$$

where $\tilde{h} = \sum_i \tilde{Y}_i \tilde{h}_i$ is the enthalpy of the gas mixture per unit of mass and $\tilde{h}_i$ is the enthalpy of the species i per unit of mass.

Another useful equation for the total enthalpy of the mixture shall allow arriving in a special form of energy equation in terms of the temperature, uses the definition of enthalpy in a gas mixture and applied to a control volume of fluid, results

$$\frac{\tilde{D}\tilde{h}}{\tilde{D}t} = \frac{\tilde{D}}{\tilde{D}t}\left(\sum_i \tilde{Y}_i \tilde{h}_i\right). \tag{4.22}$$

Remember that tilde (˜) over the variables indicate that these are dimensional. The definition of the mixture enthalpy for a thermally perfect gas is $d\tilde{h} = \tilde{c}_p d\tilde{T}$, applying it to the control volume of fluid results

$$\frac{\tilde{D}\tilde{h}}{\tilde{D}t} = \tilde{c}_p \frac{\tilde{D}\tilde{T}}{\tilde{D}t}, \tag{4.23}$$

using it and the derivative product rule in 4.22 results

$$\frac{\tilde{D}\tilde{h}}{\tilde{D}t} = \sum_i \left(\tilde{h}_i \frac{\tilde{D}\tilde{Y}_i}{\tilde{D}t} + \tilde{Y}_i \tilde{c}_{pi} \frac{\tilde{D}\tilde{T}}{\tilde{D}t}\right). \tag{4.24}$$

Now using the species conservation equation to eliminate $(\tilde{D}\tilde{Y}_i/\tilde{D}t)$

$$\tilde{\rho}\frac{\tilde{D}\tilde{h}}{\tilde{D}t} = \sum_i \left\{ \tilde{h}_i \tilde{\nabla} \cdot (\tilde{\rho}\tilde{\mathcal{D}}\tilde{\nabla}\tilde{Y}_i) + \tilde{\rho}\tilde{Y}_i\tilde{c}_{pi}\frac{\tilde{D}\tilde{T}}{\tilde{D}t} \right\}. \tag{4.25}$$

The energy equation for sensible enthalpy can be written as

$$\tilde{\rho}\frac{D\tilde{h}}{D\tilde{t}} = \frac{D\tilde{p}}{D\tilde{t}} + \tilde{\boldsymbol{\tau}} : \tilde{\nabla}\tilde{\mathbf{u}} + \tilde{\nabla} \cdot (\tilde{k}\tilde{\nabla}\tilde{T}) + \tilde{\nabla} \cdot \sum_i \tilde{\rho}\tilde{\mathcal{D}}_{im}\tilde{\nabla}\tilde{Y}_i\tilde{h}_i. \tag{4.26}$$

Subtracting 4.25 from above equation results

$$\frac{\tilde{D}\tilde{p}}{\tilde{D}\tilde{t}} + \tilde{\boldsymbol{\tau}} : \tilde{\nabla}\tilde{\mathbf{u}} + \tilde{\nabla} \cdot (\tilde{k}\tilde{\nabla}\tilde{T}) + \tilde{\nabla} \cdot \sum_i \tilde{\rho}\tilde{\mathcal{D}}_{im}\tilde{\nabla}\tilde{Y}_i\tilde{h}_i =$$
$$\sum_i \tilde{h}_i[\tilde{\nabla} \cdot (\tilde{\rho}\tilde{\mathcal{D}}_{im}\tilde{\nabla}\tilde{Y}_i)] + \sum_i \left(\tilde{\rho}\tilde{Y}_i\tilde{c}_{pi}\frac{\tilde{D}\tilde{T}}{\tilde{D}t} \right). \tag{4.27}$$

Using the conservation of species in the first term of the right hand side of the equation

$$\frac{\tilde{D}\tilde{p}}{\tilde{D}\tilde{t}} + \tilde{\boldsymbol{\tau}} : \tilde{\nabla}\tilde{\mathbf{u}} + \tilde{\nabla} \cdot (\tilde{k}\tilde{\nabla}\tilde{T}) + \tilde{\nabla} \cdot \sum_i \tilde{\rho}\tilde{\mathcal{D}}_{im}\tilde{\nabla}\tilde{Y}_i\tilde{h}_i = \tilde{\rho}\sum_i \left(\tilde{h}_i\frac{\tilde{D}\tilde{Y}_i}{\tilde{D}t} \right) + \tilde{\rho}\sum_i \left(\tilde{Y}_i\tilde{c}_{pi}\frac{\tilde{D}\tilde{T}}{\tilde{D}t} \right), \tag{4.28}$$

defining

$$\tilde{c}_{pf} \equiv \sum_i \tilde{Y}_i\tilde{c}_{pi},$$

as the frozen mixture specific heat. The term frozen refers to gas mixture without chemical reaction. This definition can be used in the above equation, resulting

$$\frac{\tilde{D}\tilde{p}}{\tilde{D}\tilde{t}} + \tilde{\boldsymbol{\tau}} : \tilde{\nabla}\tilde{\mathbf{u}} + \tilde{\nabla} \cdot (\tilde{k}\tilde{\nabla}\tilde{T}) + \tilde{\nabla} \cdot \sum_i \tilde{\rho}\tilde{\mathcal{D}}_{im}\tilde{\nabla}\tilde{Y}_i\tilde{h}_i = \tilde{\rho} \sum_i \left(\tilde{h}_i \frac{\tilde{D}\tilde{Y}_i}{\tilde{D}t} + \tilde{c}_{pf} \frac{\tilde{D}\tilde{T}}{\tilde{D}t} \right).$$

$$(4.29)$$

Applying distributive properties of the gradient to the third term of the left hand side of the equation and eliminating the equal terms, results

$$\tilde{\rho}\tilde{c}_{pf} \frac{\tilde{D}\tilde{T}}{\tilde{D}t} - \frac{D\tilde{p}}{\tilde{D}\tilde{t}} = \tilde{\boldsymbol{\tau}} : \tilde{\nabla}\tilde{\mathbf{u}} + \tilde{\nabla} \cdot (\tilde{k}\tilde{\nabla}\tilde{T}) + \sum_i \tilde{\rho}\tilde{\mathcal{D}}_{im}\tilde{\nabla}\tilde{Y}_i \cdot \tilde{\nabla}\tilde{h}_i. \qquad (4.30)$$

Using the chain rule for a total enthalpy derivative because the enthalpy is function only of the temperature, that meaning

$$\tilde{\nabla}\tilde{h}_i = \frac{\partial \tilde{h}_i}{\partial \tilde{T}}\tilde{\nabla}\tilde{T} = \frac{d\tilde{h}_i}{d\tilde{T}}\tilde{\nabla}\tilde{T} \qquad (4.31)$$

and using the definition for the species enthalpy $d\tilde{h}_i = \tilde{c}_{pi}d\tilde{T}$ results in a conservation energy equation in terns of the temperature

$$\tilde{\rho}\tilde{c}_{pf} \frac{\tilde{D}\tilde{T}}{\tilde{D}t} - \frac{\tilde{D}\tilde{p}}{\tilde{D}\tilde{t}} = \tilde{\boldsymbol{\tau}} : \tilde{\nabla}\tilde{\mathbf{u}} + \tilde{\nabla} \cdot (\tilde{k}\tilde{\nabla}\tilde{T}) + \sum_i \tilde{\rho}\tilde{\mathcal{D}}_{im}\tilde{\nabla}\tilde{Y}_i \cdot \left(\tilde{c}_{pi}\tilde{\nabla}T \right). \qquad (4.32)$$

This form of the energy equation is very useful because all the molecular properties are function of the temperature. Therefore, for problems with chemical species and chemical reaction it is widely used Law (2010).

4.1.1.1 Pressure form of the energy equation

Despite of the fact that the temperature energy equation is advantageous, a very useful form of the energy equation for aeroacustic is based on the pressure variable, being it the main characteristic of the sound waves, the changes of the pressure. Therefore once the temperature equation given for a perfect gas equation can be used to relate this quantities.

The perfect gas equation for a gas mixture is given by

$$\tilde{T} = \frac{\tilde{p}}{\tilde{\rho}\tilde{R}}, \tag{4.33}$$

where the mixture gas constant $\tilde{R}$ is

$$\tilde{R} = \sum_i Y_i \tilde{R}_i. \tag{4.34}$$

Applying it to the temperature energy conservation equation

$$\tilde{\rho}\tilde{c}_{pf}\tilde{p}\frac{\tilde{D}}{\tilde{D}t}\left(\frac{1}{\tilde{\rho}\tilde{R}}\right) + \left(\frac{\tilde{c}_{pf}}{\tilde{R}} - 1\right)\frac{\tilde{D}\tilde{p}}{\tilde{D}\tilde{t}} =$$
$$\boldsymbol{\tilde{\tau}} : \tilde{\nabla}\tilde{\mathbf{u}} + \tilde{\nabla}\cdot(\tilde{k}\tilde{\nabla}\tilde{T}) + \sum_i \tilde{\rho}\tilde{\mathcal{D}}_{im}\tilde{\nabla}\tilde{Y}_i \cdot \left(\tilde{c}_{pi}\tilde{\nabla}\left(\frac{\tilde{p}}{\tilde{\rho}\tilde{R}}\right)\right). \tag{4.35}$$

Now, using the definition of the mixture gas constant in terms of the specific heats, $\tilde{R} = \tilde{C}_p - \tilde{C}_v$ and the specific heat $\gamma = \tilde{C}_p/\tilde{C}_v$ ratio is possible to write an equation for pressure as

$$\frac{D\tilde{p}}{D\tilde{t}} - (\tilde{\gamma}-1)\tilde{c}_{pf}\frac{\tilde{p}}{\tilde{\rho}\tilde{R}^2}\frac{\tilde{D}(\tilde{\rho}\tilde{R})}{\tilde{D}t} = (\tilde{\gamma}-1)\boldsymbol{\tilde{\tau}} : \tilde{\nabla}\tilde{\mathbf{u}} + (\tilde{\gamma}-1)\tilde{\nabla}\cdot(\tilde{k}\tilde{\nabla}\tilde{T})+$$
$$(\tilde{\gamma}-1)\sum_i \tilde{\rho}\tilde{\mathcal{D}}_{im}\tilde{\nabla}\tilde{Y}_i \cdot \left(\tilde{c}_{pi}\tilde{\nabla}\left(\frac{\tilde{p}}{\tilde{\rho}\tilde{R}}\right)\right). \tag{4.36}$$

Opening the derivative of the second term of the r.h.s, so that

$$\frac{D\tilde{p}}{D\tilde{t}} - (\tilde{\gamma}-1)\tilde{c}_{pf}\frac{\tilde{p}}{\tilde{\rho}\tilde{R}}\frac{\tilde{D}\tilde{\rho}}{\tilde{D}t} - (\tilde{\gamma}-1)\tilde{c}_{pf}\frac{\tilde{p}}{\tilde{R}^2}\frac{\tilde{D}}{\tilde{D}t}\tilde{R} =$$
$$(\tilde{\gamma}-1)\boldsymbol{\tilde{\tau}} : \tilde{\nabla}\tilde{\mathbf{u}} + (\tilde{\gamma}-1)\tilde{\nabla}\cdot(\tilde{k}\tilde{\nabla}\tilde{T}) + (\tilde{\gamma}-1)\sum_i \tilde{\rho}\tilde{\mathcal{D}}_{im}\tilde{\nabla}\tilde{Y}_i \cdot \left(\tilde{c}_{pi}\tilde{\nabla}\left(\frac{\tilde{p}}{\tilde{\rho}\tilde{R}}\right)\right), \tag{4.37}$$

and using the conservation of mass equation to eliminate $\tilde{D}\tilde{\rho}/\tilde{D}\tilde{t}$,

$$\frac{\tilde{D}\tilde{p}}{\tilde{D}\tilde{t}} - \tilde{\gamma}\tilde{p}\tilde{\nabla}\cdot\mathbf{u} - \tilde{\gamma}\frac{\tilde{p}}{\tilde{R}}\frac{\tilde{D}\tilde{R}}{\tilde{D}t} = (\tilde{\gamma}-1)\tilde{\boldsymbol{\tau}} : \tilde{\nabla}\tilde{\mathbf{u}} + (\tilde{\gamma}-1)\tilde{\nabla}\cdot\left(\tilde{k}\tilde{\nabla}\frac{\tilde{p}}{\tilde{\rho}\tilde{R}}\right) +$$
$$(\tilde{\gamma}-1)\sum_i \tilde{\rho}\tilde{\mathcal{D}}_{im}\tilde{\nabla}\tilde{Y}_i \cdot \left(\tilde{c}_{pi}\tilde{\nabla}\left(\frac{\tilde{p}}{\tilde{\rho}\tilde{R}}\right)\right). \tag{4.38}$$

This expression for pressure is more advantageous when the viscous effects are negligible like will be in linear stability analysis because it allows the direct computation of the pressure field:

$$\frac{\tilde{D}\tilde{p}}{\tilde{D}\tilde{t}} + \tilde{\gamma}\tilde{p}\tilde{\nabla}\cdot\tilde{\mathbf{u}} = 0 \tag{4.39}$$

4.2 Linearized form of the conservation equations

In order to make a linear stability analysis of binary coaxial jets is necessary to get the linearized form of the Navier-Stokes equation. To this end perturbation theory is used. Later it is necessary to applied a normal mode solution to arrive the linear instability equations.

The first step on this way is to represent the instantaneous variables, which are present in the conservation equation 4.1 to 4.4, by an asymptotic series where the ϵ is a small parameter. The first approximation, known as the base flow, will be a function only of the radial variable $\tilde{r}$, as it represents a flow whose properties changed mainly in radial direction and where the changes in $\tilde{\theta}$ and $\tilde{z}$ direction are small and can be negligible. The second term of the series represents a correction to the base flow of order ϵ and represent the perturbation variables whose behavior define the stability properties of the flow.

In this stage the dimensionless variables are also defined. The reference density $\tilde{\rho}_0$, the species composition $\tilde{Y}_{i0}$, the transport coefficients $\tilde{\mu}_0$, $\tilde{k}_{i0}$, and the enthalpy of the inner gas $\tilde{h}_0$ are chosen with respect to the jet where the oxygen is located. The reference velocity will be the speed of sound in the oxygen stream a_0, because the acoustics perturbation are of interest.

To measure all the quantities with respect to the oxygen jet allows to have reference quantities that are most common in aerodynamics studies, wheres if the hydrogen

jet is used this quantities would appear strange due to the fact that a lower Mach number results. As example the speed of sound of the hydrogen at $273.15[K]$ is approximately $1290[m/s]$. For a jet of oxygen or hydrogen at the speed of $129[m/s]$ the Mach number will be $M = 0.1$ with respect to hydrogen speed of sound, compared to $M = 0.4$ in relation to the oxygen speed of sound, both at the same temperature.

Then, the non-dimensional variables are defined as

$$\rho(t, r, \theta, z) \equiv \frac{\tilde{\rho}(\tilde{r}, \theta, \tilde{z})}{\tilde{\rho}_0} = \bar{\rho}(r) + \epsilon \rho'(t, r, \theta, z), \tag{4.40}$$

$$\tilde{\mathbf{u}}(t, r, \theta, z) \equiv \frac{\tilde{\mathbf{u}}(\tilde{r}, \theta, \tilde{z})}{\tilde{a}_0} = \bar{\mathbf{u}}(r) + \epsilon \mathbf{u}'(t, r, \theta, z), \tag{4.41}$$

$$h(t, r, \theta, z) \equiv \frac{\tilde{h}(\tilde{r}, \theta, \tilde{z})}{\tilde{h}_0} = \bar{h}(r) + \epsilon h'(t, r, \theta, z), \tag{4.42}$$

$$T(t, r, \theta, z) \equiv \frac{\tilde{T}(\tilde{r}, \theta, \tilde{z})}{\tilde{T}_{0,r=0}} = \bar{T}(r) + \epsilon T'(t, r, \theta, z), \tag{4.43}$$

$$p(t, r, \theta, z) \equiv \frac{\tilde{p}(\tilde{r}, \theta, \tilde{z})}{\tilde{\rho}_0 \tilde{a}_0^2} = \bar{p}(r) + \epsilon p'(t, r, \theta, z), \tag{4.44}$$

where the independent dimensionless variables are defined as $t \equiv \tilde{t}/\tilde{t}_c$, $r \equiv \tilde{r}/\tilde{L}_0$, $z \equiv \tilde{z}/\tilde{L}_0$; $\tilde{t}_c$ is characteristic time usually obtained from the perturbation frequency or for the characteristic velocity at the reference length.

The transport coefficients are also dimensionless using a referents parameter taken from the oxygen stream, μ_0, k_0, R_0 c_{p0} and are function of the temperature T_0 measure at the center of the coaxial jet,

$$\mu \equiv \frac{\tilde{\mu}}{\mu_0} = \bar{\mu}(r) + \epsilon \mu'(t, r, \theta, z), \tag{4.45}$$

$$k \equiv \frac{\tilde{k}}{k_0} = \bar{k}(r) + \epsilon k'(t, r, \theta, z), \tag{4.46}$$

20

$$\gamma \equiv \frac{\gamma}{\gamma_0} = \gamma(r) + \epsilon\gamma'(t, r, \theta, z), \tag{4.47}$$

$$R \equiv \frac{\tilde{R}}{R_0} = \bar{R}(r) + \epsilon R'(t, r, \theta, z). \tag{4.48}$$

The completed non-dimensional Navier-Stokes equations are

$$\frac{D\rho}{Dt} + \rho\nabla \cdot \mathbf{u} = 0, \tag{4.49}$$

$$\rho\frac{DY_i}{Dt} = \frac{1}{Pe}\nabla \cdot (\rho\mathcal{D}_{im}\nabla Y_i), \tag{4.50}$$

$$\rho\frac{D\mathbf{u}}{Dt} = -\nabla p + \frac{1}{Re}\nabla \cdot \boldsymbol{\tau}, \tag{4.51}$$

$$\frac{Dp}{Dt} + \gamma_0\gamma p\left(\nabla \cdot \mathbf{u} - \frac{1}{R}\frac{DR}{Dt}\right) = (\gamma_0\gamma - 1)\frac{1}{Re}\boldsymbol{\tau} : \nabla\mathbf{u} + \gamma_j(\gamma_0\gamma - 1)\frac{1}{Pe}\nabla \cdot \left(k\nabla\left(\frac{p}{\rho R}\right)\right) +$$
$$\gamma_j(\gamma_0\gamma - 1)\frac{1}{Pe}\sum_i \mathcal{D}_{im}\rho\nabla Y_i \cdot \left(c_{pi}\nabla\left(\frac{p}{\rho R}\right)\right), \tag{4.52}$$

where Re is the Reynolds number, Pe is the Peclet number and γ is the relation between the specific heat c_{pf} and c_{vf}.

This dimensionless numbers are expressed by

$$Re = \frac{\rho_0 a_0 L_0}{\mu_0}, \quad Pe = \frac{L_0 a_0}{\alpha_0}, \quad D_{im} = \frac{\tilde{D}_{im}}{\alpha_0}, \quad \text{where} \quad \alpha_0 = \frac{k_0}{\rho_0 c_{p0}} \tag{4.53}$$

and

$$\gamma_j \equiv \frac{\gamma_0}{\gamma_0 - 1}. \tag{4.54}$$

21

The dimensionless state gas mixture equation is

$$p\gamma_0 = \rho RT. \tag{4.55}$$

The base flow equation of state is

$$\bar{p}\gamma_0 = \bar{\rho}R\bar{T}. \tag{4.56}$$

The base flow pressure is constant and to simplify the equation it is chosen as $\bar{p} = 1/\gamma_0$.

Then, the non-dimensional state equation results

$$\frac{1}{R\bar{T}} = \bar{\rho}. \tag{4.57}$$

According to the definition introduced in the equation 4.40 to 4.48 the dimensionless linearized form of the Navier-Stokes equation is obtained if only approximation of order ϵ is held, neglecting the high order terms. The perturbation of the transport coefficients, μ', k', γ', D'_{im} and the perturbation to the gas constant, R' are also negligible to simplify the problem. Finally, noting that a base flow satisfies the governing equations, then the conservation perturbation equations are given in its linear form by

$$\frac{\bar{D}\rho'}{\bar{D}t} + \frac{D'\bar{\rho}}{D't} + \bar{\rho}\nabla \cdot \mathbf{u}' + \rho'\nabla \cdot \bar{\mathbf{u}} = 0, \tag{4.58}$$

$$\bar{\rho}\frac{\bar{D}Y_i'}{\bar{D}t} + \bar{\rho}\frac{D'\bar{Y}_i}{D't} + \rho'\frac{\bar{D}\bar{Y}_i}{\bar{D}t} = \frac{1}{Pe}\nabla \cdot (\rho\mathcal{D}_{im}\nabla Y_i)', \tag{4.59}$$

$$\bar{\rho}\frac{\bar{D}\mathbf{u}'}{\bar{D}t} + \bar{\rho}\frac{D'\bar{\mathbf{u}}}{D't} + \rho'\frac{\bar{D}\bar{\mathbf{u}}}{\bar{D}t} = -\nabla p' + \frac{1}{Re}[\nabla \cdot \boldsymbol{\tau}]', \tag{4.60}$$

$$\frac{\bar{D}p'}{\bar{D}'t} + \frac{D'\bar{p}}{D't} + \gamma_0\gamma\bar{p}\left(\nabla\cdot\mathbf{u}' - \frac{1}{\bar{R}}\frac{D'\bar{R}}{D't} - \frac{1}{\bar{R}}\frac{\bar{D}R'}{\bar{D}t}\right) + \gamma_0\gamma p'\left(\nabla\cdot\bar{\mathbf{u}} - \frac{1}{\bar{R}}\frac{\bar{D}R}{\bar{D}t}\right) =$$
$$(\gamma_0\gamma - 1)\frac{1}{Re}\left[\gamma(\gamma-1)(\boldsymbol{\tau}:\nabla)\mathbf{u}\right]' + \gamma_j(\gamma_0\gamma - 1)\frac{1}{Pe}\left[\gamma\nabla\cdot(k\nabla T')\right] +$$
$$\left[\gamma_j(\gamma_0\gamma - 1)\frac{1}{Pe}\sum_i \mathcal{D}_{im}\rho\nabla Y_i\cdot\left(c_{pi}\nabla\left(\frac{p}{\rho R}\right)\right)\right]'.$$
(4.61)

The perturbation conservation equations 4.58 to 4.61, have a different definition for the material D/Dt, that was introduced in the previous section, being

$$\frac{\bar{D}}{\bar{D}t} = \frac{\partial(\ )}{\partial t} + \bar{\mathbf{u}}\cdot\nabla(\ ) \quad \text{and} \quad \frac{D'}{D't} = \mathbf{u}'\cdot\nabla(\ ). \tag{4.62}$$

The transport terms of order ϵ that appear in the above equation are given by:

$$\nabla\cdot(\rho\mathcal{D}_{im}\nabla Y_i)' = \nabla\cdot(\bar{\rho}\mathcal{D}_{im}\nabla Y_i' + \rho'\mathcal{D}_{im}\nabla\bar{Y}_i) \tag{4.63}$$

$$\left[\gamma_j(\gamma_0\gamma - 1)\frac{1}{Pe}\sum_i \rho\mathcal{D}_{im}\nabla Y_i\cdot\left(c_{pi}\nabla\left(\frac{p}{\rho R}\right)\right)\right]' =$$
$$\gamma_j(\gamma_0\gamma - 1)\frac{1}{Pe}\sum_i\left\{\mathcal{D}_{im}\left[\rho'\nabla\bar{Y}_i\cdot\left(c_{pi}\nabla\left(\frac{\bar{p}}{\bar{\rho}\bar{R}}\right)\right) + \bar{\rho}\nabla Y_i'\cdot\left(c_{pi}\nabla\left(\frac{\bar{p}}{\bar{\rho}\bar{R}}\right)\right) + \right.\right. \quad \text{(4.64)}$$
$$\left.\left.\bar{\rho}\nabla\bar{Y}_i\cdot\left(c_{pi}\nabla\left(\frac{\bar{p}'}{\bar{\rho}\bar{R}}\right)\right)\right]\right\},$$

$$[\nabla\cdot\boldsymbol{\tau}]' = \nabla\cdot\boldsymbol{\tau}'_{u'}, \tag{4.65}$$

$$[(\gamma_0\gamma - 1)\boldsymbol{\tau}:\nabla\mathbf{u}]' = (\gamma_0\gamma - 1)\left[\bar{\boldsymbol{\tau}}:\nabla\mathbf{u}' + \boldsymbol{\tau}'_{u'}:\nabla\bar{\mathbf{u}}\right], \tag{4.66}$$

where $\bar{\boldsymbol{\tau}}\equiv\boldsymbol{\tau}(\mu,\bar{\mathbf{u}})$ is the stress tensor evaluated in terms of μ and $\bar{\mathbf{u}}$, $\boldsymbol{\tau}'_{u'}\equiv\boldsymbol{\tau}(\mu,\mathbf{u}')$ is the stress tensor evaluated in μ and $\mathbf{u}'$.

4.3 Linear stability equations

In order to arrive to a simpler form of the systems of equation 4.58 to 4.61 and achieve the Liner Stability equations is necessary to use the hypothesis that the base flow of the coaxial jets behave like parallel flow, *i.e.*, the properties do not depend of the axial z and azimuthal θ direction, as the variation of properties in the radial direction the most important. Therefore, defining the base flow velocity as

$$\bar{\mathbf{u}} \equiv [0, 0, \bar{w}(r)], \tag{4.67}$$

where $\bar{w}$ is the component of the velocity in the axial direction and it is function only the radial coordinate.

With the parallel assumption for the base flow and taking it as steady and a constant pressure flow, a linear system for the perturbation variables can be obtained. Then the linear perturbation equation for inviscid, compressible, parallel base flow is given by

$$\frac{\bar{D}\rho'}{\bar{D}t} + \frac{D'\bar{\rho}}{D't} + \bar{\rho}\nabla \cdot \mathbf{u}' = 0, \tag{4.68}$$

$$\bar{\rho}\frac{\bar{D}Y_i'}{\bar{D}t} + \bar{\rho}\frac{D'\bar{Y}_i}{D't} + \rho'\frac{\bar{D}\bar{Y}_i}{\bar{D}t} = 0, \tag{4.69}$$

$$\bar{\rho}\frac{\bar{D}\mathbf{u}'}{\bar{D}t} + \bar{\rho}\frac{D'\bar{\mathbf{u}}}{D't} = -\nabla p', \tag{4.70}$$

$$\frac{\bar{D}p'}{\bar{D}t} + \gamma_0\gamma\bar{p}\left(\nabla \cdot \mathbf{u}' - \frac{1}{\bar{R}}\left(\frac{D'\bar{R}}{D't} + \frac{\bar{D}R'}{\bar{D}t}\right)\right) = 0. \tag{4.71}$$

In the above equations by the use of the parallel velocity assumption 4.67 the definition of the total derivative change, being

$$\frac{\bar{D}}{\bar{D}t} \equiv \frac{\partial}{\partial t} + \bar{w}\frac{\partial}{\partial z} \quad \text{and} \quad \frac{D'}{D't} \equiv \mathbf{u}' \cdot \nabla(\ ) \equiv u'\frac{\partial}{\partial r}. \tag{4.72}$$

24

It is important to note that the linear pressure equation involves total derivatives of the gas constant, in view of the use of different species for a coaxial jet. The Gas constant is function of the specific mass and is expressed in terms of disturbance variables as

$$R = \sum R_i Y_i = \sum R_i(\bar{Y}_i + Y_i') = \bar{R} + R'. \tag{4.73}$$

Using the species equation in linear form to invicid parallel flow

$$\frac{\bar{D}Y_i'}{\bar{D}t} + \frac{D'\bar{Y}_i}{D't} = 0, \tag{4.74}$$

is possible to find a conservation equation for the gas constant

$$\frac{\bar{D}}{\bar{D}t} \sum_{i=1}^n R_i Y_i' + \frac{D'}{D't} \sum_{i=1}^n R_i \bar{Y}_i = 0. \tag{4.75}$$

Now using the definition 4.73 the conservation equation for the gas constant is

$$\frac{\bar{D}}{\bar{D}t} R' + \frac{D'}{D't} \bar{R} = 0. \tag{4.76}$$

Is important to note the meaning of this equation, because its effects are very interesting

$$\frac{\partial R'}{\partial t} + \bar{W}\frac{\partial R'}{\partial z} + u'\frac{\partial \bar{R}}{\partial r} = 0. \tag{4.77}$$

The first two terms represent the convective part of the equation with only transport the perturbation caused by the species. The second term represent the inertial term cause by the distribution of the species in the base flow, as it will be treated in the linear stability results, being it one the effects that binary coaxial jets can have.

Using this conservation equation in the pressure perturbation energy equation results

$$\frac{\bar{D}p'}{\bar{D}t} + \gamma_0 \gamma \bar{p} \nabla \cdot \mathbf{u}' = 0. \tag{4.78}$$

Then, the linear system of equation for the perturbation variables can be combined in a single equation, known as Rayleigh equation for compressible flows, however the derivation of this equation using the Rayleigh methodology to compressible flow was made by Lees and Lin (1946). Thus in this work the compressible Rayleigh equation will be referenced as Less-Lin equation.

For the purposes of this work it is interesting to obtain the stability equation in terns of pressure. To obtain the pressure perturbation equation the divergence of the momentum equation is taken,

$$\nabla \cdot \left(\bar{\rho} \frac{\bar{D}\mathbf{u}'}{\bar{D}t} \right) + \nabla \cdot (\bar{\rho}(\mathbf{u}' \cdot \nabla)\bar{\mathbf{u}}) = -\nabla^2 p'. \tag{4.79}$$

This equation can be rearranged if noted that $\bar{\rho}$ is a constant to the linear operator $\bar{D}/\bar{D}t$ and by applying the divergence to the first term, so that

$$\frac{\bar{D}}{\bar{D}t} \nabla \cdot \bar{\rho}\mathbf{u}' + \nabla \bar{w} \cdot \frac{\partial}{\partial z}(\bar{\rho}\mathbf{u}') + \bar{\rho} + \nabla \cdot (\bar{\rho}(\mathbf{u}' \cdot \nabla)\bar{\mathbf{u}}) = -\nabla^2 p'. \tag{4.80}$$

Now, multiplying the linear pressure energy equation 4.71 by $\bar{\rho}/\gamma_0 \gamma \bar{p}$ and apply the operator $\bar{D}/\bar{D}t$ results

$$\frac{\bar{\rho}}{\gamma_0 \gamma \bar{p}} \frac{\bar{D}^2 p'}{\bar{D}t} + \bar{\rho}\frac{\bar{D}}{\bar{D}t}(\nabla \cdot \mathbf{u}') = 0. \tag{4.81}$$

The term $\bar{\rho}\nabla \cdot \mathbf{u}'$ can be seen as part of $\nabla \cdot (\bar{\rho}\mathbf{u}') = \bar{\rho}\nabla \cdot \mathbf{u}' + \nabla\bar{\rho} \cdot \mathbf{u}$ by the gradient product of a scalar field and vector, then

$$\frac{\bar{\rho}}{\gamma_0 \gamma \bar{p}} \left(\frac{\bar{D}p'}{\bar{D}t} \right)^2 + \frac{\bar{D}}{\bar{D}t}(\nabla \cdot (\bar{\rho}\mathbf{u}')) - \frac{\bar{D}}{\bar{D}t}(\nabla\bar{\rho} \cdot \mathbf{u}') - \frac{\bar{D}\bar{\rho}}{\bar{D}t} = 0. \tag{4.82}$$

Subtracting the above pressure modified equation for the momentum modified equa-

tion 4.80 to eliminate $\bar{D}(\bar{\rho}\mathbf{u}')/\bar{D}$,

$$\nabla \cdot (\bar{\rho}(\mathbf{u}' \cdot \nabla)\bar{\mathbf{u}}) + \nabla \bar{w} \cdot \frac{\partial}{\partial z}(\bar{\rho}\mathbf{u}') + \frac{\bar{D}}{\bar{D}t}\nabla \bar{\rho} \cdot \mathbf{u}' - \frac{\bar{\rho}}{\gamma_0 \gamma \bar{p}}\left(\frac{\bar{D}}{\bar{D}t}\right)^2 p' + \nabla^2 p' = 0. \quad (4.83)$$

Opening the first two terms and rearranging

$$\left(\left(\frac{\partial \bar{\rho}}{\partial r}\right)\frac{\bar{D}}{\bar{D}t} + 2\bar{\rho}\frac{\partial \bar{w}}{\partial r}\frac{\partial}{\partial z}\right)u' + \nabla \cdot \nabla p' - \frac{\bar{\rho}}{\gamma_0 \gamma \bar{p}}\left(\frac{\bar{D}}{\bar{D}t}\right)^2 p' = 0 \quad (4.84)$$

As the above equation is a function of p' and u' it is necessary to eliminate the radial velocity u'.

Applying the operator $\bar{D}/\bar{D}t$ to the last equation it can be written as

$$\left(\left(\frac{\partial \bar{\rho}}{\partial r}\right) + 2\bar{\rho}\frac{\partial \bar{w}}{\partial r}\frac{\partial}{\partial z}\right)\frac{\bar{D}u'}{\bar{D}t} + \frac{\bar{D}}{\bar{D}t}(\nabla \cdot \nabla p') - \frac{\bar{D}}{\bar{D}t}\left(\frac{\bar{\rho}}{\gamma_0 \gamma \bar{p}}\left(\frac{\bar{D}}{\bar{D}t}\right)^2 p'\right) = 0, \quad (4.85)$$

by the linearity of the operators.

Then, with the linear momentum equation 4.70 in the radial direction

$$\bar{\rho}\frac{\bar{D}u'}{Dt} = -\frac{\partial p'}{\partial r}, \quad (4.86)$$

and applying the particular operator

$$\left(\frac{\partial \bar{\rho}}{\partial r}\frac{\bar{D}}{\bar{D}t} + 2\bar{\rho}\frac{\partial \bar{w}}{\partial r}\frac{\partial}{\partial z}\right) \quad (4.87)$$

results

$$\left(\frac{\partial \bar{\rho}}{\partial r}\frac{\bar{D}}{\bar{D}t} + 2\bar{\rho}\frac{\partial \bar{w}}{\partial r}\frac{\partial}{\partial z}\right)\frac{\bar{D}u'}{Dt} = -\frac{1}{\bar{\rho}}\left(\frac{\partial \bar{\rho}}{\partial r}\frac{\bar{D}}{\bar{D}t} + 2\bar{\rho}\frac{\partial \bar{w}}{\partial r}\frac{\partial}{\partial z}\right)\frac{\partial p'}{\partial r}. \quad (4.88)$$

27

Subtracting it from the equation 4.85, a second order partial differential equation for the perturbation pressure p' is achieve

$$\frac{\bar{D}}{\bar{D}t}\left(\nabla^2 - \frac{\bar{\rho}}{\gamma_0\gamma\bar{p}}\left(\frac{\bar{D}}{\bar{D}t}\right)^2\right)p' - \left(\frac{1}{\bar{\rho}}\frac{\partial\bar{\rho}}{\partial r}\frac{\bar{D}}{\bar{D}t} + 2\frac{\partial\bar{w}}{\partial r}\frac{\partial}{\partial z}\right)\frac{\partial p'}{\partial r} = 0 \qquad (4.89)$$

The definition of the Laplace operator ∇^2 can be founded in the appendix the Appendix .

4.4 Local normal modal solution

The pressure perturbation and the other perturbation variables can be approximated using normal mode solution because of the linearity and the single dependence of the coefficient of the radial direction r. This allows the perturbation variables behavior like waves, where its amplitude depends exclusively of the radial coordinate r, with frequency ω, wave number k in axial direction z and n in azimuthal direction. On the whole will be the Linear Stability Theory that is going to say if this waves grow or decay in a coaxial jets.

To transform the partial pressure disturbances equation in a ordinary differential equation a wave solution of the form

$$p'(r,\theta,z,t) = \hat{p}(r)e^{i(kz+n\theta-\omega t)} + \hat{p}^*(r)e^{i(k^*z+n^*\theta-\omega^*t)} \qquad (4.90)$$

is used, where "*" represent the complex conjugate. In order to apply the above ansatz is enough to resolve only one part of the solution, because is easy to obtain its complex conjugate. To the other disturbance variables a similar ansatz is used.

Using the anzatz in the pressure disturbance equation 4.89, so that

$$\begin{aligned}(-i\omega + ik\bar{w})\left(\left(\frac{1}{r}\frac{d}{dr}\left(r\frac{d}{dr}\right) - \left(\frac{n^2}{r^2} + k^2\right)\right) - \frac{\bar{\rho}}{\gamma_0\gamma\bar{p}}(-i\omega + ik\bar{w})^2\right)\hat{p} - \\ \left(\frac{1}{\bar{\rho}}\frac{d\bar{\rho}}{dr}(-i\omega + ik\bar{w}) + 2ik\left(\frac{d\bar{w}}{dr}\right)\right)\frac{d\hat{p}}{dr} = 0,\end{aligned} \qquad (4.91)$$

and rearranging, results

$$\frac{d^2\hat{p}}{dr} + \left(\frac{1}{r} - \frac{1}{\bar{\rho}}\frac{d\bar{\rho}}{dr} - \frac{2}{(\bar{w}-c)}\left(\frac{d\bar{w}}{dr}\right)\right)\frac{d\hat{p}}{dr} + \left(k^2\left((\bar{w}-c)^2\frac{\bar{\rho}}{\gamma_0\gamma\bar{p}} - 1\right) - \left(\frac{n^2}{r^2}\right)\right)\hat{p} = 0.$$

$$(4.92)$$

The local non-dimensional sound velocity for the base flow is given by

$$a^2 = \frac{\tilde{a}^2}{a_0} = \gamma R\bar{T} \tag{4.93}$$

where a_0 is the speed of sound of the oxygen at the temperature T_0, and using the ideal gas equation for the base flow 4.56,

$$a^2 = \frac{\gamma}{\bar{\rho}}. \tag{4.94}$$

Defining $M_c \equiv (\bar{w} - c)/\bar{a}$, as the convective mach number, so that

$$\frac{d^2}{dr}\hat{p} + \left(\frac{d}{dr}\left(ln\left(\frac{r}{\gamma M_c^2}\right)\right)\right)\frac{d\hat{p}}{dr} + \left(k^2\left(M_c^2 - 1\right) - \left(\frac{n^2}{r^2}\right)\right)\hat{p} = 0, \tag{4.95}$$

simplified to axisymmetric coaxial jets, the above equation reduce to:

$$\frac{d^2\hat{p}}{dr^2} + \frac{d}{dr}\left(ln\left(\frac{r}{\gamma M_c^2}\right)\right)\frac{d\hat{p}}{dr} + k^2(M_c^2 - 1)\hat{p} = 0, \tag{4.96}$$

The convective Mach M_c is a important parameter to describe the compressible effects on the growth rate of unstable modes of a mixing layer.

4.4.1 Boundary condition

The boundary condition for the Less-Lin equation 4.95 can be defined if the coaxial jet is considered uniform in the symmetry axis and in the far-field, which mean that pronounced gradients of velocity, temperature, density and concentration of species are negligible.

To $r \rightarrow 0$ the equation turns

$$\frac{d^2\hat{p}}{dr^2} + \frac{1}{r}\frac{d\hat{p}}{dr} + \left(n_0 - \frac{n^2}{r^2}\right)\hat{p} = 0, \tag{4.97}$$

where $n_0 = \sqrt{k^2 - M_c^2}$ is the Convective Mach number relative to the waves velocity. This M_c is measure in relation to the axial velocity at center of the jet W_0 and the corresponding sound velocity. This equation is easily recognized as a Bessel equation, whose solution is given by

$$\hat{p} = AJ_n(n_0 r) + BY_n(n_0 r), \tag{4.98}$$

where J_n and Y_n are the Bessel function of order n of the first and second kind, respectively.

As the pressure must be bounded in the center of the coaxial jet, immediately the coefficient B must be zero, because the second kind Bessel function is infinite at origin, $r = 0$. The the solution results

$$\hat{p} = AJ_n(n_0 r). \tag{4.99}$$

To have an idea of the meaning of this solution an asymptotic approximation of the first kind Bessel function when its argument goes to infinity can be obtained, so that

$$J_n \approx \sqrt{\frac{2}{\pi r}} cos(r - n\pi/2 - \pi/4), \tag{4.100}$$

which together with the anzatz of normal modes solution 4.90 represent a standing waves. This waves oscillates in time but whose peaks amplitude profile do not move in space.

In the same way when $r \rightarrow \infty$ the equation 4.95 can be written

$$\frac{d^2\hat{p}}{dr^2} + \frac{1}{r}\frac{d\hat{p}}{dr} - \left(n_e + \frac{n^2}{r^2}\right)\hat{p} = 0, \tag{4.101}$$

where $n_e = \sqrt{M_c^2 - k^2}$ is the convective Mach number referenced with respect to the far field velocity W_e, with their respective sound velocity a_e. This ordinary differential equation is recognized as a modified Bessel equation, whose solutions is

$$\hat{p} = CI_n(n_e r) + DK_n(n_e r), \tag{4.102}$$

where I_n and K_n are the modified Bessel of order n of first and second kind, respectively. This function can be expressed as Bessel function of first J_n and third kind $H_n^{(1)}$, also known as a first order Hankel function. Being

$$I_n(r) = i^{-n} J_n(ir), \qquad K_n(r) = \frac{\pi}{2} i^{n+1} H_n^{(1)}(ir). \tag{4.103}$$

As the pressure must be bounded and can not increase indefinitely the constant of integration C must be zero, because the modified Bessel function I_n has an exponential growth behavior. This exponential behavior can be shown if the argument of the firs kind modified Bessel function I_n goes to infinity

$$I_n(\infty) \approx \frac{e^r}{\sqrt{2r}}. \tag{4.104}$$

The Hankel function of first specie $H_n^{(1)}$ also can be approximated asymptotically when its goes to infinity

$$H_n^{(1)}(\infty) \approx \sqrt{\frac{\pi}{2r}} e^{i(r - n\pi/2 - \pi/4)} \tag{4.105}$$

which together with the anzatz of normal modes solution 4.90 represents traveling outgoing waves (radiating modes, acoustics modes) or decaying waves, which are physically in agreement with this problem.

4.5   Waves solution of linear stability equation.

In order to shown that the inviscid stability equation 4.92 can be transformed in a generalized eigenvalue problem when its solutions are assumed in the form of waves, a normal mode approach is used.

To normal approach the ansatz

$$p'(r, \theta, z, t) = \Re\left\{\hat{p}(r)e^{i(kz+n\theta-\omega t)}\right\} \qquad (4.106)$$

is used, which depending the selection of its parameters defined what kind of stability analysis can be done, is used.

The wave number k and the frequency ω are complex number, represented by $k = k_r + ik_i$, $\omega = \omega_r + i\omega_i$.

A temporal growing of instability can be performed making $k_i = 0$, that allows pressure disturbances only to increase, decrease or be neutral in time, being periodic in space. Representing its behavior by the real part of $\Re(e^{i(-\omega_r+i\omega_i)t}) = e^{\omega_i t}$. So that, in a temporal stability analysis a coaxial jets is temporally unstable if exist $\omega_i > 0$.

In the same way, a spatial analysis of the stability of a coaxial jet is performed making $\omega_i = 0$, that allows that the pressure disturbances only to increased, decreased or be neutral in space, more specifically in the streamwise direction, being periodic in time. Representing its behavior by the real part of $\Re(e^{i(k_r+ik_i)t}) = e^{-k_i z}$. So that, in a spatial stability analysis a coaxial jets is spatially unstable if exist $k_i < 0$.

When both the k and ω are allowed to be complex numbers, with $k_i, \omega_i \neq 0$, the stability analysis define an absolute or a convective instabilities.

As was reported by Michalke (1984) and Morris (2010a) for circular jets and used by Perrault-Joncas and Maslowe (2008) and Gloor et al. (2013) for a coaxial jets, a spatial stability analysis is adequate for these flow, since the disturbances formed by the shear layer development in the space not in time.

To perform a spatial stability analysis it is necessary to rearrange the stability compressible equation in form of a generalized eigenvalue problem for the the k eigenvalues and the $\hat{p}$ eigenvectors as

$$\mathbf{A}\hat{\mathbf{p}} = \mathbf{B}k\hat{\mathbf{p}}, \qquad (4.107)$$

which will be solved using the QZ algorithm.

Expanding the term in Less-Lin equation 4.92 and rearrange, it can be written as

$$k^3 \left(\bar{w} - \frac{\bar{w}^3}{\bar{a}^2} \right) \hat{p} + k^2 \left(\frac{3\omega\bar{w}^2}{\bar{a}^2} - \omega \right) \hat{p} +$$

$$k \left(-\bar{w}\frac{d^2}{dr^2} - \bar{w}\frac{1}{r}\frac{d}{dr} + \bar{w}\frac{1}{\bar{\rho}}\frac{d\bar{\rho}}{dr}\frac{d}{dr} + 2 \left(\frac{d\bar{w}}{dr} \right) \frac{d}{dr} - \frac{3\omega^2\bar{w}}{\bar{a}^2} + \bar{w}\frac{n^2}{r^2} \right) \hat{p} + \quad (4.108)$$

$$\left(\omega\frac{d^2}{dr^2} + \omega\frac{1}{r}\frac{d}{dr} - \omega\frac{1}{\bar{\rho}}\frac{d\bar{\rho}}{dr}\frac{d}{dr} + \frac{\omega^3}{\bar{a}^2} - \omega\frac{n^2}{r^2} \right) \hat{p} = 0.$$

This is explicitly a eigenvalue problem for k and the eigenfunction $\hat{p}$. Using $\mathcal{D} = d/dr$ and $\mathcal{D}^2 = d^2/d^2r$ to represent the first and second derivative respectively and defining

$$R_1 \equiv \bar{w} - \frac{\bar{w}^3}{\bar{a}^2}, \quad (4.109)$$

$$L_{q_2} \equiv \omega - \frac{3\omega\bar{w}^2}{\bar{a}^2}, \quad (4.110)$$

$$L_{q_1} \equiv -\bar{w}\mathcal{D}^2 - \bar{w}\frac{1}{r}\mathcal{D} + \bar{w}\frac{1}{\bar{\rho}}\frac{d\bar{\rho}}{dr}\mathcal{D} + 2 \left(\frac{d\bar{w}}{dr} \right) \mathcal{D} - \frac{3\omega^2\bar{w}}{\bar{a}^2} + \bar{w}\frac{n^2}{r^2}, \quad (4.111)$$

$$L_p \equiv \omega\mathcal{D}^2 + \omega\frac{1}{r}\mathcal{D} - \omega\frac{1}{\bar{\rho}}\frac{d\bar{\rho}}{dr}\mathcal{D} + \frac{\omega^3}{\bar{a}^2} - \omega\frac{n^2}{r^2}. \quad (4.112)$$

Then,

$$k^3 R_1 \hat{p} + k^2 L_{q_2} \hat{p} + k L_{q_1} \hat{p} + L_p \hat{p} = 0. \quad (4.113)$$

This is a non-linear eigenvalue problem, where the eigenvalue k appears in a polynomial form. In order to transform it in a linear eigenvalue problem a change of variable may be used Morris (2010b), defining

$$q_1 \equiv k\hat{p} \qquad \text{and} \qquad q_2 \equiv kq_1, \quad (4.114)$$

the polynomial eigenvalue problem results

$$kR_1q_2 + L_{q_2}q_2 + L_{q_1}q_1 + L_{\hat{p}} = 0. \tag{4.115}$$

This system can be written in matrix form

$$\begin{bmatrix} -L_{q_1} & -L_{q_2} & -L_p \\ 1 & 0 & 0 \\ 0 & 1 & 0 \end{bmatrix} \begin{bmatrix} q_1 \\ q_2 \\ \hat{p} \end{bmatrix} = k \begin{bmatrix} 0 & R_1 & 0 \\ 0 & 0 & 1 \\ 1 & 0 & 0 \end{bmatrix} \begin{bmatrix} q_1 \\ q_2 \\ \hat{p} \end{bmatrix}. \tag{4.116}$$

or

$$\mathbf{L}\hat{\mathbf{q}} = k\mathbf{R}\hat{\mathbf{q}}, \tag{4.117}$$

with $\mathbf{L}$ and $\mathbf{R}$ being the matrices in left and right side of the equation 4.116 and $\mathbf{q}$ the eigenvector, where one of their components is the eigenfunction $\hat{p}$.

4.5.1 Navier-Stokes generalized eigenvalue problem

A solution using normal mode approach in form of traveling waves can be imposed, using the ansatz 4.90 on the linear Navier Stokes equations 4.58 to 4.61.

Therefore the linear Navier-Stokes in the Fourier space is expressed as

$$-i\omega\hat{\mathbf{u}} + \mathbf{A}\frac{\partial\hat{\mathbf{u}}}{\partial r} + ik\mathbf{B}\hat{\mathbf{u}} + \mathbf{C}\hat{\mathbf{u}} - \frac{1}{Re}\left(\mathbf{D}\frac{\partial^2\hat{\mathbf{u}}}{\partial r^2} - k^2\mathbf{E}\hat{\mathbf{u}} + ik\mathbf{F}\frac{\partial\hat{\mathbf{u}}}{\partial r} + \mathbf{G}\frac{\partial\hat{\mathbf{u}}}{\partial r} + ik\mathbf{H}\hat{\mathbf{u}} + \mathbf{I}\hat{\mathbf{u}}\right) -$$
$$\frac{\gamma_0\gamma - 1}{Re}\left(\mathbf{L}\frac{\partial\hat{\mathbf{u}}}{\partial r} + ik\mathbf{M}\hat{\mathbf{u}}\right) + \frac{\gamma_j(\gamma_0\gamma - 1)}{Pe}\left(\mathbf{O}\frac{\partial^2\hat{\mathbf{u}}}{\partial r^2} - k^2\mathbf{P}\hat{\mathbf{u}} + \mathbf{Q}\frac{\partial\hat{\mathbf{u}}}{\partial r} + \mathbf{S}\hat{\mathbf{u}}\right) -$$
$$\frac{1}{Pe}\left(\mathbf{T}\frac{\partial^2\hat{\mathbf{u}}}{\partial r^2} - k^2\mathbf{U}\hat{\mathbf{u}} + \mathbf{V}\frac{\partial\hat{\mathbf{u}}}{\partial r} + \mathbf{X}\hat{\mathbf{u}}\right) = 0. \tag{4.118}$$

The definition of the matrices used are given in appendix .

The derivatives with respect to r can be expressed by the operator

$$\frac{\partial \hat{\mathbf{u}}}{\partial r} = \mathcal{D}\hat{\mathbf{u}} \qquad \text{and} \qquad \frac{\partial^2 \hat{\mathbf{u}}}{\partial r^2} = \mathcal{D}^2\hat{\mathbf{u}}. \tag{4.119}$$

This system of equation can be recognized as generalized eigenvalued problem. To do it, the equation can be rearranged as

$$k^2 \left(\frac{1}{\bar{\rho}Re_0}\mathbf{E} + \frac{\gamma_j(\gamma_0\gamma - 1)}{Pe}\mathbf{P} + \frac{1}{Pe}\mathbf{U} \right)\hat{\mathbf{u}} + ik\left(\mathbf{B} - \frac{1}{Re}(\mathbf{F}\mathcal{D} + \mathbf{H}) - \frac{\gamma_0\gamma - 1}{Re}\mathbf{M} \right)\hat{\mathbf{u}} +$$
$$\left[-i\omega + \mathbf{A}\mathcal{D} + \mathbf{C} - \frac{1}{\bar{\rho}Re}\left(\mathbf{D}\mathcal{D}^2 + \mathbf{G}\mathcal{D} + \mathbf{I} \right) - \frac{\gamma_0\gamma - 1}{Re}\mathbf{L}\mathcal{D} - \right.$$
$$\left. \frac{\gamma_j(\gamma_0\gamma - 1)}{Pe}\left(\mathbf{O}\mathcal{D}^2 + \mathbf{Q}\mathcal{D} + \mathbf{S} \right) - \frac{1}{Pe}\left(\mathbf{T}\mathcal{D}^2 + \mathbf{V}\mathcal{D} + \mathbf{X} \right) \right]\hat{\mathbf{u}} = 0, \tag{4.120}$$

and defining

$$\mathbf{A_2} = \frac{1}{\bar{\rho}Re}\mathbf{E} + \frac{\gamma_j(\gamma_0\gamma - 1)}{Pe}\mathbf{P} + \frac{1}{Pe}\mathbf{U} \tag{4.121}$$

$$\mathbf{A_1} = i\left(\mathbf{B} - \frac{1}{\bar{\rho}Re}(\mathbf{F}\mathcal{D} + \mathbf{H}) - \frac{\gamma_0\gamma - 1}{Re}\mathbf{M} \right) \tag{4.122}$$

$$\mathbf{A_0} = -i\omega + \mathbf{A}\mathcal{D} + \mathbf{C} - \frac{1}{\bar{\rho}Re}\left(\mathbf{D}\mathcal{D}^2 + \mathbf{G}\mathcal{D} + \mathbf{I} \right)$$
$$-\frac{\gamma_0\gamma - 1}{Re}\mathbf{L}\mathcal{D} - \frac{\gamma_j(\gamma_0\gamma - 1)}{Pe}\left(\mathbf{O}\mathcal{D}^2 + \mathbf{Q}\mathcal{D} + \mathbf{S} \right) - \frac{1}{Pe}\left(\mathbf{T}\mathcal{D}^2 + \mathbf{V}\mathcal{D} + \mathbf{X} \right) \tag{4.123}$$

$$k^2\mathbf{A_2}\hat{\mathbf{u}} + k\mathbf{A_1}\hat{\mathbf{u}} + \mathbf{A_0}\hat{\mathbf{u}} = 0 \tag{4.124}$$

This is a polynomial eigenvalue problem for the parameter k, as was presented in the last section to the Less-Lin equation. To solve it, is necessary linearized in the same way as was made previously a variable change is proposed

$$\hat{\mathbf{m}} = k\hat{\mathbf{u}} \tag{4.125}$$

and the above equation become:

$$kA_2\hat{m} = -A_1\hat{m} - A_0\hat{u} \tag{4.126}$$

Them, the polynomial eigenvalue problem can be written as a linear generalized eigenvalue problem in matrix form $\mathbf{Ax} = \lambda\mathbf{Bx}$

$$\begin{bmatrix} 0 & \mathbf{I_d} \\ -\mathbf{A_0} & -\mathbf{A_1} \end{bmatrix} \begin{bmatrix} \hat{u} \\ \hat{m} \end{bmatrix} = k \begin{bmatrix} \mathbf{I_d} & 0 \\ 0 & \mathbf{A_2} \end{bmatrix} \begin{bmatrix} \hat{u} \\ \hat{m} \end{bmatrix} \tag{4.127}$$

where $\mathbf{I_d}$ is the identity matrix.

The boundary conditions for the perturbation variables are imposed.

For $r \to 0$ the perturbation must be bounded Gloor et al. (2013):

$$\frac{d\rho'}{dr} = \frac{dw'}{dr} = \frac{dp'}{dr} = u' = 0, \tag{4.128}$$

and for $r \to \infty$ all perturbation goes to zero

$$\rho' = w' = p' = u' = 0. \tag{4.129}$$

4.5.2 Generalized eigenvalue problem

The solution of the stability equations both the Less-Lin equation (Compressible Rayleigh equation) 4.92 and the linear Navier-Stokes 4.127 equation are able to be resolved transforming the problem in a generalized eigenvalue problem of the kind

$$\mathbf{Ax} = \mathbf{B}\lambda\mathbf{x}, \tag{4.130}$$

where $\mathbf{A}$ and $\mathbf{B}$ are matrices, $\mathbf{x}$ is the generalized eigenvector and λ is an generalized eigenvalue of $\mathbf{A}$ and $\mathbf{B}$. If $\mathbf{B}$ is a non-singular matrix this problem turns to a classical eigenvalue problem.

$$\mathbf{Cx} = \lambda\mathbf{x} \tag{4.131}$$

with $\mathbf{C} = \mathbf{B}^{-1}\mathbf{A}$.

To resolve the generalized eigenvalue problem the Spectral Collocation method was used. To it the operator that discretize a linear system of ordinary differential equation of the form

$$\mathcal{L}(\hat{r})\hat{p} = \left(a_n(\hat{r})\mathcal{D}^{(n)} + a_{n-1}(\hat{r})\mathcal{D}^{(n-1)} + ... + a_1(\hat{r})\mathcal{D} + a_0(\hat{r}) \right) \hat{p} \tag{4.132}$$

where the operator $\mathcal{D}^{(n)}, \mathcal{D}^{(n-1)}, ..., \mathcal{D}$ represent the derivatives $d^{(n)}/d\hat{r}^{(n)}, d^{(n-1)}/d\hat{r}^{(n-1)}, ..., d/d\hat{r}$, respectively and the coefficients a_n defining completely this differential operator.

The solution to the system of ordinary differential equation 4.132 can be represented by the function $\hat{p}$,

$$\hat{p}(\hat{r}) \approx \sum_{j=0}^{N} a_n \phi(\hat{r}), \tag{4.133}$$

where $\phi(\hat{r})$ are the known as trial function.

For the function 4.133 be solution of the differential equation 4.132 the residual $\mathcal{R}(\hat{r})$ must be vanish, so that

$$\mathcal{R}(\hat{r}) = \mathcal{L}_{ij}(\hat{p}(\hat{r})) = \mathcal{L}_{ij} \left(\sum_{j=0}^{N} a_n \phi(\hat{r}) \right) = 0 \tag{4.134}$$

In order to find the coefficients a_n, that determine the solution the weighted residual method can be used, which required that internal product over the domain d,

$$\int_d w(\hat{r})\mathcal{R}(\hat{r})d\hat{r} = 0, \tag{4.135}$$

which means that the residual $\mathcal{R}$ required to be orthogonal to all test functions (weights) w. This is the reason why the method is called method of weighted residuals Mason and Handscomb (2002). The test function w to the spectral collocation method is defined by

$$w(\hat{r}) = \delta(\hat{r} - r_i), \tag{4.136}$$

where the Dirac delta function δ is defined as

$$\delta(\hat{r} - r_i) = \begin{cases} \infty & \text{if} \quad r = r_i \\ 0 & \text{if} \quad r \neq r_i \end{cases}. \tag{4.137}$$

Using the properties of the delta function

$$\int_d \delta(\hat{r} - r_i)\mathcal{R}(\hat{r}) = \mathcal{R}(r_i) = 0, \tag{4.138}$$

being r_i points, the collocation points, where the differential equation is satisfied exactly, $\mathcal{L}(\hat{p})|_{\hat{r}=r_i} = 0$.

In the case of the collocation spectral method the collocation points are the extreme of the Nth order Chebyshev polynomial, given by

$$r_i = \frac{cos\pi j}{N} \qquad j = 0, 1, ..., N \tag{4.139}$$

and known as the Gauss-Lobatto points. defined on the interval $-1 \leq r_i \leq 1$.

Now, in the collocation spectral method or pseudo-spectral method the test function for a non-periodic problem are the Chebyshev polynomials. The Chebyshev polynomials of Nth order are defined as

$$\phi_n(\hat{r}) = cos(jcos^{-1}(\hat{r})), \quad j = 0, 1, ..., n. \tag{4.140}$$

with $\phi_0(\hat{r}) = 1$, $\phi_1(\hat{r}) = \hat{r}$, $\phi_2(\hat{r}) = 2\hat{r}^2 - 1$,..., $\phi_{n+1} + \phi_{n_1} = 2\hat{r}\phi_n(\hat{r})$,

Is interesting to note that if the test function is selected as polynomials of lower order, the equation represent a differential finite scheme.

Therefore, to find the coefficient to the interpolating polynomial at the Gauss-Lobatto points is necessary to solve a system of $N+1$ equation with $N+1$ unknowns:

$$\mathcal{L}(p(r_i)) = \mathcal{L}\left(\sum_{j=0}^{N} a_n \phi(r_i)\right) = 0. \tag{4.141}$$

If a collocation method is employed, the derivative of a discretized function $\hat{p}(r_i)$ can be written as a matrix multiplication. To that, the derivatives of a polynomial function can be expanded over a polynomial base function as

$$\frac{d^{(m)}}{d\hat{r}^{(m)}}\hat{p}(\hat{r}) = \sum_{j=0}^{N} a_i' \phi(\hat{r}). \tag{4.142}$$

In this case the $\phi(\hat{r})$ represent the Chebyshev polynomials. As $d^{(m)}\hat{p}(\hat{r})/d\hat{r}^{(m)}$ is polynomial it can expressed by unique Lagrange polynomial, the lowest degree polynomial using the values $\hat{r}_i$, in this case the collocation points, so that

$$\frac{d^{(m)}}{d\hat{r}^{(m)}}\hat{p}(\hat{r}) = \sum_{i=0}^{N} \frac{d^{(m)}}{d\hat{r}^{(m)}}\hat{p}(r_i) l_i(\hat{r}), \tag{4.143}$$

where l_i are the Lagrange polynomials defined by

$$l_i(\hat{r}) = \frac{\gamma_n(\hat{r})}{\gamma_n'(\hat{r} - r_i)} \tag{4.144}$$

with

$$\gamma_n(\hat{r}) = \prod_{i=0}^{n}(\hat{r} - r_i) \tag{4.145}$$

Then, the coefficients to interpolate the derivative of the polynomial function $d^{(m)}\hat{p}(r)/(d\hat{r}^{(m)})$ are determined by

$$a_n' = \frac{d^{(m)}}{d\hat{r}^{(m)}}(l_i(\hat{r}_i)) \tag{4.146}$$

$$\frac{d^{(m)}}{d\hat{r}^{(m)}}\hat{p}(\hat{r}) = \sum_{j=0}^{N} a_i' \phi(\hat{r}_i) = \sum_{j=0}^{N} D_{ij}^{(m)}\hat{p}(r_i) \tag{4.147}$$

The matrix $D_{ij}^{(m)}$ is known as the (Chebyshev) derivative matrix, and represents a transformation into spectral space of spatial derivative.

Using the Chebychev polynomial ϕ to expressed the the Lagrange polynomials as

$$\gamma_n = (\hat{r}^2 - 1)\frac{d\phi_n}{d\hat{r}} = (\hat{r}^2 - 1)\phi_n' \tag{4.148}$$

So, is possible to shown that the derivative matrix

$$\frac{d}{d\hat{r}}(l_i(\hat{r}_i)) = D_{ij}, \tag{4.149}$$

using the Lagrange polynomials in the Gauss-Lobatto points, the derivative matrix can be calculate as

$$D_{ij} \begin{cases} \dfrac{c_i}{c_j}\dfrac{(-1)^{i+j}}{\hat{r}_i - \hat{r}_j} & i \neq j \\[2mm] -\dfrac{\hat{r}_i}{2(1-\hat{r}_i^2)} & 1 \leq i = j \leq N-1 \\[2mm] \dfrac{2N^2+1}{6} & i = j = 0 \\[2mm] -\dfrac{2N^2+1}{6} & i = j = N \end{cases} \tag{4.150}$$

with $c_i = 1$, except for $c_0 = c_N = 2$, and N is the number of collocation points, (TREFETHEN, 2000).

Then, a ordinary differential equations, that has the form of the linear system that represent the eigenvalue problem for k as 4.116 and 4.127 can be discretized as

$$\mathcal{L}_{ij}(\hat{r})\hat{p}(\hat{r}) = \left(a_n(r_i)\mathcal{D}_{ij}^{(m)} + a_{n-1}(r_i)\mathcal{D}_{ij}^{(m-1)} + ... + a_1(r_i)\mathcal{D}_{ij} + a_0(r_i)\right)\hat{p}(r_i) \tag{4.151}$$

over the collocation point r_i.

The generalized eigenvalue problem 4.130 is solved using $N = 300$ Chebyshev collocation points. As the collocations points are in the interval [-1,1], the mapping presented in (4.152) is used.

$$y = \beta \tan\left(\frac{\pi}{2N}\right), \tag{4.152}$$

where β controls the grid stretching and $\beta = 0.2$ was used.

5 LINEAR STABILITY ANALYSIS

In this Chapter the results of the linear stability analysis for inviscid problem will be presented and discussed. In order to show the effect of binary species in the formation of coaxial jet and their stability characteristics, some of the results presented by Perrault-Joncas and Maslowe (2008) were reproduced. It was also useful to verify the spectral code implemented.

To show that there are different effects in the stability properties beyond compressibility, caused by the use of different species with its respective speed of sound, a low Mach number and incompressible formulation will be presented.

5.1 Description of the mean flow profiles

As was used by Perrault-Joncas and Maslowe (2008) the mean flow used in the linear stability analysis is determined by a canonical profiles.

The velocity profile is defined by

$$\bar{w} = (1 - h)w_1 + hw_2, \tag{5.1}$$

where

$$w_n = \frac{1}{2}\left\{1 + tanh\left[b_n\left(\frac{R_n}{r} - \frac{r}{R_n}\right)\right]\right\} M \quad n = 1, 2. \tag{5.2}$$

The parameter h is the velocity ratio between the primary stream, defined by the value of the velocity at radii R_1, and the velocity of the secondary stream, defined by the velocity value in the radii R_2 of the coaxial jet. M represents the Mach number of the inner jet in relation to oxygen speed of sound at the temperature of the center of the coaxial jet, $r = 0$. In the cases evaluated $M = 0.6558$ was selected because as shown by Joncas and Maslowe, above the $M > 0.8281$ radiating modes exist which have different behavior of the well known instability modes, the Kelvin-Helmholtz mode. The other parameters, b_1 and b_2 are related to the momentum thickness of the shear layer of the different streams θ_1 and θ_2 and are defined by the relation $b_n = R_n/4\theta_n$, where θ_n is the momentum thickness.

Beginning the evaluation of the geometric effects in the change of the radius of the coaxial jet, the ratio between them $\Gamma = R_2/R_1$ was defined. To account for the

change of momentum thickness of the outer stream when R_2 and b_2 is modified the relation 5.3 was employed

$$\theta_2 = \frac{3}{100}\left(z + \frac{4}{3}R_2\right).$$

(5.3)

This relation is valid to slowly diverging jet flows and used in axisymmetric jet by Crighton and Gaster (1976). and in coaxial jet by Perrault-Joncas and Maslowe (2008).

Crow and Champagne (1971) shown that the first instabilities develop at one diameter downstream of the exhaust of the jet. Then, $R = 2R_1$ will be use as axial coordinate and $\theta_1 = 0.1$ with $\theta_2 = 3/50 + R_2/25$, being a function of R_2.

The temperature of the base flow was also defined using a canonical profiles. Papamoschou (2004) proposed the use of

$$\bar{T}_{hot} = \frac{1}{2}\left(1 - S\right)\left\{1 + tanh\left[b_n\left(\frac{R_n}{r} - \frac{r}{R_n}\right)\right]\right\} + S,$$

(5.4)

to represent a coaxial jet with inner jet S times hotter than the outer jet. This profile was referenced as "Hot" by Joncas and Maslowe and was used at Mach number of $M = 0.6558$, with respect to to average velocity of the inner jet. They also defined a "Cold" profile to fit the Paparamoschou's experiments using a second order polynomial

$$\bar{T}_{cold} = a_0\bar{w}^2 + b_0\bar{w} + c_0,$$

(5.5)

where $a_0 = -0.0592$, $b_0 = -0.1032$ and $c_0 = 1.1624$. The Mach number in relation to the average velocity of inner jet used was $M = 1$.

Figure 5.1 - Comparison between spectral code and the results for compressible and incompressible coaxial jet of Perrault-Joncas and Maslowe (2008), with $\Gamma = 2$, $h = 0.7$ and the different canonical profiles of temperature.
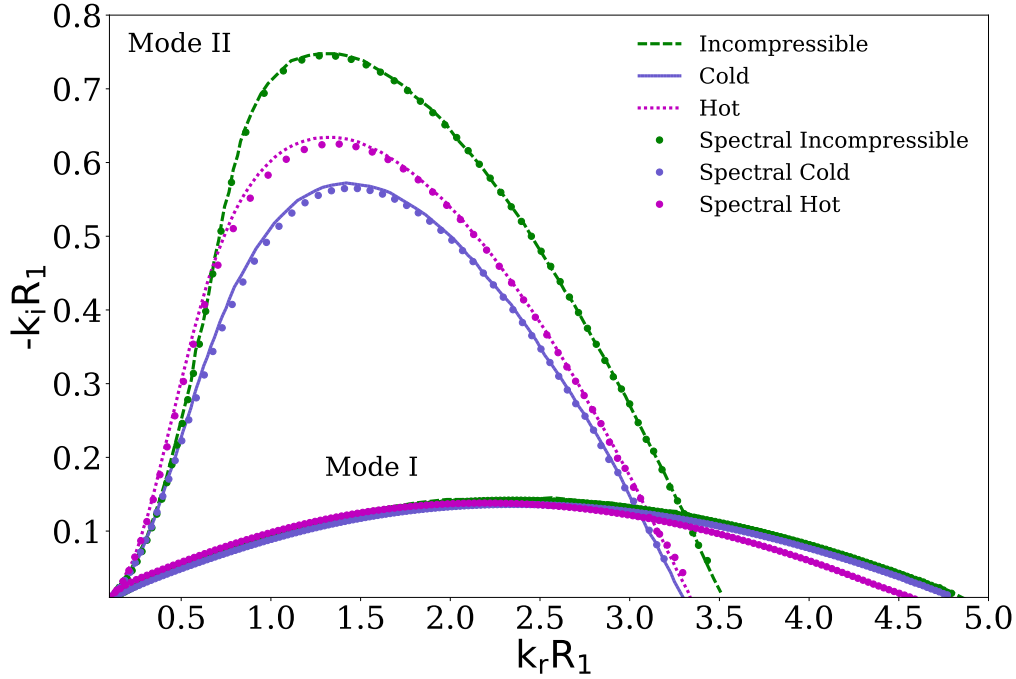
To verified the present spectral collocation method the results of Perrault-Joncas and Maslowe (2008) for incompressible and compressibles profiles with different temperature for coaxial jet were reproduced and are presented in Figure 5.1. This figure shows a good agreement between the results and is also useful to remember, as was presented in the introduction, that a coaxial jet present two hydrodynamic modes related with the shear layer that form it. The first mode (Mode I) is related to the shear layer formed with the inner and the outer jets. The second mode is related to the shear layer formed with the outer jet and the ambient (Mode II). Theses modes defined the hydrodynamic characteristics of homogeneous coaxial jets.

Once the spectral code was verified to find the two modes of instability of coaxial jets, the first cases evaluated were chosen as incompressibles cases. This with the intention to investigate if there is another reason different that compressibility that affect the stability characteristic of the coaxial jet when different chemical species, like oxygen and hydrogen form it.

There are two ways to neglect the compressible effect in the problem, a low Mach

number formulation or an incompressible formulation.

5.2 Low Mach number formulation

One way to avoid the compressible effects over the growth rates using low Mach number formulation is increasing the pressure of the base as follows.

Remembering that the non-dimensional linear inviscid perturbation Navier-Stokes equation for a parallel flow that depict a compressible coaxial jet are given by

$$\bar{\rho}\frac{\bar{D}\mathbf{u}'}{\bar{D}t} + \bar{\rho}\frac{D'\bar{\mathbf{u}}}{D't} = -\nabla p', \tag{5.6}$$

$$\frac{\bar{D}p'}{D't} + \gamma_0\gamma\bar{p}\left(\nabla\cdot\mathbf{u}'\right) = 0. \tag{5.7}$$

The linear conservation of mass and the perfect gas equations are not presented here because their were used to obtain the pressure perturbation equation.

It is interesting to note that the parameter that controls the compressibility in the above system of equations in this non-dimensional form is the pressure of the base flow $\bar{p}$.

When the dynamic pressure $p_d = \rho_0 u_0^2$ is not used to scale the pressure of the system and the static pressure $p_s = \rho_0 R_0 T_0$ is used, the conservation of momentum results

$$\bar{\rho}\frac{\bar{D}\mathbf{u}'}{\bar{D}t} + \bar{\rho}\frac{D'\bar{\mathbf{u}}}{D't} = -\frac{1}{M_0^2\gamma}\nabla p'. \tag{5.8}$$

In order to work in a low Mach regime, the pressure perturbation must be of the order of $M_0^2\gamma$ which means

$$p = \frac{\tilde{p}}{p_0} = \frac{\tilde{\bar{p}}}{p_0} + \frac{1}{M_0^2\gamma}\frac{\tilde{p}'}{p_0} \tag{5.9}$$

The tilde variables $\tilde{\bar{p}}$ and $\tilde{p}'$ represent the base flow and the perturbation pressure respectively, in dimensional form.

Now, making the reference pressure $p_0 = p_d = \rho_0 u_0^2$ with u_0 is a generic reference velocity, then

$$p = \frac{\tilde{p}}{p_0} = \bar{p} + p', \tag{5.10}$$

where is clear that $\bar{p} \gg 1/M_0^2\gamma$, to hold the low Mach number approximation and to allow define the perturbation pressure in the problem.

Therefore make $\bar{p} \gg 1/M_0^2$ define a low Mach number regime and the leading terms of the system of equations that describe a compressible low Mach number coaxial jet and are given by

$$\nabla \cdot \mathbf{u}' = 0, \tag{5.11}$$

$$\bar{\rho}\frac{\bar{D}\mathbf{u}'}{\bar{D}t} + \bar{\rho}\frac{D'\bar{\mathbf{u}}}{D't} = -\nabla p', \tag{5.12}$$

In order to obtain the density perturbation the mass conservation equation is used, so that

$$\frac{\bar{D}\rho'}{\bar{D}t} + \frac{D'\bar{\rho}}{D't} = 0. \tag{5.13}$$

If specific mass perturbation, Y_i' is considered, it is necessary to consider the perturbation conservation of R'

$$\frac{\bar{D}R'}{\bar{D}t} + \frac{D'\bar{R}}{D't} = 0, \tag{5.14}$$

presented in the Chapter 4.

The temperature disturbances are obtained with the perturbation ideal gas equation.

$$p' = \rho'\bar{R}\bar{T} + \bar{\rho}R'\bar{T} + \bar{\rho}\bar{R}T' \tag{5.15}$$

In order to get an ordinary differential equation for the pressure disturbances, the above system of equations can be collected using the ansatz of the linear stability analysis, $\mathbf{q}'(r, z, t) = \hat{\mathbf{q}}(r)e^{i(kz - \omega t)}$, with it the eigenvalues of the problem k and ω can be obtained.

If a similar procedure used to obtain the pressure perturbation equation for a compressible flow is adopted, the low Mach number equation is obtained, then

$$\frac{d\hat{p}}{dr^2} + \left(\frac{1}{r} - \frac{1}{\bar{\rho}}\frac{d\bar{\rho}}{dr} - \frac{2k}{(k\bar{w} - \omega)}\left(\frac{d\bar{w}}{dr}\right)\right)\frac{d\hat{p}}{dr} - k^2\hat{p} = 0. \tag{5.16}$$

It is interesting to note that the only way that the species or the temperatures changes affect the stability characteristics in low Mach number regime is by the density profile, more specifically the gradient of the density in the radial direction. This term, $d\bar{\rho}/dr$, comes from the linear conservation of mass equation, u'$d\bar{\rho}/dr$, and can be interpreted as the change of inertia of the flow due mass changes, the change of mass flux of perturbation in radial direction caused by the density changes of the base flow.

There are another important effects caused by the density profile. If the low Mach number pressure disturbance equation is compared with the pressure compressible equation derived in the formulation chapters, and repeating here

$$\frac{d^2\hat{p}}{dr^2} + \left(\frac{1}{r} - \frac{1}{\bar{\rho}}\frac{d\bar{\rho}}{dr} - \frac{2k}{(k\bar{w} - \omega)}\left(\frac{d\bar{w}}{dr}\right)\right)\frac{d\hat{p}}{dr} + \left(\left((k\bar{w} - \omega)^2\frac{\bar{\rho}}{\gamma_0\gamma\bar{p}} - k^2\right)\right)\hat{p} = 0. \tag{5.17}$$

The density appears again in the last term of this equation, meaning that if it has a different density profile being caused by the use of different species that form the coaxial jet, or for having different temperatures in the jets stream, the speed of sound of the medium change, which is the velocity at which the perturbation can be travel.

Then the density plays two important role, change the inertia of the flow and modified the speed of sound. There are two ways to change the density, change the temperatures of the gases or change the gases that form the coaxial jet. Physically it allows to have larger gradient of density that modify the stability characteristic.

In order to shown how the pressure of the base flow controls the compressibility, different base pressure values were evaluated and are presented in the Figures 5.2 and 5.3. As was expected, the compressibility reduce the amplification rates, being achieved with low values of $\bar{p}$, although as was view $\bar{p}$ must be greater that $1/\gamma M_0^2 = 1/(1.4*0.6558^2) \approx 1.660$ to allows the definition of the pressure perturbation in a low Mach number approximation.

Large values of $\bar{p}$ lead to low Mach number formulation. As will be discussed in the next section an incompressible case and low Mach number formulation, both agree on their answers when the density profiles induced by the species or by different temperatures or by both, are not pronounced.

Figure 5.2 - Growth rates using different base pressure $\bar{p}$, showing that its increase leads to the incompressible case. The parameter of the base flow velocity for a coaxial jet are $\Gamma = 2$ and $h = 0.7$, with isothermal and same species jets.
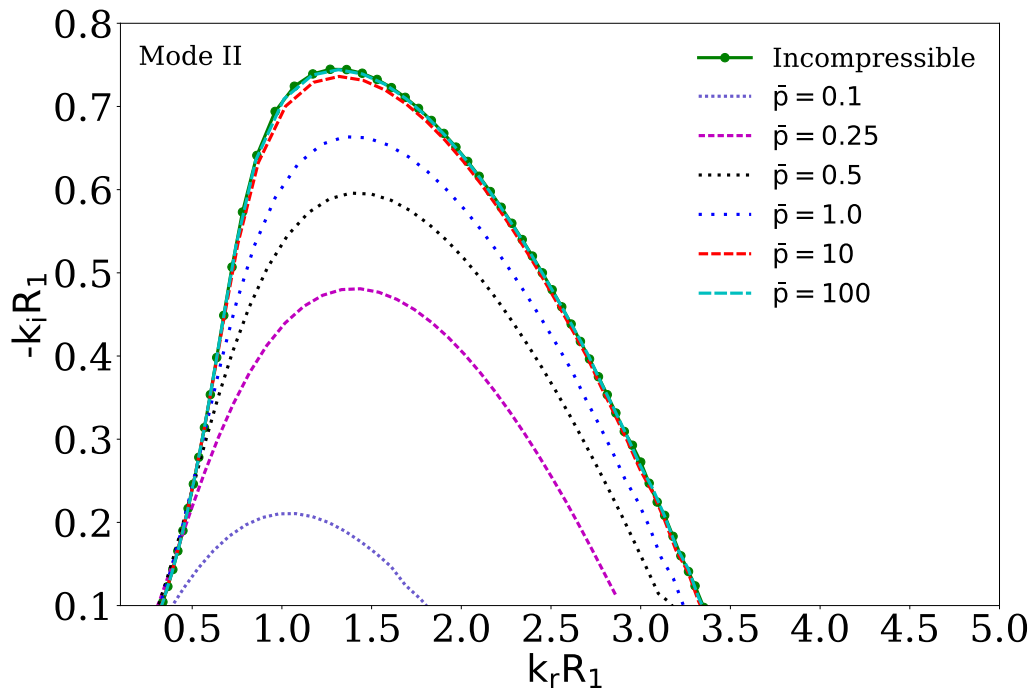
The changes of the phase velocity of the instability waves are presented in Figure 5.3, showing that if the compressibility is neglected the K-H waves are able to travel a high velocities in low frequencies, decreasing its velocity with the $\bar{p}$.

In Figure 5.3 the incompressible case are not presented because Perrault-Joncas and

Maslowe (2008) only show the real and the imaginary part of the wave number as well as the growth rates of the mode I.

Figure 5.3 - Stability characteristics changing the base flow pressure $\bar{p}$.

(a) Growth rates   (b) Phase velocity
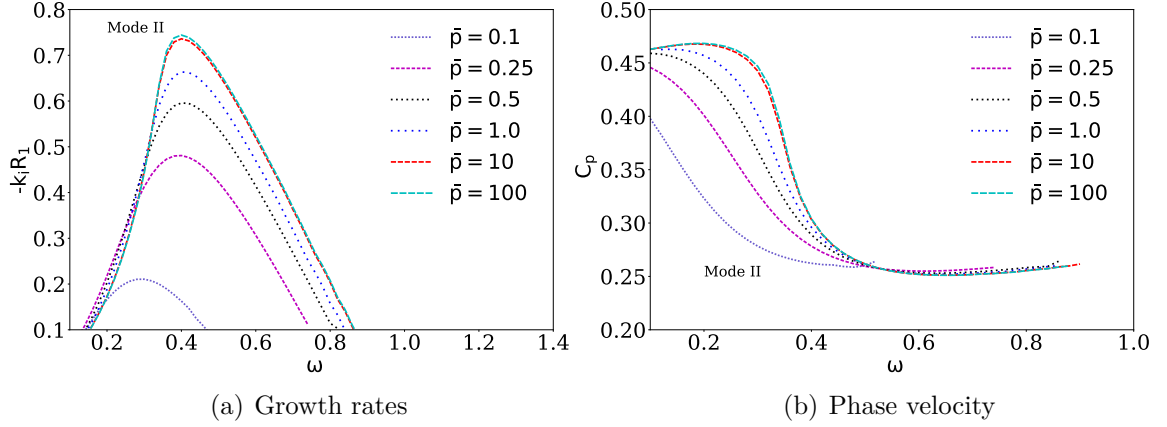
5.3   Incompressible formulation

In order to obtain an incompressible formulation, the mathematical way to do this is considering constant the density perturbation , i.e. using the linear perturbation conservation mass equation as

$$\frac{D'\bar{\rho}}{D't} + \bar{\rho}\nabla \cdot \mathbf{u}' = 0, \tag{5.18}$$

together with the momentum conservation equation

$$\bar{\rho}\frac{\bar{D}\mathbf{u}'}{\bar{D}t} + \bar{\rho}\frac{D'\bar{\mathbf{u}}}{D't} = -\nabla p'. \tag{5.19}$$

This system of equation can be transformed in an ordinary differential equation using the Rayleigh procedure for incompressible flows and as was done in the previous section, the incompressible pressure perturbation equation is obtained

$$\frac{d^2\hat{p}}{dr^2} + \left(\frac{1}{r} - \frac{2k}{(k\bar{w} - \omega)} \frac{d\bar{w}}{dr} \right) \frac{d\hat{p}}{dr} - k^2\hat{p} = 0. \tag{5.20}$$

It interesting to note that, this is the Rayleigh equation for incompressible flow, although a non-uniform base flow profile of density was used to obtain it. This means that if a incompressible formulation is used to make a stability analysis, the eigenvalues k and ω will be the same as that of a flow without density gradients.

The only part when the density plays a role, in this incompressible formulation, is in the calculation of the eigenfunction, as in the radial perturbation velocity,

$$u' = -\frac{1}{i\bar{\rho}\left(k\bar{w} - \omega\right)} \frac{\partial p'}{\partial r}. \tag{5.21}$$

Therefore an incompressible formulation when there are larger gradient of the base flow density in not appropriated, although mathematically it exits. A low Mach number formulation in consequence must be used, which makes sense because it corresponds to making a physical parameter, the Mach number, sufficiently small, opposite to the mathematical reason to make the perturbation flow incompressible.

Is important to note that, the incompressible and low Mach number formulation coincide when the gradients of density are small or does not exits.

5.4 Linear stability analysis results

5.4.1 Homogeneous coaxial jet

Once the spectral code was verified to find the two modes of instability of coaxial jet, the first cases evaluate were chosen as isothermal and with the same species (homogeneous flow), without density variation in the base flow, where the geometric parameter radii ratio Γ and the velocities ratio h were modified to assess the stability characteristics of a coaxial binary jet. The homogeneous flow cases are relevant to evaluated the characteristics of stability since the compressibility only has a stabilizing effect, as was shown in the previous section. This effect can be visualized in Figure 5.1 and it was one of the results shown by Perrault-Joncas and Maslowe (2008).

Several Γ ratios were evaluated and the axial velocity base flow is presented in Figure 5.4. As shown in this figure a small Γ ratio transform the coaxial jet in a single jet,

it is corroborate by the instability growth rate showing only one mode, Figure 5.5, corresponding to shear layer formed by the ambient and the inner jet, Figure 5.4. The behavior of this only mode is more similar to the second instability mode than the first mode of the coaxial jet, it due to the larger gradients of velocity.

Figure 5.4 - Base flow axial velocity $\bar{w}(r)$ for different Γ ratio with the the same velocity ratio $h = 0.7$.
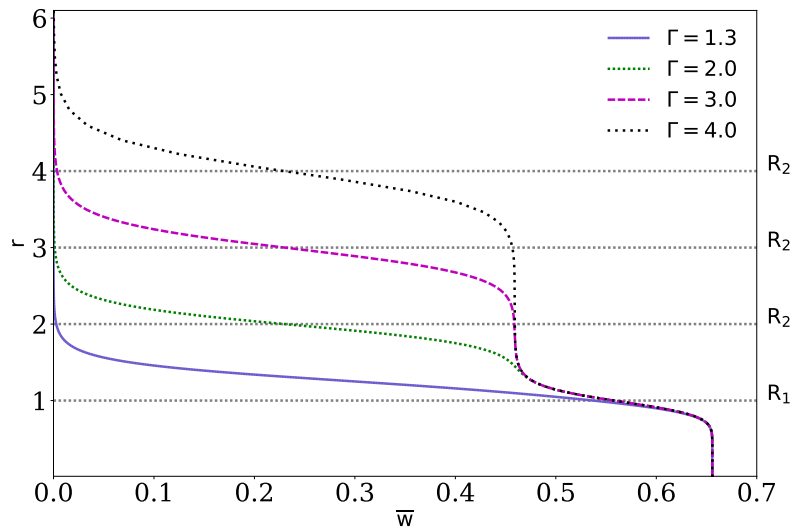
Larger radii ratios Γ have smooth transition between the jet velocities, Figure 5.4, causing not pronounced growth rates and a slow phase velocity, Figure 5.6.

There are one relation corresponding to $\Gamma = 2$ with the largest growth rate in Mode II. For this reason this will be the Γ ratio used in other cases evaluated. Changing the radii ratio Γ, the Mode II is favored and the Mode I is not affected.

Figure 5.5 - Effect of Γ ratios on instability growth rates $-k_i$, as a function of real part of
the wave number k_r, at velocity ratio $h = 0.7$.
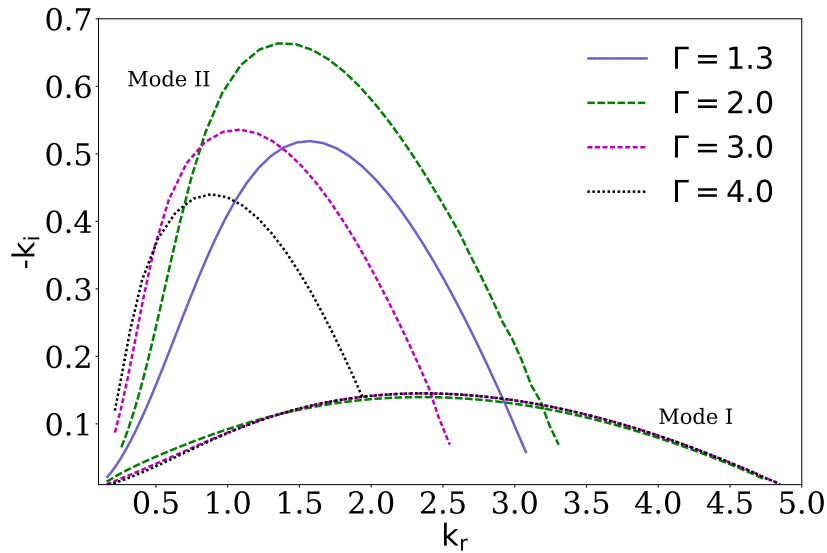
Figure 5.6 - Effect of Γ ratio on instability characteristics for different geometric config-
uration with velocity ratio of $h = 0.7$, as a function of the waves frequency
ω.

(a) Growth rates k_i.

(b) Phase velocity $C_p = \omega/k_r$.
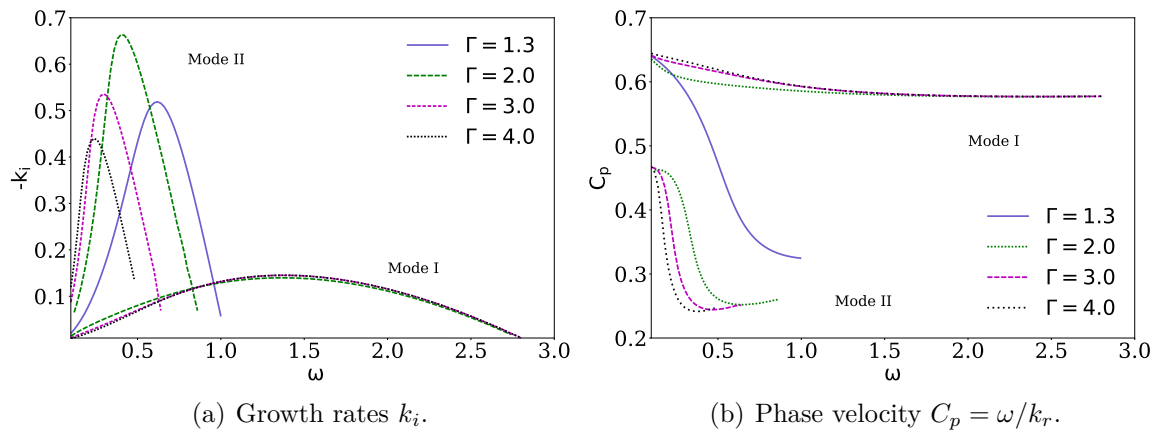
In relation to the phase velocity, Figure 5.6b the first instability modes, Modes
I, are little dispersive, almost constant phase velocity, with respect to the second
instability modes, Mode II, where the phase velocity is a function of the frequency
but is interesting to note that dispersion relation is almost linear.

Following with the homogeneous coaxial jet, different velocity ratios h, were considered and the modification in the axial velocity of the base flow can be see in Figure 5.7.

Figure 5.7 - Base flow radial velocity $\bar{w}(r)$ for different h ratio with $\Gamma = 2$.
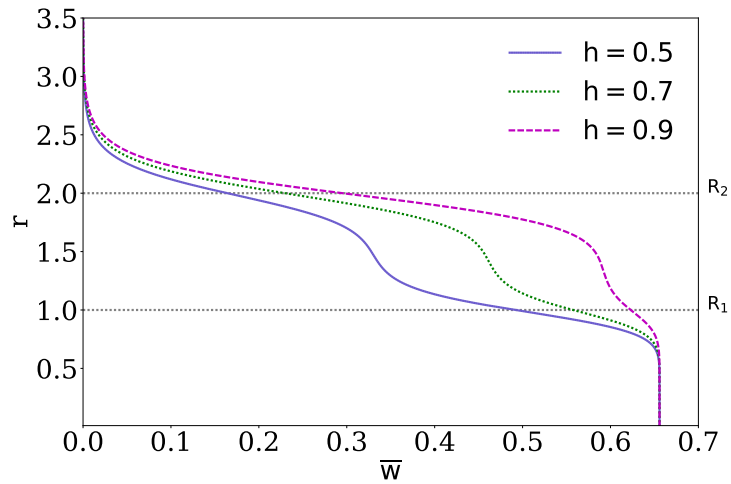
The changes in the h ratio modify visibly the Mode I, it is clear the thickness modification of the inner shear layer, Figure 5.7. As expected the smallest thickness originated the highest growth rates and the largest thickness produce the minimum amplification rate, as is presented in Figure 5.8.

Figure 5.8 - Effect of velocity ratio h on instability growth rate k_i, as a function of the waves frequency at velocity ratio of $\Gamma = 0.7$.
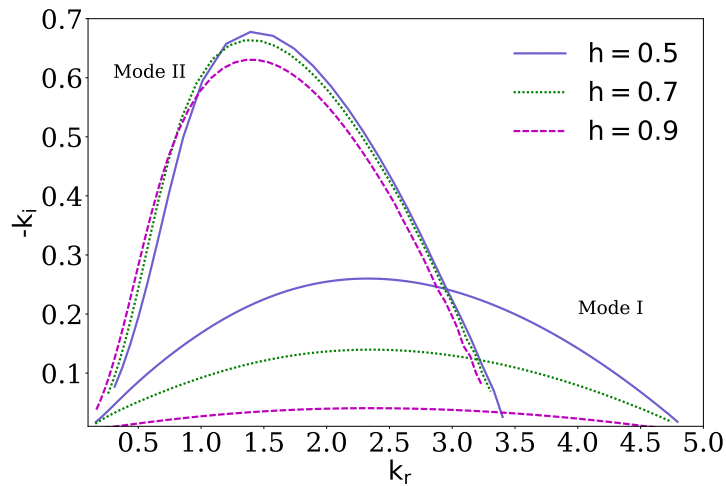
Although the growth rates are not modified by the change in h for the Mode II, the phase velocity of this waves is changed, resulting in the highest values with the largest value of the velocity ratio parameter, Figure 5.9b.

To clarified this, a classical spatial stability graph with α_i as a function of the ω is presented in Figure 5.9a. It is evident the change in the frequency of the maximum amplification rate, modifying correspondingly its phase velocity. Besides this, the first instability mode, Modes I, are little dispersive, almost constant phase velocity, with respect to the second instability mode, Mode II, where the phase velocity is a function of the frequency.

Figure 5.9 - Effect of velocity ratio h on instability characteristics at velocity ratio of $\Gamma = 0.7$, as a function of the waves frequency.

(a) Growth rates k_i.

(b) Phase velocity $C_p = \omega/k_r$.
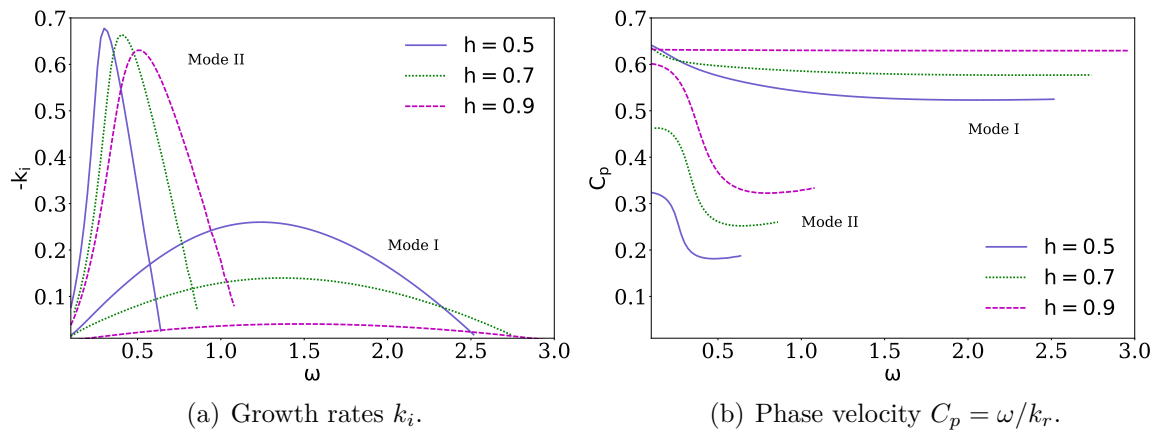
As was reported by Perrault-Joncas and Maslowe (2008) this two parameters both the geometric Γ ratio as the velocity ratio, control the two instability modes of the coaxial jet.

5.4.2 Binary coaxial jet

The purpose of this study is to identify the role of the composition of the coaxial jet in its stability characteristics, using chemical species like oxygen and hydrogen to form it.

Attending to the requirement of isothermal coaxial jets, it is without changes of density caused by the temperature, different species compositions were evaluated

and its density base flows are presented in Figure 5.10. In these base flow $h = 0.7$ and $\Gamma = 2.0$ was used in its definition.

The reference properties, as can be see in the Figure 5.10, were chosen with respect to the same chemical species, the oxygen. This fact corresponds to keep the Mach number in reference to the oxygen, as it is more similar to air than in relation to the hydrogen, where the speed of sound is about 4 times greater.

Figure 5.10 - Density base flow profiles for different binary coaxial jet, non-dimensional respect the oxygen jet at the $r = 0$ temperature, $\Gamma = 2$ and $h = 0.7$.
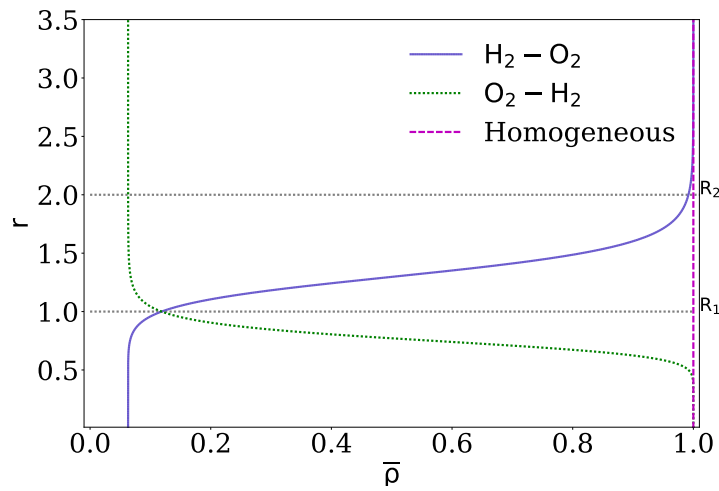
The first species that appears in the nomenclature in the label of the figures indicate the species used in the inner jet and the second represent the species used in the outer jet and the ambient. There is a case without gradients of density, homogeneous case, formed with the same species in both the inner and outer jet, being oxygen or hydrogen and with $\bar{\rho} = 1$.

The change in the density due to the formation of the coaxial jet with different species is evident in the density base flow distribution, Figure 5.10. To construct this density profile the specific mass base flow were created using the same form of the canonical profiles used for the axial velocity.

The mass fraction profiles are defined by

$$\bar{Y}_1 = \frac{1}{2} \left\{ 1 + tanh \left[b_1 \left(\frac{R_1}{r} - \frac{r}{R_1} \right) \right] \right\} \qquad (5.22)$$

and

$$\bar{Y}_2 = 1 - \bar{Y}_1. \tag{5.23}$$

The b_1 parameter related with the momentum thicknesses is the same as that used in the velocity profile, also the h relation. This base flow profile is presented in the Figure 5.11.

Figure 5.11 - Mass fraction $\bar{Y}_1$ and $\bar{Y}_2$ base flow profiles used to obtain the density base flow $\bar{\rho}$, representing binary coaxial jet with $\Gamma = 2$ and $h = 0.7$.
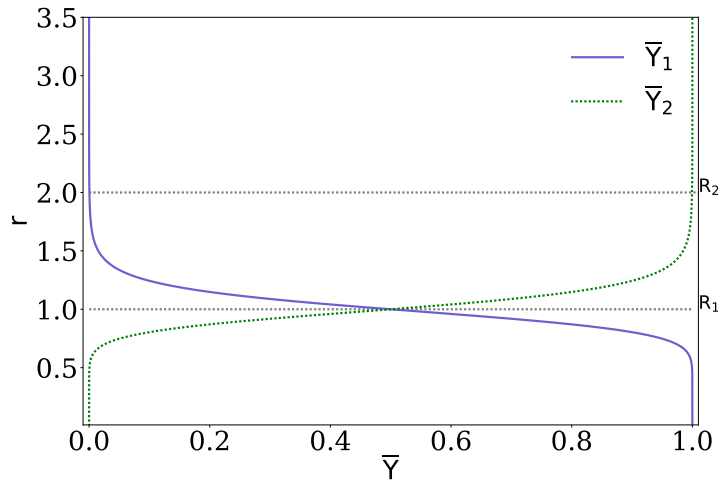
As was presented in section 5.2, the low Mach number formulation allows to neglect the effects of compressibility given by the use of different species that changes the speed of sound and given at the Mach number of the inner jet $M = 0.6558$, which are considerable, and allows to only concentrate in the the effects of the gradient of velocity and density. In this case the density gradients are caused by the used of different species.

Figure 5.12 presents the growth rates for compressible and low Mach number coaxial jet using different species and using a homogeneous configuration, without density or temperature gradients in the base flow.

The low Mach number configuration can be distinguished by the use of a line thickness but the same color and line type than the compressible cases.

Figure 5.12 - Effect of species configuration and compressibility (thinner lines) on insta-
bility growth rates k_i, for a coaxial binary jet as a function of the real wave
number k_r. With $\Gamma = 2$ and $h = 0.7$.
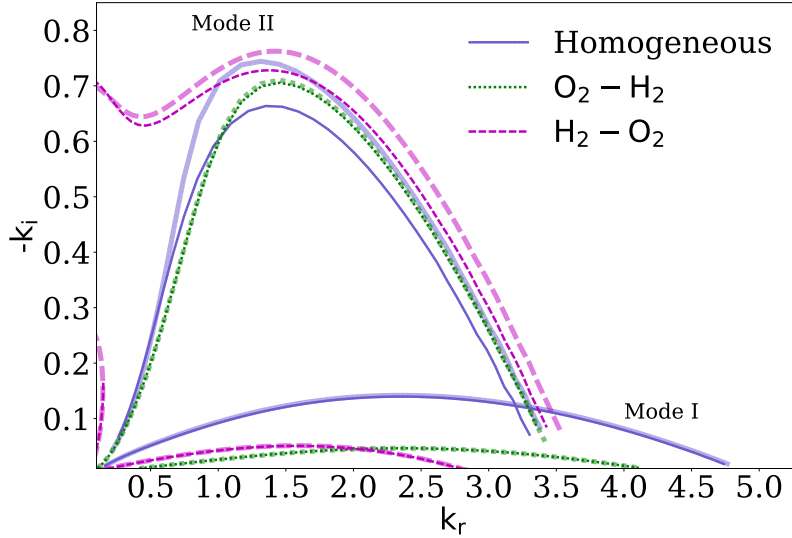
Differently than what happened with the change in the parameters Γ and h, which
modified a single mode of the coaxial jet, the change in the density profile induced
by the use of different species in the formation of the jets, changes both modes, this
can be distinguished even in the low Mach number as well the compressible cases.

As can be seen in Figure 5.12, the growth rates of the second mode are higher when
the oxygen is positioned in the outer jet, and smaller when it is positioned in the
inner jet. However, in both cases, the growth rates are larger than the homogeneous
case even in the compressible and the low Mach number cases. Furthermore, when
the low Mach number approximation is used to compare the results, the maximum
amplification rate is also given by the $H_2 - O_2$ configuration, which is consistent
with Kozusko et al. (1996b) results, when the heavier species is in the lower velocity
stream the amplification rates are larger. This meaning that the use of the species
like hydrogen, where the speed of sound is almost 4 times the oxygen speed of sound,
allows that compressible effects, that always reduce the amplification rates, do not
be so pronounced. This is most evident in the $O_2 - H_2$ configuration, where the
compressibility does not change visually the growth rates. In this case, the medium
when the coaxial jet is ejected is formed by hydrogen too, making the speed of
sound larger that the medium with oxygen, which implies that it can be considered
as the low Mach number case. Remember that the speed of sound of reference is

with respect to the oxygen stream and the Mach number of the inner jets at $r = 0$ is $M = 0.6558$, if this Mach number was measured with respect to the hydrogen the values will be $M \approx 0.16$, where the compressible effects are really negligible.

Differently then, as was made by Kozusko et al. (1996b), who use the convective Mach number to compare the amplification rates in binary mixing layer. This study does not use the convective Mach number because it implies in keeps the compressible effects at $M = 0.6558$ equals for different species configurations. To maintain the convective Mach number of the hydrogen jet equal to the oxygen jet, it implies in increase its axial velocity $\bar{w}$, however this is not the objectives of this study, which aims to increase the mixing of oxygen and hydrogen changing the radii ratio Γ, the velocity ratio h and the set up of the species in a coaxial binary jet. Changes the axial velocity implies in an abrupt change of the initial configuration in an experimental setup, it implies more power to take the gas to high velocities

Although the second instability mode (Mode II), originated by the instability of the outer shear layer, is formed with different species, it is in the inner shear layer where the gradient of density actually places and where the binary effects over the growth rate must be more evident (Mode I).

Figure 5.13 shows only the growth rates of the first instability mode, Mode I, evidencing that the compressibility effects does not play a significant role in the stability characteristics. Nonetheless the species change significantly the stability characteristics, showing different behavior only by the fact of using oxygen or hydrogen, by the modification of the mass flux of the jet, an inertia effect.

Is important to note that amplification rates of the first mode formed by different species are much smaller than the homogeneous cases, being approximately one third of it, this contrast with a behavior observed in the a mixing layer, where the amplification rates when the heavier gas is located in the slow stream are the largest.

The phase velocity of both modes is presented in Figure 5.15. For Mode I, as was shown, the growth rates are very different depending the arrangement of the species. Unstable frequencies are too very different, Figure 5.14, therefore the phase velocities are very different, being higher when the oxygen is located in the inner jet, the perturbation travel at the speed of the fast stream. Contrary when the hydrogen is located in the inner jet the phase velocities are smaller. Another important comment is about the dispersive behavior of Mode II, which is much more dispersive than the Mode I.

Figure 5.13 - Effect of species configuration and compressibility (thinner lines) of the coaxial jet Mode I on instability growth rates k_i, as a function of the real wave number k_r. With $\Gamma = 2$ and $h = 0.7$.
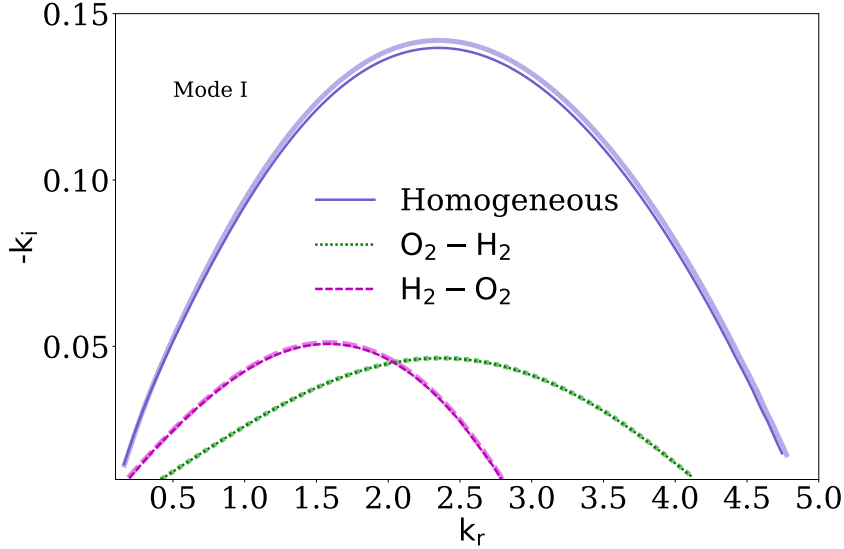
One more time, the compressible effects, when hydrogen is used as coaxial jet specie, does not play a important role at Mach number of $M = 0.6558$ for the phase velocity, Figure 5.15.

The first mode for $H_2 - O_2$ and $O_2 - H_2$ configurations, with its non-dispersive behavior and its smaller growth rates, they make this mode almost a neutral mode. It is, Mode I is only transported at the inner jet stream velocity without significant growing. This behavior will be discussed in the next Chapter 6 using high order numerical simulation.

For the Mode II is clear that lower phase velocities is achieved with the $H_2 - O_2$ configuration, being the corresponding phase velocity for homogeneous and the $O_2 - H_2$ cases are very similar, however the compressible effects are evident for the homogeneous case, contrary to the binary cases, Figure 5.12.

A special behavior is appreciated in the configuration $H_2 - O_2$ at low frequencies, the growth rates have a discontinuity in the second mode of the coaxial jet. This behavior can be associated with absolute instability, high gradients of density can induce an absolute instability behavior, as was shown by Yu and Monkewitz (1990) for jets and wakes, however this is out of the bounds of this thesis and certainly will be addressed in future works.

Figure 5.14 - Effect of species configuration and compressibility (thinner lines) on the coaxial jet Modes on instability growth rates k_i, as a function of the wave frequency ω. With $\Gamma = 2$ and $h = 0.7$.
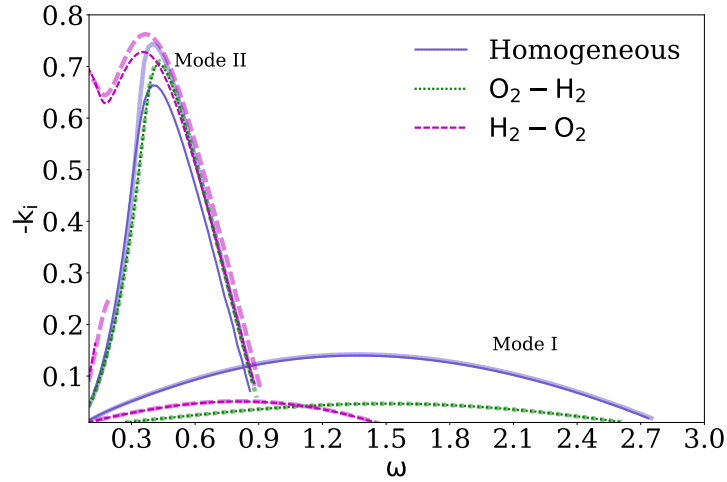
Figure 5.15 - Effect of species configuration and compressibility (thinner lines) on the coaxial jet Modes on phase velocity C_p as a function of the wave frequency ω. With $\Gamma = 2$ and $h = 0.7$.
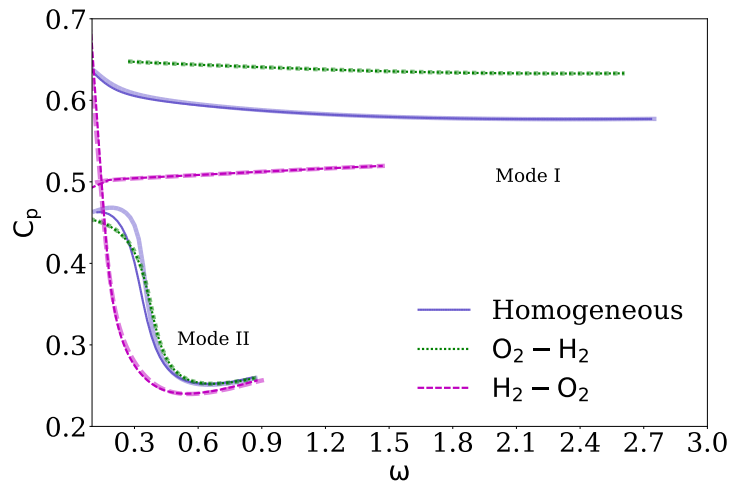
5.4.2.1 Binary coaxial jet, effects of radii ratio Γ.

As both modes are modified by use of different species using the same radii relation $\Gamma = 2.0$, the change in this relation can be used to understand the above results. Changing the radii of the external jet allows to have more of the species of the outer jets moving with its velocity. In Figure 5.16 it can be observed how changing the Γ,

61

the quantity of the species in outer jets is forced to move at the outer jet velocity, change the momentum $\bar{\rho}\bar{w}$ of the second jet stream.

Figure 5.16 - Mass fraction $\bar{Y}_1$ and $\bar{Y}_2$ base flow profiles together with base flow axial velocity profiles obtained using different Γ ratios.
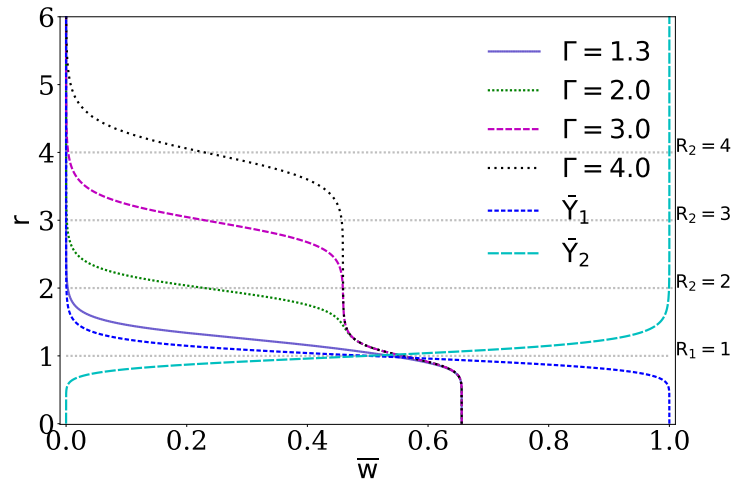
The stability characteristics of these configuration can be seen in Figure 5.17 specifically for the $H_2 - O_2$ arrangement changing Γ.

Like when the radii of the outer jet was modified, the second mode is affected in similar way, having the largest amplification rate with the $\Gamma = 2$ and decreasing with higher outer radio R_2. Is important to take into account that principles of absolute instability seems to appear for the lowest Γ ratios and practically are not found in $\Gamma = 4$.

The first mode, in Figure 5.17 Mode I, differently from what happened in the homogeneous cases, was modified by the radii relation. Its growth rates are larger than found with the $\Gamma = 2$. When more quantity of oxygen is traveling at the outer jet velocity, larger Γ ratio, achieved similar growth rates, even bigger than homogeneous case for certain frequencies, but they are not modified for $\Gamma > 3.0$.

Figure 5.17 - Effect of Γ ratio on instability growth rates k_i, of the coaxial binary jets configuration $H_2 - O_2$ as a function of the real wave number k_r. With $h = 0.7$.
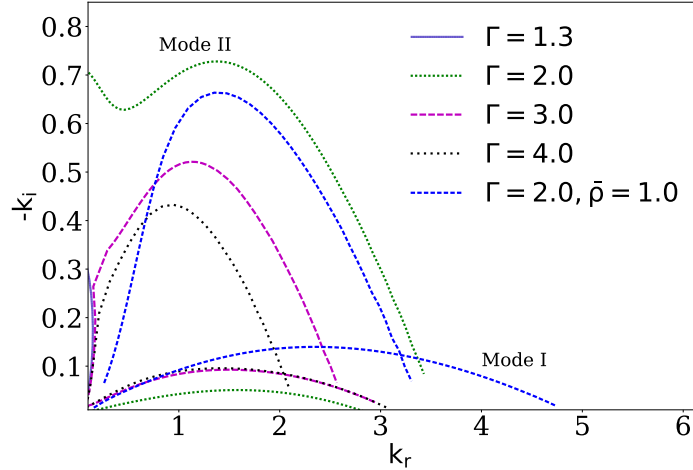
In terms of the phase velocity, for both modes there exist small different between the binary coaxial jet with different Γ ratio, attaining smaller velocities with $\Gamma = 4$ at low frequencies, this can be seen in Figure 5.18. The biggest differences in the phase velocities were found with respect to the homogeneous case, being it larger than all different configuration of $H_2 - O_2$, as was showed before for $\Gamma = 2$ in Figure 5.15. It is interesting to note that the Mode I is almost non-dispersive for all cases evaluated, contrary to Mode II, which is dispersive but in different way to the homogeneous case.

The stability characteristics changing Γ ratio specifically for $O_2 - H_2$ arrangement can be seen in Figure 5.19. This figure does not show any new information, the second instability mode is attenuated with the increment of the Γ, as happened in the homogeneous case. Contrary to what happened with the second instability mode in $H_2 - O_2$ configuration, it is not modified significantly by the radii ratio.

Is important to note that there is a important behavior when $\Gamma = 1.3$, there is only one unstable mode. When the set up of the coaxial jet is $H_2 - O_2$ this mode behaves like the second instability mode, however when the configuration is $O_2 - H_2$ this single mode behaves like the first instability mode and its growth rate are almost zero. This is consistent with Kozusko et al. (1996b) results, when the heavier species is in the faster velocity stream the amplification rates are smaller. In the homogeneous case this mode behaves like the Mode II, Figure 5.6.

63

Figure 5.18 - Effect of Γ ratio on instability characteristics of the coaxial binary jet configuration $H_2 - O_2$ as a function of the waves frequency ω, with $h = 0.7$.

(a) Growth rates k_i

(b) Phase velocity $C_p = \omega/k_r$

Figure 5.19 - Effect of Γ ratio on instability characteristics of the coaxial binary jet configuration $O_2 - H_2$ as a function of the waves frequency ω. With $h = 0.7$. $\bar{\rho} = 1$ is the homogeneous case, using for comparison reasons.
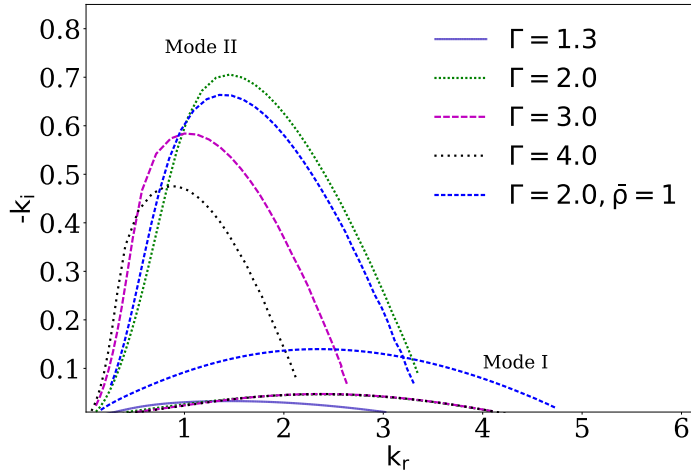
Regarding phase velocity presented in Figure 5.20, for the second instability mode the small velocities are reached by the larger ratio at low frequencies and for the first instability mode all velocities are very similar to the inner jet axial velocity, showing how this mode does not modified the behavior of the coaxial jet in this particular arrangement $O_2 - H_2$. Again the Mode I is less dispersive than the Mode II.

64

Figure 5.20 - Effect of Γ ratio on instability characteristics of the coaxial binary jet configuration $O_2 - H_2$ as a function of the waves frequency ω, with $h = 0.7$.

(a) Growth rates

(b) Phase velocity
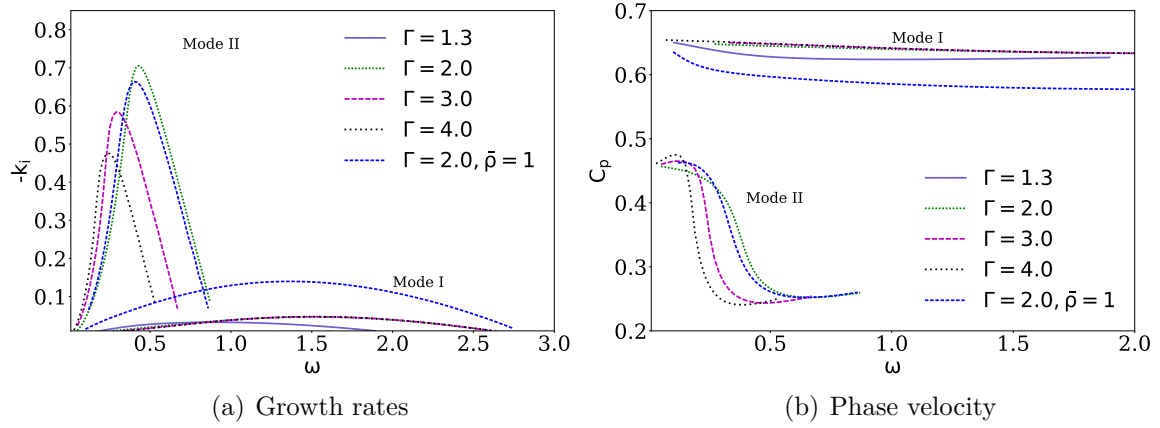
In order to conclude the analysis of the role of Γ in binary coaxial jet and to show which has the largest amplification rates that will allow to improve of the mixing between the oxygen and hydrogen, Figure 5.21 compare the most relevant cases for the both unstable modes.

Figure 5.21 - The most relevant cases evaluated to illustrate the effect of Γ ratio on of the coaxial binary jet as a function of the waves frequency ω. With $h = 0.7$.

(a) First Instability mode, Mode I

(b) Second Instability mode, Mode II
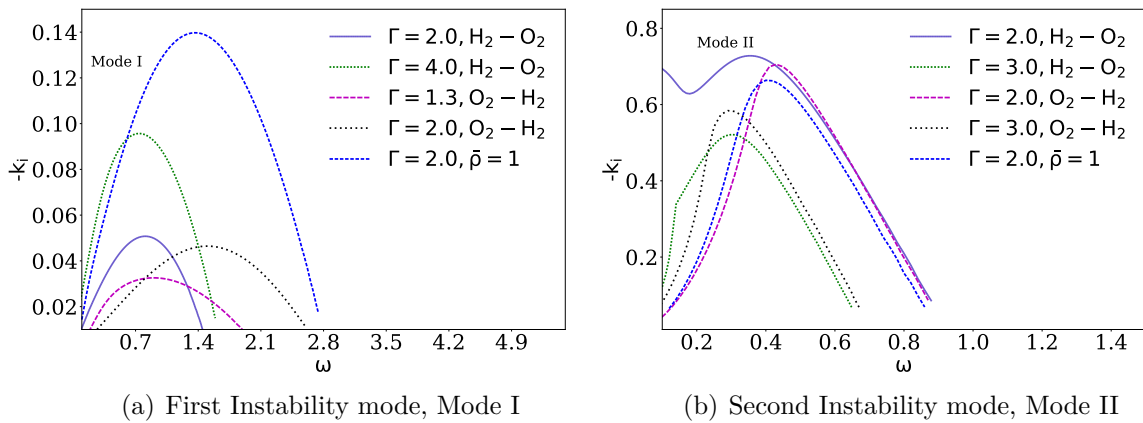
In Figure 5.21, it is evident that the biggest amplification rates are reached when

65

the oxygen in situated in the slower jet stream, in the outer jet, which is consistent with results founded in a mixing layer by Kozusko et al. (1996b).

However in the first instability mode, the homogeneous case shows larger growth rates. This behavior can be explained by the finite quantity of species that can be place in a coaxial configuration, in mixing layer both stream are infinite.

For the second mode this limitation is less evident because it is formed by almost a homogeneous density profile, which is also infinity on one side. Nonetheless the influence of the species in the growth rates in this mode are evident, achieving the largest amplification rates with $\Gamma = 2$ and apparently with the onset of absolute instability.

When the oxygen is located in the fast stream the amplification rates are the smallest, leading to the almost annihilation of Mode I and smaller growth rates of Mode II, when compared with the other results.

5.4.2.2 Binary Coaxial jet, effects of velocity ratio h.

After the effects of Γ ratio were verified in binary coaxial jet, the effects of the velocity ratio will be presented. As was done for homogeneous case, with constant density profile, different h relation were evaluated using two binary configurations with oxygen and hydrogen. Figure 5.22 shows different h ratios in a $H_2 - O_2$ configuration and are compared with the most unstable case of a homogeneous coaxial jet, $\bar{\rho} = 1$. Differently than happened in the homogeneous cases the change in the h changes notably the growth rates and the behavior of the second instability mode. Increasing h the amplification rates decrease, being similar to the unchanged Mode II of the homogeneous cases, however the traces of absolute instability are present in low frequencies.

In relation to Mode I, as was observed with the radii relation, the biggest amplification rates are reached with the homogeneous case, but its interesting to note as the h relation modified preferably the first mode, its increase make this mode decrease until disappear for $h = 0.9$.

The phase velocity, Figure 5.23, as was expected with the smaller h ratios allows the perturbation to travel slower, this apply to both modes. Its interesting highlight the $h = 0.5$ case, which was the lowest velocity reached for the Mode I in this work both for binary as homogeneous coaxial jet. For $h = 0.9$ the neutral waves travel at high velocity of the coaxial jet. Again Mode II is more dispersive in relation to the

behavior almost non-dispersive of Mode I when a binary coaxial jet are considered.

Figure 5.22 - Effect of h ratio on instability characteristics of the coaxial binary jet config-
uration $H_2 - O_2$ as a function of the waves frequency ω. With $\Gamma = 2$. $\bar{\rho} = 1$
is the most unstable homogeneous case for Mode I, using for comparison
reasons.
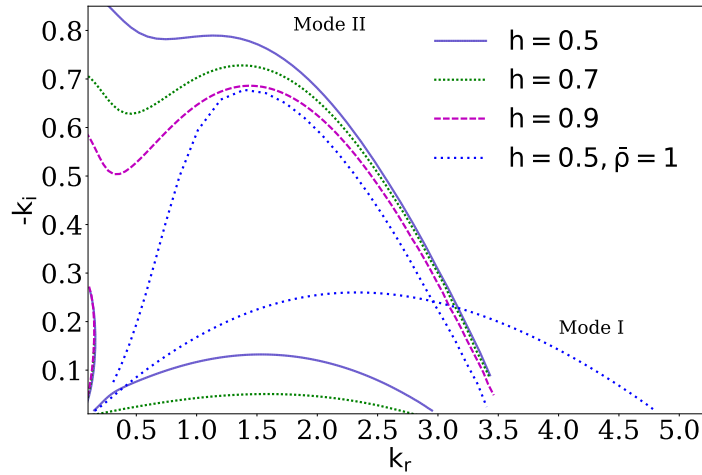
The effect of the confinement, induced by the coaxial configuration, can be dimin-
ished using $\Gamma = 4$ with the $h = 0.5$, the increment of the growth rates is evident,
Figure 5.24a. The first instability mode is larger than with $h = 0.7$, which has
the biggest amplification rates for Mode I founded in this investigation for binary
configurations.

The modification of Γ change the second mode, as shown in Figure 5.24b, where the
amplification rate is reduce considerably.

Figure 5.23 - Effect of h ratio on instability characteristics of the coaxial binary jet con-
figuration $H_2 - O_2$ as a function of the waves frequency ω, with $\Gamma = 2$. $\bar{\rho} = 1$
is the most unstable homogeneous case for Mode I, using for comparison
reasons.

(a) Growth rates k_i.

(b) Phase velocity $C_p = \omega/k_r$.
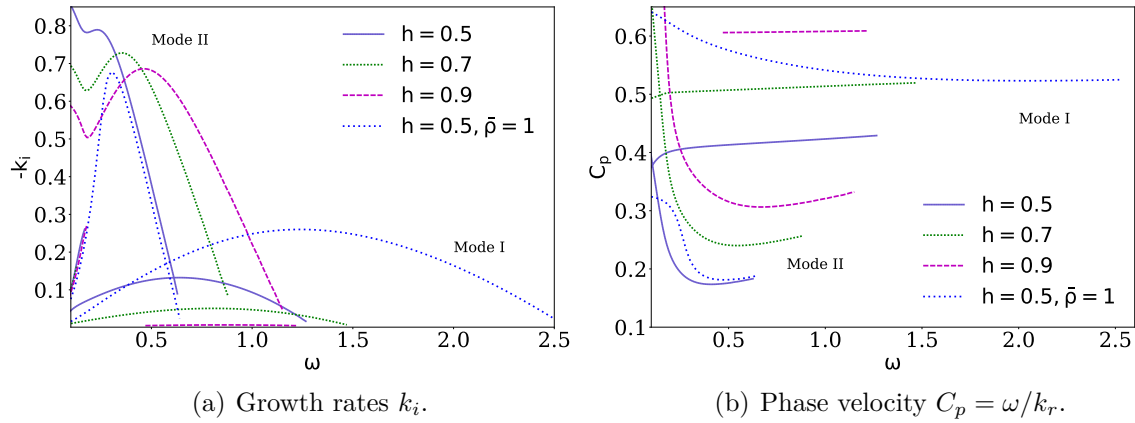
Figure 5.24 - Effect of h ratio on instability characteristics of the coaxial binary jet con-
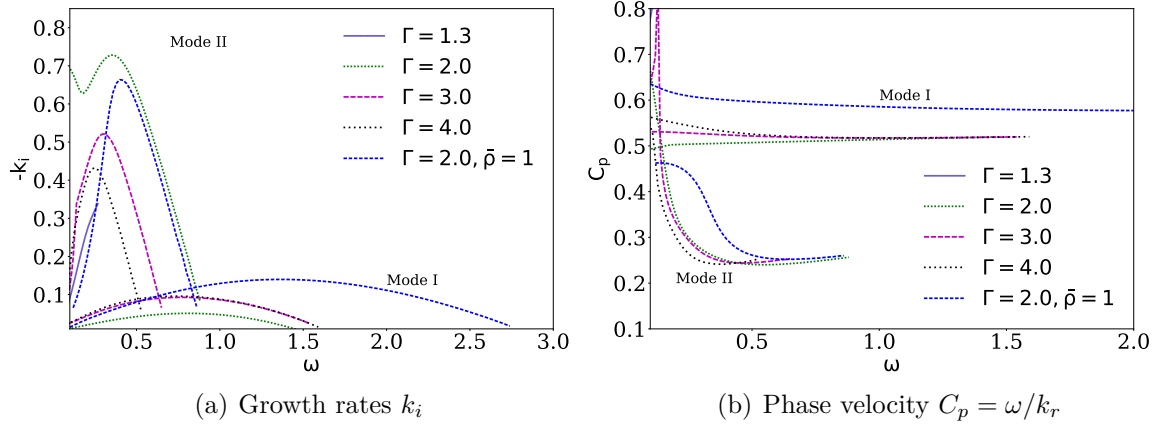figuration $H_2 - O_2$ as a function of the waves frequency ω, with $\Gamma = 2$. $\bar{\rho} = 1$
is the most unstable homogeneous case for Mode I and $\Gamma = 4$ with $h = 0.5$
has the most unstable mode I, both used for comparison reasons.

(a) Growth rates k_i.

(b) Phase velocity $C_p = \omega/k_r$

68
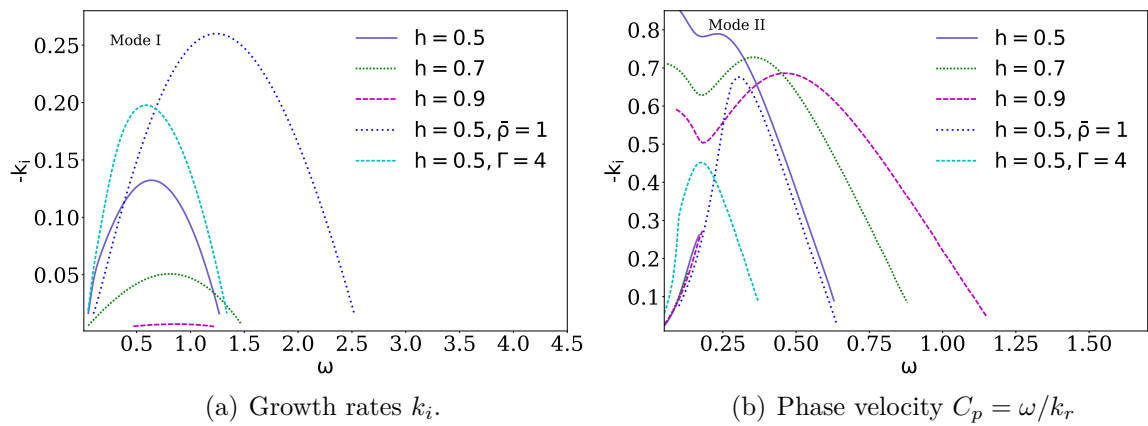
Changing to the $O_2 - H_2$ configuration, Figures 5.25 and 5.26, the stability charac-teristics are not modified differently than have happened before, the only mode that is affected with the change of h ratio is Mode I and the amplification rates compared are smaller respect to the homogeneous and $H_2 - O_2$ cases. The second instability mode does not change notably, staying very similar in all cases evaluate, showing difference in the maximum frequency where the maximum amplification rate occurs 5.26a, like in homogeneous case. In the phase velocity the same behavior is observed, increasing with the increment of h and showing as the first mode when $h = 0.9$ is a neutral wave that travel at the inner jet velocity, Figure 5.26b.

Figure 5.25 - Effect of h ratio on instability characteristics of the coaxial binary jet config-uration $O_2 - H_2$ as a function of the waves frequency ω, with $\Gamma = 2$. $\bar{\rho} = 1$ is the most unstable homogeneous case for Mode I, used for comparison reason.
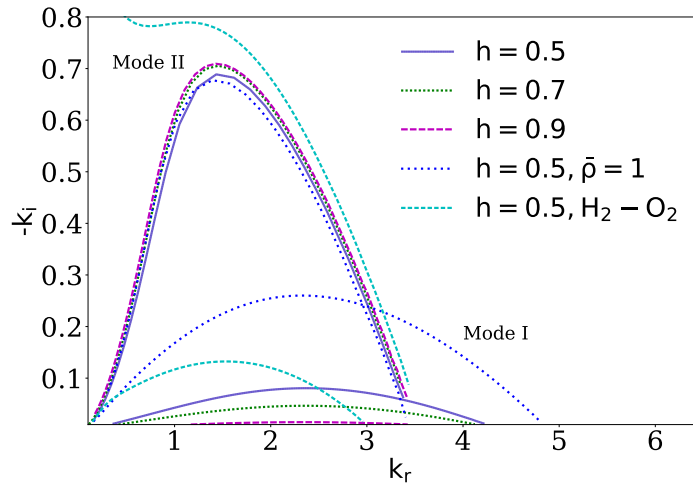
To conclude the effects of the h ratio, the most unstable case of the $H_2 - O_2$ and homogeneous case, both with $h = 0.5$ and $\Gamma = 2$, were also compared with the above results and presenting in Figures 5.25 and 5.26. These figures show that the growth rates are always less pronounced in relation to the homogeneous case and with $H_2 - O_2$ configuration. There was no need to compared with other Γ because in this configuration the only effect is felt in the second instability mode, which is less unstable. Then, when the oxygen is placed in the faster jet stream ($O_2 - H_2$) the first mode is smaller with the larger h, as happened in the other cases, but with the difference that the amplification rate of this configuration are always smaller.

Figure 5.26 - Effect of h ratio on instability characteristics of the coaxial binary jet con-
figuration $O_2 - H_2$ as a function of the waves frequency ω, with $\Gamma = 2$. $\bar{\rho} = 1$
is the most unstable homogeneous case for Mode I, and $H_2 - O_2$ case with
$h = 0.5$ is the most unstable mode, both used for comparison reasons with
$\Gamma = 2$.

(a) Growth rates k_i.

(b) Phase velocity $C_p = \omega/k_r$.
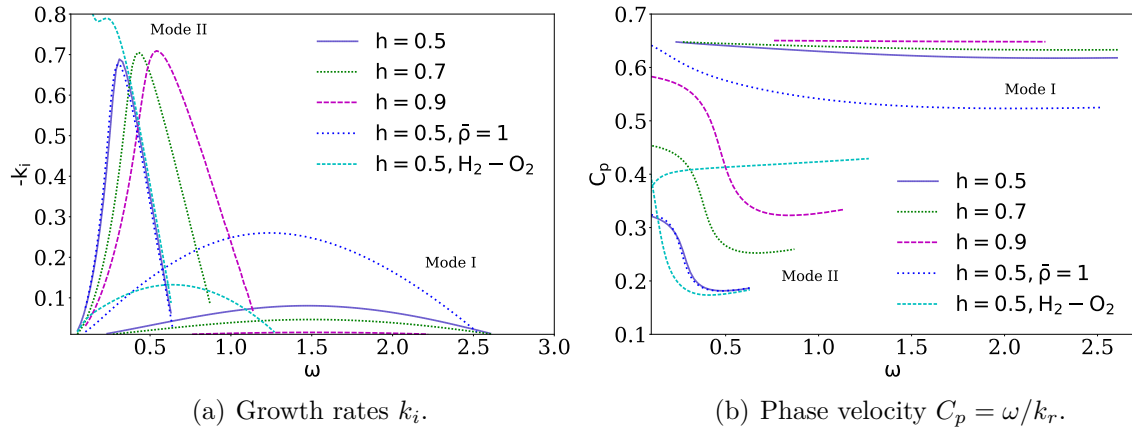
Considering the second instability mode, its instability characteristics does not
change, the growth rates are very similar to the homogeneous case, but ever smaller
that $H_2 - O_2$ coaxial jet configuration.

6 HIGH ORDER NUMERICAL SIMULATION

In this Chapter, using High Order Simulations (HOS) of the Euler equations, the vortical structures present in both homogeneous and binary coaxial jets will be investigated. The description and the verification of the numerical code will be present in the next section.

6.1 Numerical code and verification.

The numerical code was developed using low dissipation, low dispersion, high order numerical methods, to represent appropriately the waves characteristics of the instabilities development. The spatial discretization uses a 4th order Dispersion Relation Preserving finite difference (DRP) proposed by Tam and Webb (1993). This is a central scheme with 7 points, which coefficients were calculated in order to decrease the dispersive error of the central difference traditional scheme. The coefficients were optimized for a wave number band between 0 and $\pi/2$ by Tam and Webb (1993) and are defined as:

$$a_0 = 0, \quad a_1 = a_{-1} = 0.79926643,$$
$$a_2 = a_{-2} = -0.18941314, \quad a_3 = a_{-3} = -0.02651995. \tag{6.1}$$

For the temporal advancement a 6 steps, low storage Runge Kutta specialized in non-linear operator implemented by Berland et al. (2006) was used. The algorithm of this method is defined

$$\left.\begin{array}{c} \omega_i = \alpha_i \omega_{i-1} + \Delta t F(u_{i-1}, t_i) \\ u_i = u_{i-1} + \beta_i \omega_i \end{array}\right\} \quad \text{for} \quad i = 1...s \tag{6.2}$$

where $\partial u / \partial t = F(u, t)$, Δt is the time step and s is the number of steps. $u_0 = u_n$, $u_{n+1} = u_s$, $\omega_0 = 0$ and $t_i = (n + c_i)\Delta t$. α_i and β_i are the coefficients of the algorithm defined in Berland et al. (2006).

Non-reflecting boundary conditions (NRBC) were implemented to avoid reflections of outgoing waves at the boundaries of the computational domain. More specifically a buffer Zone proposed by Wasistho et al. (1997) was used. The buffer zone is based on numerical damping and requires to increase the domain, including zones where

the numerical damping will be applied. Within it the amplitude of outgoing waves is damped to a value determined by a damping function. The NRBC were implemented in inflow, outflow and upper boundaries as shown in Figure 6.1 and its size is defined by the parameters D_r and D_z, that represent the number of mesh point in radial and axial direction, respectively.

Within the buffer zone the amplitude of outgoing waves is damped to a value determined by a damping function σ. Defining $\overline{\mathbf{u}}^n = (\rho, u, w, p, Y_i)$ as the solution vector at each time step, the buffer zone can be applied as:

$$\mathbf{u}^{n+1} = \overline{\mathbf{u}}^{n+1} - \sigma(\overline{\mathbf{u}}^{n+1} - \mathbf{u}_{\text{target}}). \tag{6.3}$$

Where $\mathbf{u}^{n+1}$ is the solution vector for each time step after the application of the damping. The $\mathbf{u}_{\text{target}}$ used in (6.3) sets the required value $\overline{\mathbf{u}}$ on the buffer zone, which is defined depending on the problem. For the linearized Euler equations $\mathbf{u}_{\text{target}}$ is set to zero so that the perturbation that enters the buffer zone is removed from the base flow. For non-linear Euler equations $\mathbf{u}_{\text{target}}$ can be defined as the base flow for instantaneous variables.

For the buffer the absorption coefficient σ applied was based on Wasistho et al. (1997):

$$\sigma_n = (1 - C_1 n_b^2)\left(1 - \frac{1 - e^{C_2 n_b^2}}{1 - e^{C_2}}\right) \qquad \text{with,} \qquad n_b = \frac{n - n_s}{n_e - n_s}, \tag{6.4}$$

where n_s and n_e are points on the domain corresponding to the beginning and end of the damping zone, n represents the coordinates r and z, depending on the direction of application of the boundary condition. C_1 and C_2 define the transition mode of σ within the buffer zone, and are set as $0 \leqq C_1 \leqq 0.1$ and $10 \leqq C_2 \leqq 20$. For the buffer NRBC implementation the following grid stretching is used

$$\frac{\partial}{\partial n} \quad \rightarrow \quad \frac{1}{\alpha(n)}\frac{\partial}{\partial n}, \tag{6.5}$$

where n represents the coordinate direction r or z according to the direction of application of the NRBC and $\alpha(n)$ is a stretching function:

$$\alpha(n) = 1 + 2 \left| \frac{n - n_0}{D_n} \right|^2 . \tag{6.6}$$

n_0 represents the point where stretching zone begins.

The mesh used to numerical simulations is uniform in the core where the Euler equations are resolved, Figure 6.1. The above stretching is applied only in the NRBC.

At the center of the coaxial jet, $r = 0$, a special boundary condition necessary to consider an axisymmetric coaxial jet. To it, the half-mesh displacement method proposed by Tam and Fan () was used. A 4th order 13 points low dispersive and low dissipative explicit selective filter was implemented following the work of Bogey and Bailly (2004), to avoid the grid-to-grid oscillations caused by the use of central finite difference schemes. This filter remove the short waves without affecting the instability long waves, that in this case are the Kelvin-Helmholtz.

The master thesis of Manco (2014) presents the complete development of the numerical tools, where the reasons to choose this numerical schemes and which type of non-reflecting boundary condition is recommended to use in the numerical simulation of a unstable mixing layer. The choice for these numerical schemes are mainly based on particular aspects of the numerical simulation of unstable mixing layer.

The numerical code was written in Fortran, using Message Passing Interface (MPI) with a cartesian decomposition of the domain. The code was implemented to run at the Centro de Previsão do Tempo e estudos Climaticos (CPTEC-INPE) supercomputer Cray XT-6. The supercomputer, called TUPÃ (THUNDER in the Guarani language), has 256 teraflops of capacity, distribute in 14 cabinets of 1.304 nodes and 31.296 processors.

Figure 6.1 - High order simulation domain and boundary conditions.
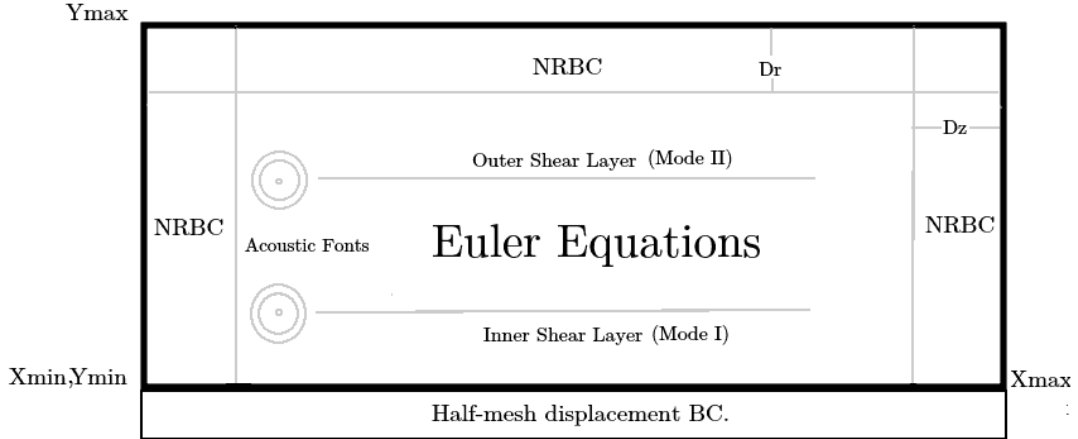
To verify the HOS of Euler equations the linear stability theory (LST) developed in Chapter 5, was used. To this end the special cases of coaxial jet where only one mode is presented, $\Gamma = 1.3$ for the homogeneous and $\Gamma = 2$ for $O_2 - H_2$ cases were used. These test cases were chosen to separate the two different modes presented in a HOS of the coaxial jet, using an acoustic pulse to exited these modes is a difficult task.

An acoustic pulse is used in order to excite the hydrodynamics instabilities for both the inner and the outer mode. The acoustic disturbance is applied as source term in the pressure energy equation and it has the form:

$$s(r, z, t) = -A_0 sin(\omega t) \exp\left[-ln(2)\left(\frac{(x + x_b)^2 + (y + y_b)^2}{\delta_b}\right)\right]. \qquad (6.7)$$

The variable A_0 is the amplitudes and δ_a is the thicknesses for the acoustic pulse. The positions x_b and y_b are the points of application of the different pulses. The frequency of of the disturbance is ω. All pulses used in this work have unitary amplitude, a thickness of $\delta_b = 0.03$ and were located at the origin of the domain $(z = 0)$ at the inner $(r = 1.0)$ and outer $(r = 2.0)$ shear layers positions.

The $H_2 - O_2$ case was not used for validation because of the existence of possible absolute instability, the amplification rate will have a different behavior and the linear growth of the instabilities exclusively in space or time is not expected. In absolute instability both, space and time, growing are important.

An important point to highlight is that the minimum Mach number that is supported by the HOS code is $M_\infty = 0.1$. This is due to the stiffness of the Euler equations when the magnitude of the velocity is small compared with the sound velocity. The local time step is limited by the fastest wave or eigenvalue, by the CFL condition, whereas the the slowest wave are propagated only a fraction in the mesh, such that the convergence time is high. As the solution can be modified by the numerical errors, the convergence a low mach number code is difficult to achieve without used of a preconditioning schemes or a Low Mach number formulation.

To this end a base flow the one used in Chapter 5 was modified as

$$\bar{w} = (M_i - M_o)w_1 + M_o w_2 + M_\infty w_3 \tag{6.8}$$

where

$$w_n = \frac{1}{2}\left\{1 + tanh\left[b_n\left(\frac{R_n}{r} - \frac{r}{R_n}\right)\right]\right\} \quad n = 1, 2, 3. \tag{6.9}$$

The parameters M_i, M_0 and M_∞ are the inner jet mach number, the outer jet mach number and the coflow ambient Mach number, respectively.

Although the base flow is different from that used in Chapter 5, the main conclusions achieved with the linear stability theory can be reproduced. Figure 6.2 shows the differences between the base flow profiles used in the high order simulation and the one used in the LST Chapter. The requirement of a minimum Mach number for HOS implies the used of a coflow with $M_\infty = 0.1$.

Due to the coflow, as presented in Figure 6.3, the second unstable mode (Mode II) is modified, decreasing the growth rates. However the maximum amplification rate is found at the same frequency. Whereas Mode II is modified, Mode I does not change due to the coflow.

Figure 6.2 - Differences between the axial base flow velocity used for the high order simulation and the linear stability theory due the coflow. $h = 0.7$, $\Gamma = 2$ and $M_\infty = 0.1$.
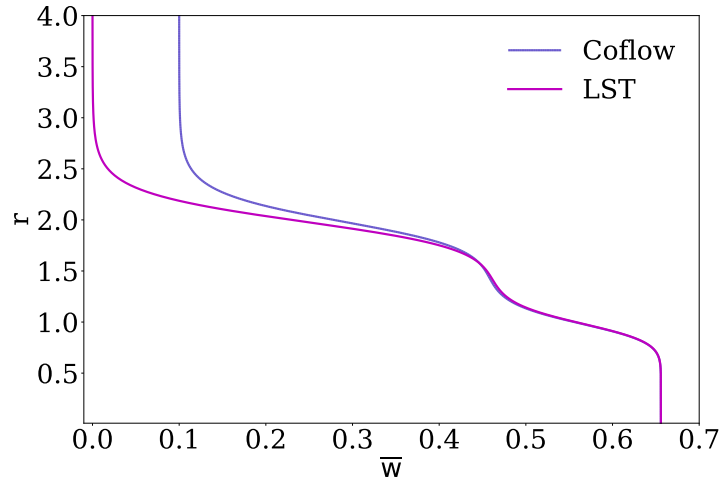
Figure 6.3 - Effect of coflow on instability growth rates k_i, of the coaxial jet as a function of the waves frequency ω, with $\Gamma = 2$ and $h = 0.7$.
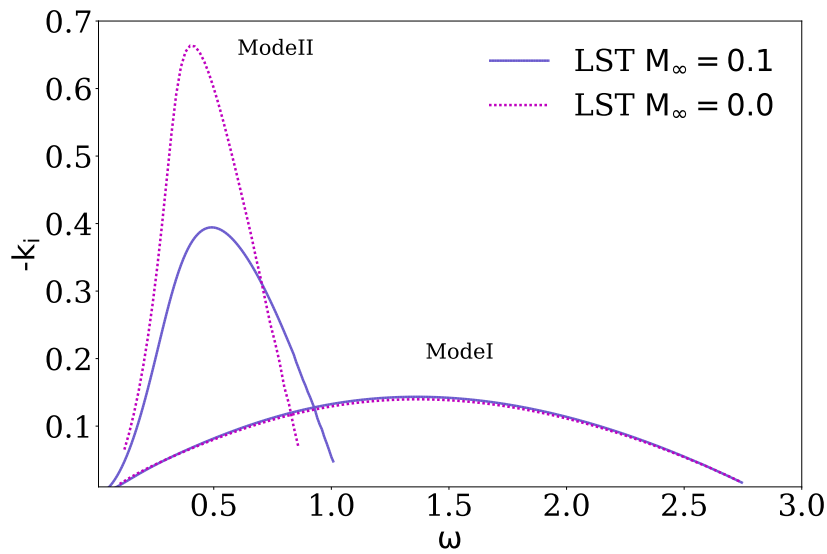
The parameters of the numerical methods used in the verification of the high order simulation are presented in Table 6.1.

The growth rates calculate by the HOS and the LST are presented in Figure 6.4.

Table 6.1 - Parameters of the numerical schemes used in HOS.

Parameters High Order Simulation	
Domain size [r,z]	[0:5,-3.5:24.5]
Filter parameter α	0.1, applying each time step.
Size NRBC $D_r = D_z$	80 mesh points
Parameters NRBC	$C_1 = 0.01$, $C_2 = 20$, $C_3 = 50$
MPI process	16x12

These were calculated by HOS using an instantaneous approximation, where the base flow is subtracted from the solution to find the perturbation variables. Once the perturbation variables are found their perturbation kinetic energy $e_k = u'^2 + w'^2$ can be calculated assuming exponential growth, similar to the LST. This linear growth of the perturbation can be achieved in HOS when the non-linearities are sufficiently small, then the vortices are not completely developed.

The perturbation kinetic energy can be calculated by

$$e'_k = u'^2 + w'^2 = u(r)e^{2i(k_i z - \omega t)} + w(r)e^{2i(k_i z - \omega t)}, \qquad (6.10)$$

differentiating the above equation in relation to z

$$\frac{\partial e'_k}{\partial z} = 2ik_i u'^2 + 2ik_i w'^2. \qquad (6.11)$$

Then, is possible to find the amplification rate if the gradient of the kinetic energy in the high order simulation is calculated, so that

$$k_i = \frac{1}{2e'_k}\frac{\partial e'_k}{\partial z} = \frac{1}{2}\frac{\partial}{\partial z}\left(ln(e'_k)\right). \qquad (6.12)$$

To calculate the kinetic energy the Fourier transform was used to removed the oscillatory behavior of the solutions.

Figure 6.4 - Growth rates k_i, of coaxial binary jet calculate with HOS ans LST as a function of the waves frequency ω, with $h = 0.7$ and $M_\infty = 0.1$.

(a) Growth rates k_i, homogeneous case $\Gamma = 1.3$ (b) Growth rates k_i, $O_2 - H_2$ case, $\Gamma = 2$
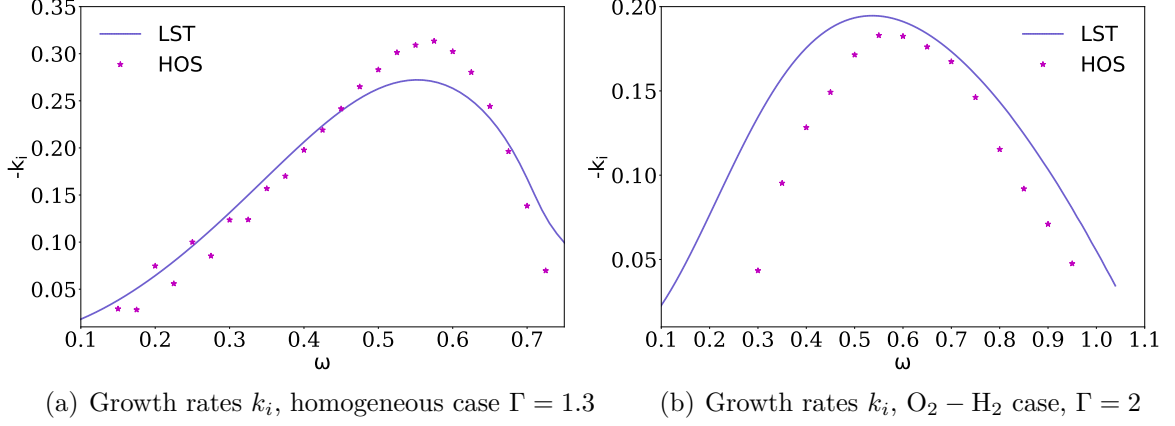
In Figure 6.4 the LST and the HOS show a good agreement , with similar behavior. The differences on the growth rates are due to the use of instantaneous approach, where, to find the perturbation field it is necessary to subtract the initial base flow for the ongoing solution, as $p' = p - \bar{p}$. Once, the base flow is also a solution of the non-linear Euler equations in an instantaneous approach, the initial canonical profiles imposed as initial conditions is different from the Euler base flow profile.

If only the perturbation variables are solved, it is assumed that the base flow remains unaltered, and the agreement between the LST and HOS is very good as can be seen in Figure 6.5. In this figure several computational meshes were used to evaluated the agreement between the LST and the HOS in hight frequencies.

It is clear that with a more refined mesh, hight frequency waves are better resolved and the results between the codes are better.

The next section will show the results of the verified numerical code for the simulation of homogeneous coaxial jets using the instantaneous approach.

6.2 Homogeneous coaxial jet

First the results of the HOS simulation are presented, using the instantaneous approach, for the cases presented in linear stability Chapter 5, with homogeneous flows presented by Perrault-Joncas and Maslowe (2008) changing the parameter Γ and h.

78

Figure 6.5 - Growth rates k_i, of coaxial binary jet calculate with HOS ans LST as a function of the waves frequency ω, with $h = 0.7$ and $M_\infty = 0.1$.
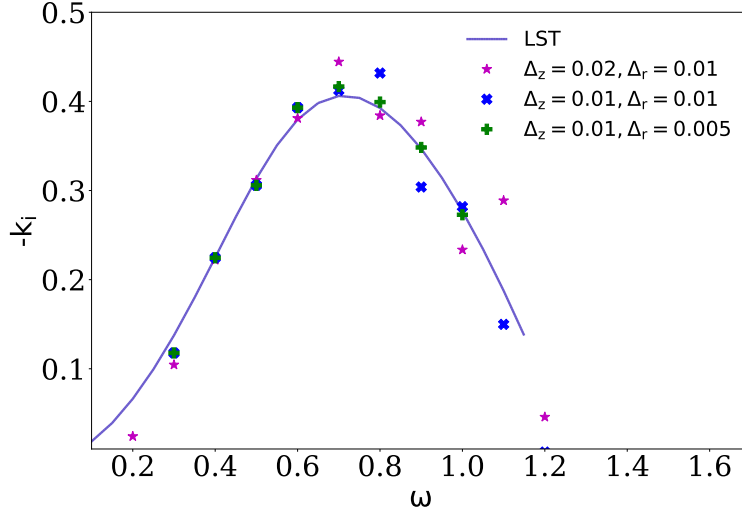
Although this cases were studied completely with the LST, the vortical structures and flow configuration in the non-linear regime can be analysed with HOS.

The color map used for contour visualization of a specified variables was chosen based in the work of Moreland (2009), where a good default color map for general purpose scientific visualization is discussed, and the use of the diverging color map is suggested. Diverging color map use two main colors with a unsaturated color, white, in the middle. The default colour map, rainbow color map, used in almost majority of fluid visualization which use saturated colors, "is well known for its ability to obscure data, introduce artifacts, and confuse users", Moreland (2009). The rainbow color map is confusing due to fact that it does not have perceptual ordering and it actively mislead the viewer by introducing artifacts to the visualization. On the other hand, diverging color maps is useful because it divides the date values into three regions: low, mid range, and high values. This is appropriated to visualization of the perturbation variables, which have small variation, positive or negative, around the base flow.

To allow a good visualization of the vortices the most unstable frequencies for each mode were used. To find these unstable frequencies the LST was used with the base flow define in equation 6.8, all cases simulate in the next section were evaluated with the linear stability theory.

The first homogeneous case simulated is shown in Figure 6.6, with $\Gamma = 2$ and $h = 0.7$. The most unstable frequencies of this configuration are $\omega = 0.5$ and $\omega = 1.35$ for Mode I and Mode II, respectively.

The variable plotted in Figure 6.6 is the density contour. This is because it is the appropriate variable that also allows to view the change of species when a binary coaxial jet is simulated, and also allows to view the vortical structures. In this figure it is clear the appearance of the two unstable modes of homogeneous coaxial jet, and internal mode and outer mode. The most unstable mode is the second mode, presenting the well known Kelvin-Helmholtz vortices (K-H). It is important to comment that the amplification rate of Mode II will be higher if a coflow is not considered and may interact non-linearly with Mode I, increasing the mixing of the jet streams if the original base flow was evaluated.

Contrary to the strong development K-H of the second mode, the first mode, that has small amplification rate, needs a larger domain to develop as a K-H instability. However, one of the motivation of this study is to find the instability characteristics that provide the largest amplification rate to improve the mixing between oxygen and hydrogen in a coaxial jet injector and this homogeneous cases will be used as reference cases.

Figure 6.6 - Density contour of homogeneous coaxial jet, showing the two unstable modes with $\Gamma = 2$ and $h = 0.7$.
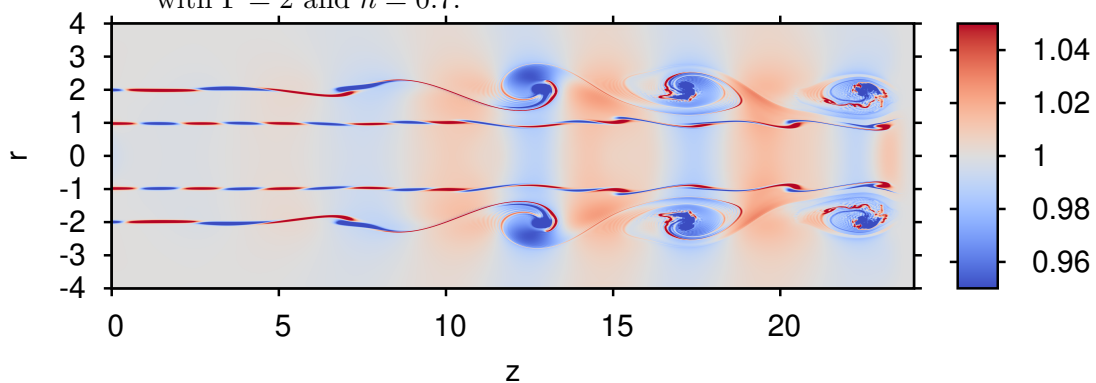
As was done in Chapter 5, the change of instabilty characteristics with parameters Γ and h, which control the the first and second unstable modes respectively, was verified with the density contour presented in Figures 6.7 and 6.8.

In Chapter 5, LST, the radii ratio $\Gamma = 1.3$ produces only one unstable mode and the

behavior of the coaxial jet is like a single jet, Figure 6.7a. This single mode develops at the inner shear layer and can be classified as a Mode I. Although the second mode is not present, this single mode can be very useful to mix the two species.

Increasing the radii ratio Γ, Mode I remains unaltered , whereas the amplification rate of Mode II decreases. The development of the unstable mode is slow, resulting in a complete vortical structure at the end of the computational domain used. This is evident in the density contours with $\Gamma = 4.0$ shown in Figure 6.7b.

Figure 6.7 - Vortical structures of coaxial homogeneous jet shown using density contour for different radii ratio Γ, with velocity ratio of $h = 0.7$.
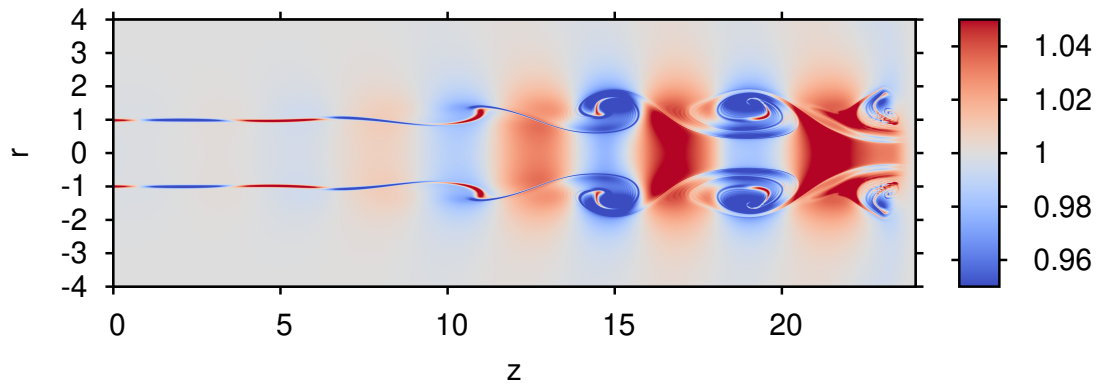
(a) $\Gamma = 1.3$
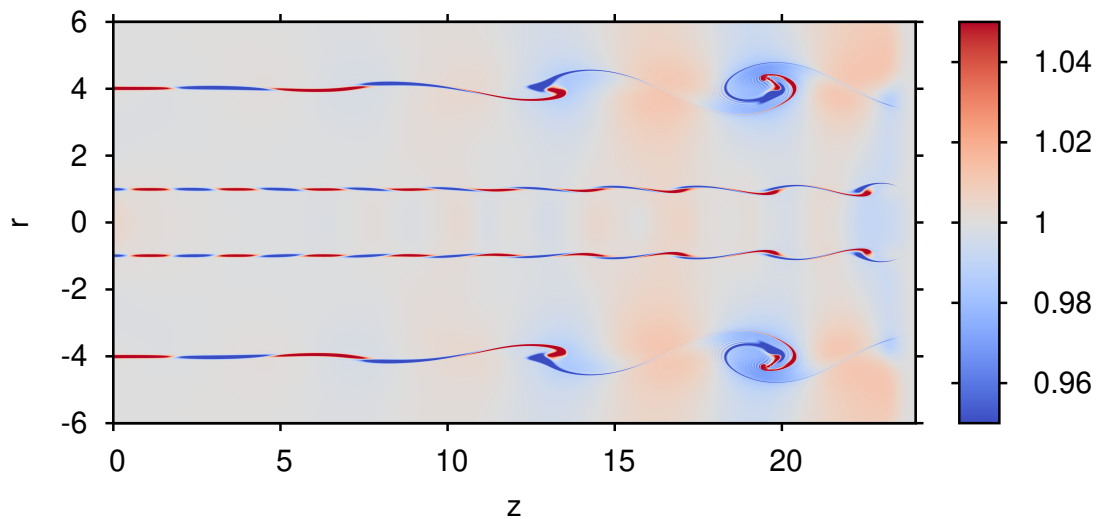
(b) $\Gamma = 4$

In the case of changes in the velocity ratio, the growth rates of the inner mode are expected to be larger with the smallest ratio, $h = 0.5$. While for the largest

velocity ratio, $h = 0.9$, the growth rates of Mode I are smaller, lending it to almost extinction. This behavior is presented in Figure 6.8.

The second mode remains unaltered when h is changed but the phase velocity changes considerably as was shown in the linear stability Chapter 5, being slower with $h = 0.5$ and faster with $h = 0.9$. Figure 6.8 shows that the vortical structures do not develop further downstream for $h = 0.5$, it is due the slower phase velocity of this structures, whereas for $h = 0.9$, Figure 6.8, the vortices are more intense.

Figure 6.8 - Vortical structures of coaxial homogeneous jet shown using density contour for different velocity ratio h, with radii ratio of $\Gamma = 2$..
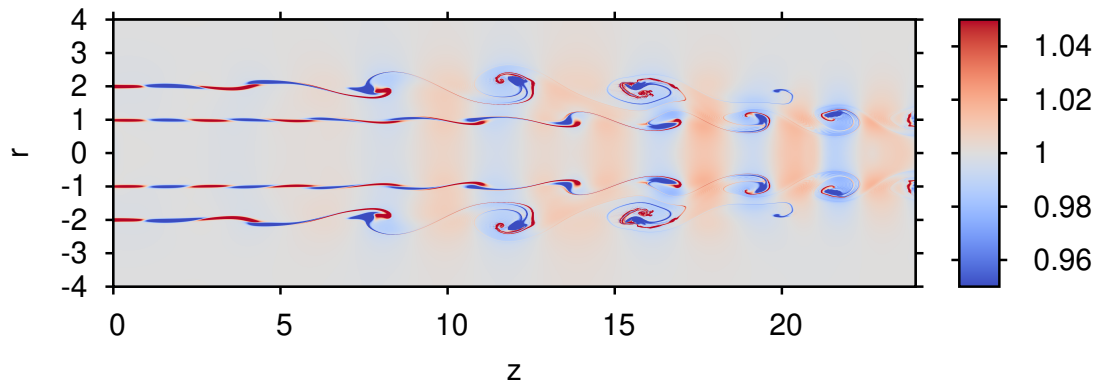
(a) $h = 0.5$
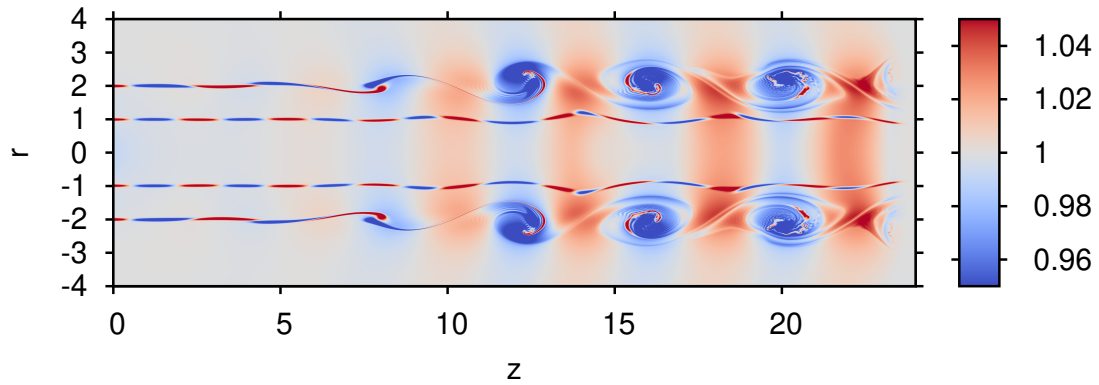
(b) $h = 0.9$

This apparent higher intensity of the vortical structures of the second mode with $h = 0.9$ induces to think that this mode is more unstable with relation to the $h = 0.5$ and $h = 0.7$ cases, which is contradictory to the LST results, where all cases have the same growth rates. Figure 6.9 shows the comparison of the density, axial velocity and vorticity contours for $h = 0.7$ and $h = 0.9$. This figure uses the axisymmetric of

the coaxial jet, to show for $r > 0$, the $h = 0.7$ case and for $r < 0$, the $h = 0.9$ case.

Figures 6.9a and 6.9b compared the $h = 0.7$ and $h = 0.9$ cases showing that they are very similar and the vortical structures, Figure 6.9c, are almost identical with the same amplification rate. The only differences are founded in the phase velocity and hence in the wave number k_r, as was shown in the LST results 5.8. The axial velocity contours Figure 6.9b, for both cases shows small differences, but it is clear that it is due to the high velocities of the second jet stream with $h = 0.9$. This can also be seen in the base flow, Figure 5.7.

A special case is found with $h = 0.5$ that results in a large growth rate of the inner mode, without modification of the outer mode with respect of $h = 0.7$ and $h = 0.9$ cases, a possible interference between these two modes may result. Firstly, the same case with different frequencies, the maximum and the minimum growth of Mode I, were evaluated and shown in Figure 6.10, this with the intention to see if the first mode interferes in the development of the second mode. The interference is clear, showing that the second mode is modified, flattening the vortical structures.

It is important to comment that, Figure 6.10 correspond to $t = 100$, different from $t = 70$ used in the previous figures. This is necessary to the complete development of the vortical structures due to the low phase velocity of the outer K-H structures reached with $h = 0.5$.

A longer simulation time, $t = 160$, shows that when the non-linear interaction between the inner and outer mode is observed the vortical structures of the second mode leads to a breakdown, Figure 6.11.

6.3   Binary coaxial jet

In order to shown the binary effects on the vortical structures of unstable coaxial jets the most relevant cases founded with the linear stability theory were evaluated with High Order Simulations. The cases simulated were those with larger growth rates in LST analysis, both for the system $H_2 - O_2$ and $O_2 - H_2$, with different radii ratios Γ and different velocity ratios h.

In this case the most important parameter is the mass fraction Y_i of the species, which shows how the species are mixing due to the instabilities, which have as the principal role to combine the oxygen and the hydrogen.

The LST shows that there are different cases where the growth rates of the unstable

Figure 6.9 - Vortical structures of coaxial homogeneous jet shown using density, velocity
and vorticity contour for velocity ratio $h = 0.7$ and $h = 0.9$, with radii ratio
of $\Gamma = 2$. For $r > 0$ are shown the properties with $h = 0.7$ and for $r < 0$ with
$h = 0.9$ velocity ratio.
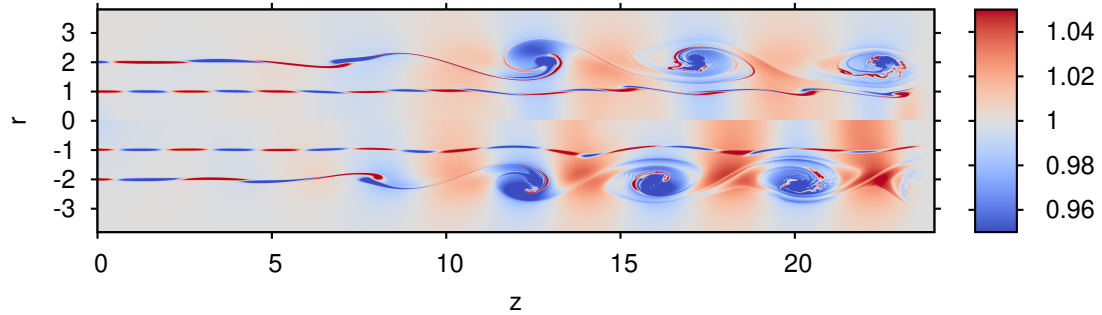
(a) Density ρ.
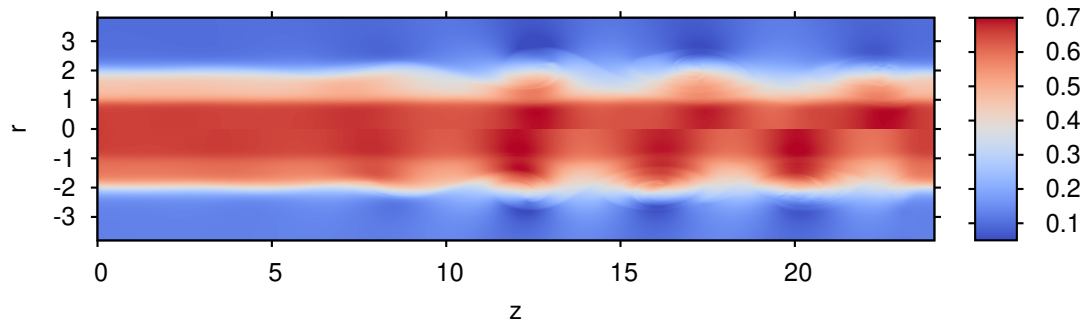
(b) Axial velocity w.
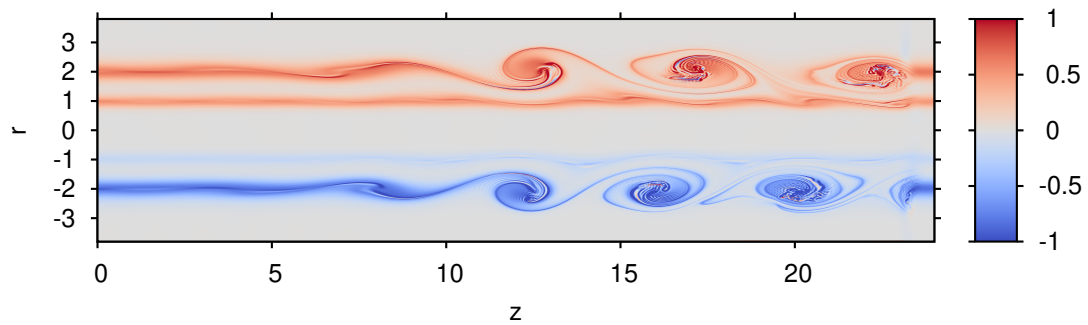
(c) Vorticity $\mathbf{w}$.

coaxial jet are larger allowing the mixing between the species. However as can be
seen not all unstable modes promote the mixing between the species.

Beginning with the different radii ratios Γ for $H_2 - O_2$ configuration, it is important
to remember that traces of absolute instability were observed and the HOS confirms
the different behavior of this binary configuration.

Figure 6.10 - Vortical structures of coaxial homogeneous jet using density contour for velocity ratio $h = 0.5$ and $\Gamma = 2$, to shown the interference between the two unstable modes. For $r > 0$ is used the frequency that produces an almost null growth rate of the first mode and for $r < 0$ is used the frequency that produces the maximum growth rate of the first mode.
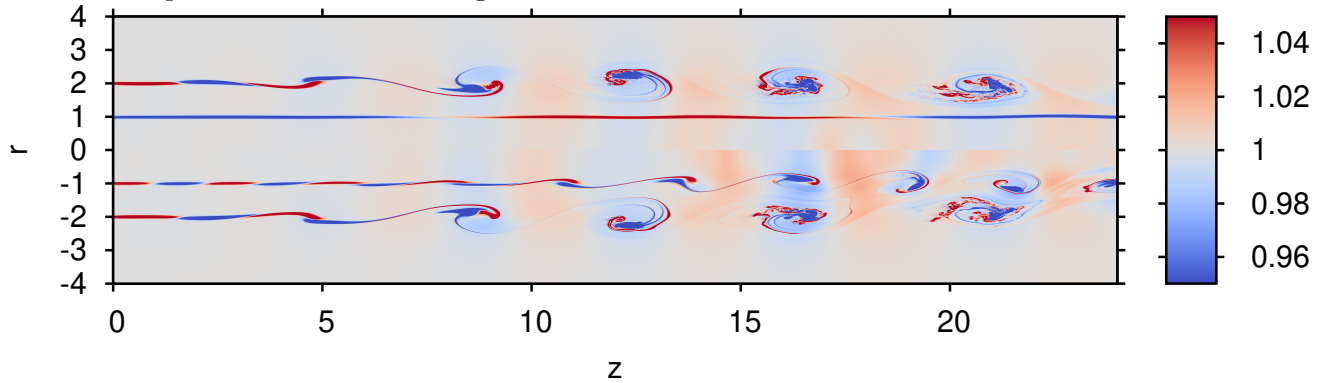
Figure 6.11 - Vortical structures of coaxial homogeneous jet using density contour for velocity ratio $h = 0.5$, evaluated at the maximum amplification frequency for both modes. To show the interference between the two unstable modes, with $\Gamma = 2$.
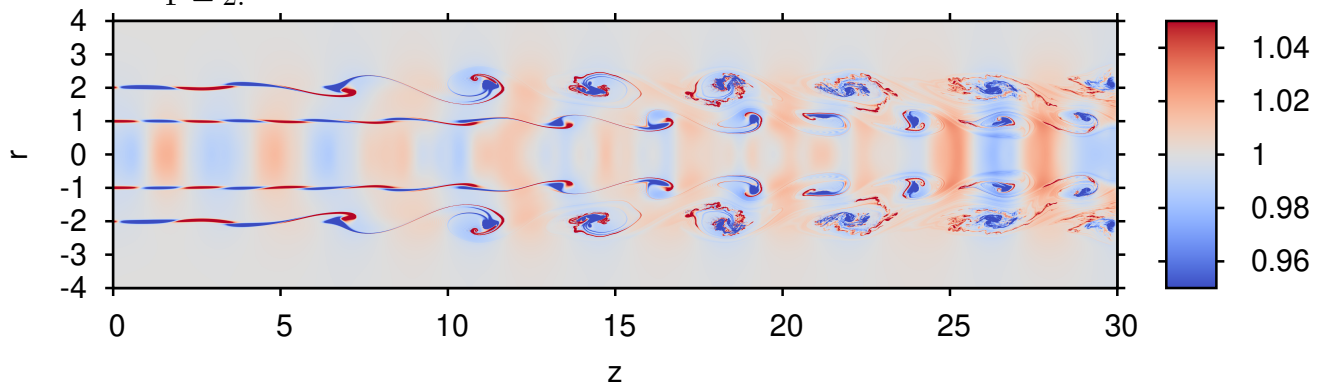
The first relevant case is the $\Gamma = 2.0$ with higher amplification rates for Mode II in relation to the homogeneous cases. In Figure 6.12 the mass fraction contours and the density contours of this configuration are shown using the axial symmetry of the coaxial jet. For $r > 0$ the mass fraction of the inner specie is plotted and for $r < 0$ the density is placed for the same time. This is done in order to compare with the homogeneous cases when the density contours were presented.

Figure 6.12 - Mass fraction contours and density contours, showing the vortical structures for $H_2 - O_2$ coaxial jet at $t = 50$. Mass fraction contours are shown for $r > 0$ and density contour for $r < 0$. The radii and velocity ratios used were $\Gamma = 2$ $h = 0.7$, respectively.

Figure 6.13 - Mass fraction contours and density contours, showing the vortical structures for $H_2 - O_2$ coaxial jet at $t = 70$. Mass fraction contours are shown for $r > 0$ and density contour for $r < 0$. The radii and velocity ratios used were $\Gamma = 2$ $h = 0.7$, respectively.
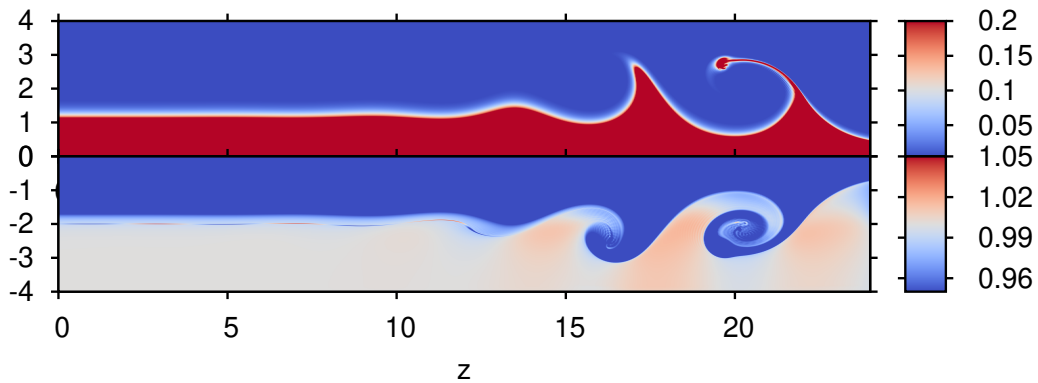
In Figure 6.12 the different behavior of the vortical structures in relation to the homogeneous cases is evident. These structures are larger and more developed, but these are not developed only in space and are not bounded for all points in z direction, Figure 6.13, as in a convective instability. Nonetheless, these structures are not stationary and not only grow in time for all points in space, as in absolute instability.

86

Figure 6.13 along with Figure 6.12, where the same case is illustrated but in a later time, shows that there are not a bounded instability for all spatial points. Concluding that this case is in the limiting region of the absolute and convective instability. It is important to highlight that for $z < 10$ in Figures 6.13 and 6.12 this behavior is not observed. This is due to the small magnitude used in the acoustic pulse that excite the shear layer in relation to the other cases simulated. It allows a linear growth of the instabilities, a larger magnitude of the acoustic pulse leads to a faster transition of this configuration. Then, with a weak acoustic pulse the response of the shear layer is not observer for $z < 10$.

An absolute stability analysis must be conducted in order to verify the conditions resulting in absolute instability.

It is interesting to note in Figures 6.12 and 6.13 how the mass fraction of the inner species jet is mixing by the instabilities with the species of the outer jet, in this case the hydrogen jet is mixed with the oxygen jet. It is the development of the vortical structures that allow the mixing between the reactants in the coaxial injector.

In the same way, a coaxial jet formed by $O_2 - H_2$, with the same radii ratio $\Gamma = 2.0$ and the velocity ratio $h = 0.7$ was simulated, as shown in Figure 6.14. As was expected the inner shear layer is almost stable, although the LST analysis has shown that this is an unstable shear layer but its small growth rates are not captured by the HOS. The outer shear layer is unstable and its growth is captured by the HOS. This is the only mode that allows the mixing between the species in $O_2 - H_2$ configuration. The mixing is due to the growth of the vortical structures of the second mode when these structures achieve the inner radii, $R_1 = 1$, where in this case the oxygen is found. Although this configuration allows the mixing between the species, the amount of oxygen that left the inner jet is very small compared with the previous case and it depends completely on the growing of Mode II.

It is important to note that, as shown in the LST, there is no traces of absolute instabilities and the density contours in Figure 6.14 for $r < 0$, are similar to the homogeneous cases.

Figure 6.14 - Mass fraction contours and density contours, showing the vortical structures for $O_2 - H_2$ coaxial jet at $t = 70$. Mass fraction contours are shown for $r > 0$ and density contour for $r < 0$. The radii and velocity ratios used were $\Gamma = 2$ $h = 0.7$, respectively.
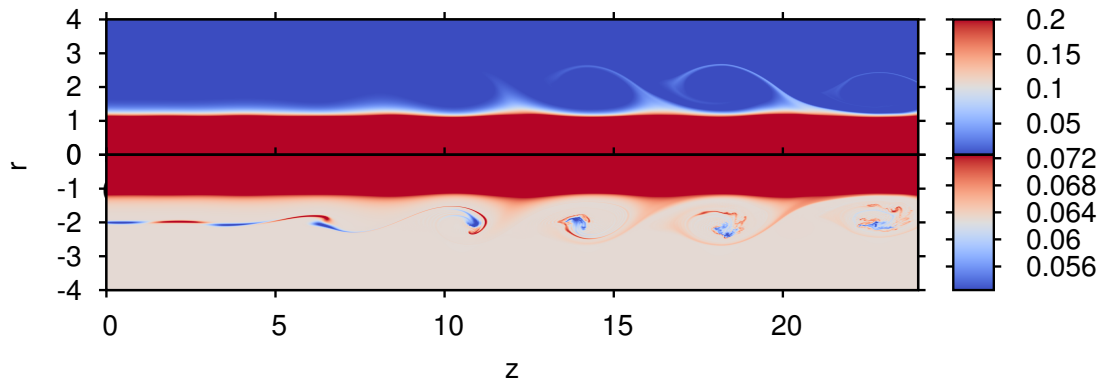
When the radii ratio is larger, $\Gamma = 3.0$ or $\Gamma = 4.0$, the growth rates of the inner mode are larger by the reduction of the confinement cause by the outer jet. The second mode decrease its amplification, being smaller with a larger Γ ratio. Therefore, the case of $H_2 - O_2$ with $\Gamma = 3.0$ was simulated and the result is presented in Figure 6.15. The possibles effects of absolute instability are also present in this case, as in all binary cases with $H_2 - O_2$ configuration, however they are not so pronounced as with $\Gamma = 2.0$. Although the inner mode has larger amplification rates they are not relevant to the mixing process. In the homogeneous cases the inner rates also shown little relevance in the formation of the unstable waves.

For $O_2 - H_2$ the configurations with $\Gamma = 3.0$ or $\Gamma = 4.0$ are not interesting cases because increasing the radii ratio the growth rates of the second instability mode are reduced and it remains unaltered for the first mode in values that are not relevant for the mixing process.

Nonetheless, there is one configuration of $O_2 - H_2$ that was not considered in the LST Chapter 5 and in the homogeneous HOS section, that could be important for the mixing process. It is the case with radii ratio $\Gamma = 1.5$. In this case, Mode II induces the mixing by growing inwards towards the inner jet, if the distance between the shear layer is reduced it is expected that instabilities of the second instability mode reaches the inner jet stream. Decreasing to $\Gamma = 1.3$ cause the appearance of only one mode, whose growth rates are not significant.

Figure 6.15 - Mass fraction contours and density contours, showing the vortical structures for $H_2 - O_2$ coaxial jet at $t = 70$. Mass fraction contours are shown for $r > 0$ and density contour for $r < 0$. The radii and velocity ratios used were $\Gamma = 3$ $h = 0.7$, respectively.
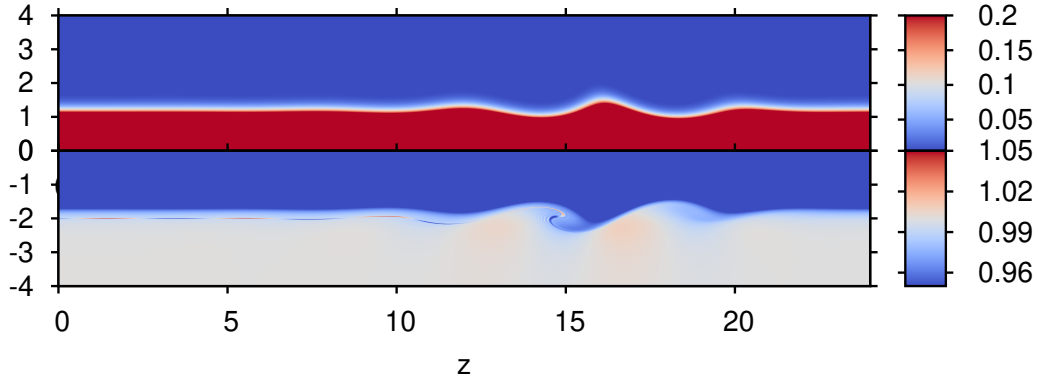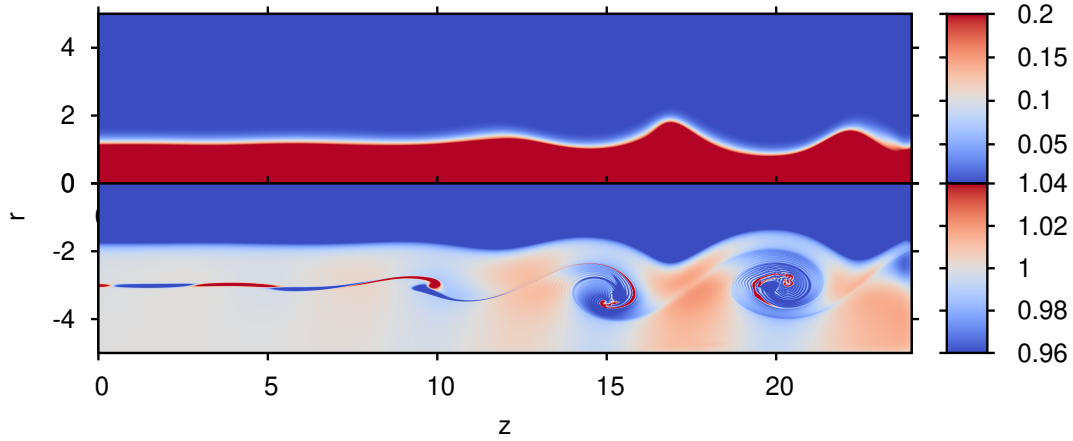

Figure 6.16 shows the mass fraction and density contours of $O_2 - H_2$ with $\Gamma = 1.5$. This figure shows that the external mode, that in this case is closer to the inner jet, takes oxygen to the hydrogen stream more efficiently than in the previous case.

Figure 6.16 - Mass fraction contours and density contours, showing the vortical structures for $O_2 - H_2$ coaxial jet at $t = 70$. Mass fraction contours are shown for $r > 0$ and density contour for $r < 0$. The radii and velocity ratios used were $\Gamma = 1.5$ $h = 0.7$, respectively.
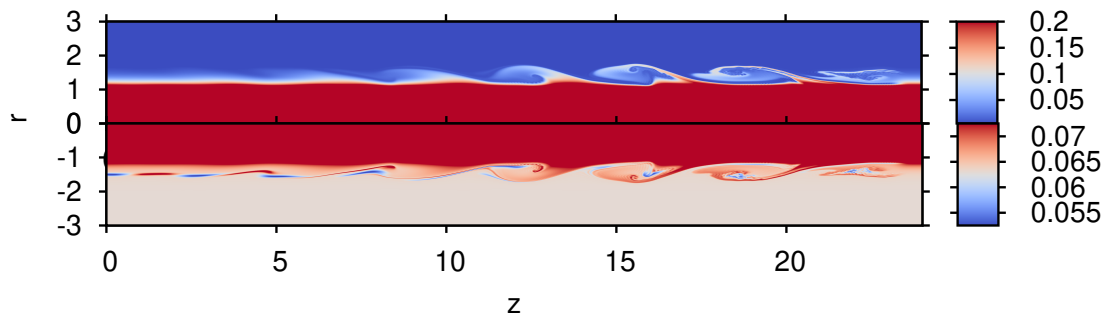
It should be noted that Mode II is apparently confined by the inner stream and its growth is restricted. It may be due to the fact that there is more momentum $(\bar{\rho}\bar{w})$

on the inner jet, formed by oxygen at Mach number $M = 0.6558$. To confirm it a homogeneous case was simulated with $\Gamma = 1.5$ and the result is presented in Figure 6.17. In this figure, the inner mode was not directly exited and only the second mode is present. To this, only one acoustic pulse was used in the inflection point of the second shear layer.

Nonetheless, the fact that there are different species in the coaxial jet apparently does not influence the shape of the vortices, as shown in Figure 6.17. This flattened form of the vortical structures can be explained due to the larger inner jet velocity which deforms the vortical structure when these come close to high stream velocity.

Figure 6.17 - Vortical structures of coaxial homogeneous jet using density contour for velocity ratio $h = 0.7$ with $\Gamma = 1.5$, to shown the interference between the inner jet stream to the second unstable mode, Mode II.
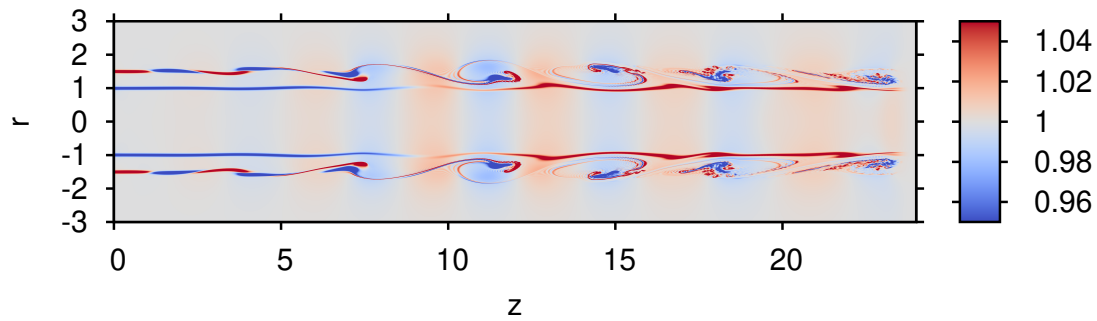
Turning now to the most relevant cases obtained changing the velocity ratio h for the different species configuration.

The first case evaluated was $H_2 - O_2$ with $h = 0.5$ as can be seen in Figure 6.18. This cases is important because it allows growth of both modes, Mode I and Mode II, where Mode II has the largest amplification rates for for all cases tested, including the homogeneous cases, Figure 5.22. In the same way traces of absolute instability are observed as the other $H_2 - O_2$ cases and effectively the vortical structures are developed faster and these are larger than others cases. Figure 6.18 was simulated until time $t = 50$, this is because the HOS does not support the breakdown of the vortices.

Figure 6.18 - Mass fraction contours and density contours, showing the vortical structures for $H_2 - O_2$ coaxial jet at $t = 50$. Mass fraction contours are shown for $r > 0$ and density contour for $r < 0$. The radii and velocity ratios used were $\Gamma = 2.0$ $h = 0.5$, respectively.
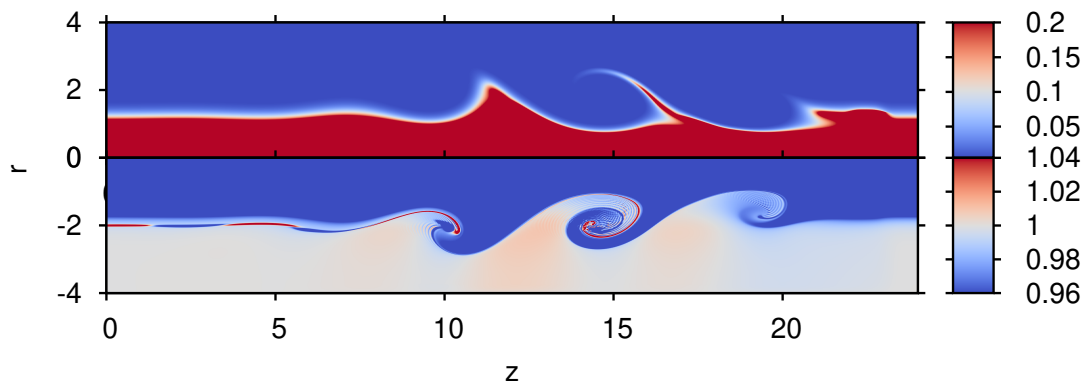
One important point to discuss is that the first instability mode, Mode I, does not appear in none of the $H_2 - O_2$ cases that were simulated. In the simulation of homogeneous coaxial jet when the velocity radio was $h = 0.5$ both unstable modes were present with $\Gamma = 2.0$, Figure 6.11. Although the first instability mode exits is amplification rate was no sufficient to form the K-H instabilities waves. This is clear in Figure 6.18, where Mode I does not appear due to the confinement effects making it smaller than the homogeneous counterpart.

To see how the inner mode can lead to the mixing of the coaxial jet species and as was shown in the LST section, the confinement effects are reduce if the radii ratio Γ is increased. Then a simulation with $H_2 - O_2$ configuration at velocity ratio $h = 0.5$ and radii ratio $\Gamma = 4$ were perform and is presented in Figure 6.19. This velocity ratio promotes the growth of the inner mode but its amplification rate is not so pronounced to transport hydrogen of the inner jet stream to the outer oxygen stream. In Figure 6.19 it is difficult to see, but Mode II is present, growing slower due to its lower phase velocity, but this mode only acts in the oxygen species, as in homogeneous cases.

Figure 6.19 - Mass fraction contours and density contours, showing the vortical structures for $H_2 - O_2$ coaxial jet at $t = 70$. Mass fraction contours are shown for $r > 0$ and density contour for $r < 0$. The radii and velocity ratios used were $\Gamma = 4.0$ $h = 0.5$, respectively.
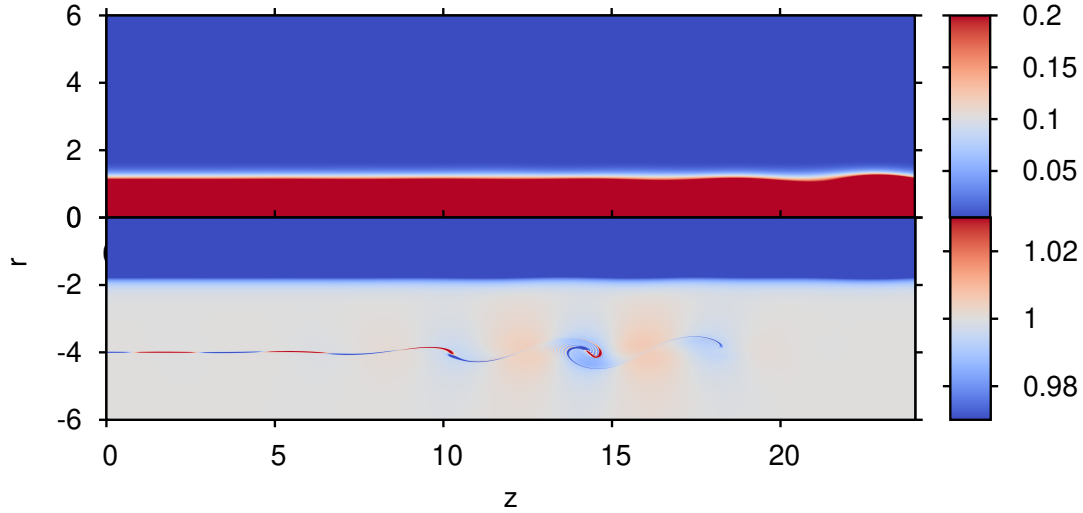
To finished the HOS and looking for the improvement of mixing between species, the $O_2 - H_2$ with lower velocity ration $h = 0.5$ and with the radii ratio $\Gamma = 2$ was simulated. This radii ratio was chosen because in this configuration the confinement effects are not so pronounced and the outer mode has the largest growth rate. The inner mode has smaller growth rates, as can be seen in the LST section and specifically in Figure 5.19, and as was shown in later HOS, amplification rates smaller than $-k_i = 0.1$ are waves that grow very little.

Therefore in the $O_2 - H_2$ arrangement with $h = 0.5$ and $\Gamma = 2.0$ is expected that the growing of Mode II leads to mix of the gases. Figure 6.20 shows as the outer mode transport the oxygen situated in the inner jet, it happens when the vortical structures formed by the velocity gradients in the hydrogen outer shear layer reach the inner stream. However this configuration is similar to the case already simulated of $O_2 - H_2$ with $h = 0.7$, Figure 6.14, since the second mode is not modified by the velocity ratio, but shows that the results of HOS and LST are consistent.

Figure 6.20 - Mass fraction contours and density contours, showing the vortical structures for $O_2 - H_2$ coaxial jet at $t = 70$. Mass fraction contours are shown for $r > 0$ and density contour for $r < 0$. The radii and velocity ratios used were $\Gamma = 2.0$ $h = 0.5$, respectively.
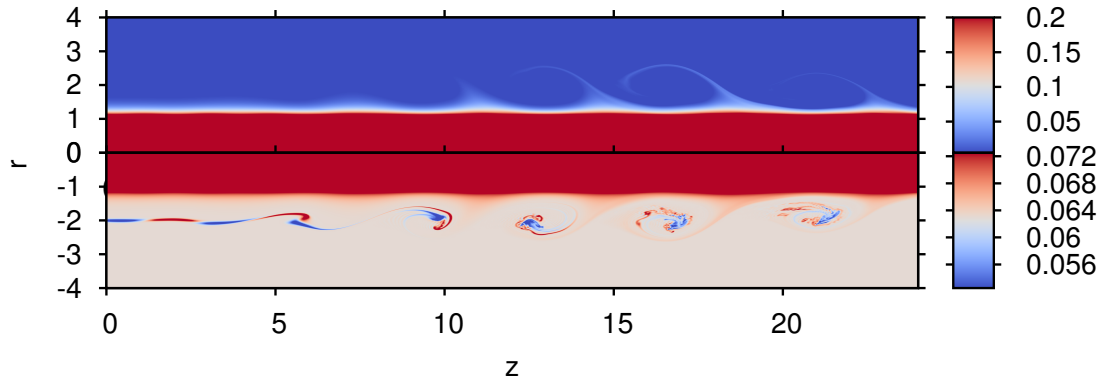
7 CONCLUSION AND FUTURE WORKS

7.1 Conclusions

This work had as main objective the understanding of the stability characteristics of axisymmetric coaxial jets composed of different gases, specifically hydrogen and oxygen. To analyze the stability characteristics of coaxial binary jets the Linear Stability Theory and High Order Simulation approaches were used.

The Linear Stability theory (LST) using the linear Euler equations and assuming normal modes solutions, allowed to understand the principal role of the species in the stability properties of the of coaxial jet, when the position of the species is varied between the inner jet and the outer jet. Coaxial jets have two unstable modes which are the result of the different shear layers that composes it, one between the inner and outer jet and the other formed by the outer jet and the ambient, Mode I and Mode II, respectively

The cases where the hydrogen was used as species in the inner jet $H_2 - O_2$ the amplification rates of Mode II are larger than the homogeneous coaxial jet, contrarily to what happens in $O_2 - H_2$ configuration where the amplification rates are smaller than the homogeneous case. This agreed with the previous studies in a binary mixing layer, in which when the heavier species is in the lower velocity stream the amplification rates are larger, and vice versa.

However For Mode I, the binary mixing layer results can not be extrapolated for a coaxial binary jet, once the confinement effect, caused by the finite quantity of species that can be place in the inner jet, plays an important role. This effect reduces the amplification rates, which are smaller than the homogeneous cases, however the $H_2 - O_2$ configuration was shown to be more unstable than $O_2 - H_2$ configuration.

Using a low Mach number formulation, the compressible effects were neglected with the intention to show in the Less and Lin equation where is the role of the species in the stability properties, which was called inertial effects. This formulation together with the compressible formulation also allows to understand the compressible effects cause by the different speed of sound of the species.

In the results, the use of the hydrogen, where the speed of sound is almost 4 times the oxygen speed of sound allows that the compressible effects, that reduce the amplification rates, to not be so pronounced. This was more evident in $O_2 - H_2$ configuration that may be considered as low Mach number case, due to fact that the

hydrogen composes the outer jet and the ambient where the coaxial jet is ejected. Then, for the outer shear layer formed only by hydrogen the compressible effects are negligible. For the inner jet the mere use of hydrogen also reduced the compressible effects.

Previous works in coaxial jets has shown that there are two parameter that control the the unstable modes of coaxial homogeneous jet, the velocity ratio h and the radii ratio Γ, controlling Mode I and Mode II, respectively. This parameters were changed with the species configuration, all with the intention to understand the role of species in the unstable modes of coaxial jet.

The changes in the radii ratio Γ in $H_2 - O_2$ binary system modify the growth rates for both unstable modes, contrarily to the homogeneous coaxial jet where it modifies exclusively Mode II. In these cases, Mode II decrease with larger Γ ratios like the homogeneous case, but for Mode I highers radii ratios allows to dismiss part of the confinement effects increasing its amplification rates, but these are still smaller than the homogeneous case.

For $O_2 - H_2$ configuration the role of the radii ratio is the same as in the homogeneous configuration, modifying solely Mode II, where it decreases its amplification rates with the larger values of Γ. Nonetheless, the growth rates of Mode I are so small that this mode is almost a neutral mode, which travels at the speed of the inner jet.

Turning now to the velocity ratio effects, which for homogeneous coaxial jets exclusively modified Mode I, but for the binary coaxial jet $H_2 - O_2$ configuration modify both unstable modes. The amplification rates of Mode I decrease with larger velocity ratios, and specifically for $h = 0.9$ this mode is almost stable. However, larger growth rates for this mode were achieved with the smaller velocity ratio of $h = 0.5$, it is due to the larger velocity gradients. Putting this together with the decrease of the confinement effects with the larger radii ratios produces the most unstable Mode I for the binary configurations considered, with the lowest phase velocity. Mode II decreases its amplification rates with larger h ratios like the homogeneous case, nonetheless, it is more unstable than the homogeneous case.

For the opposite configuration $O_2 - H_2$ Mode I is almost stable with the larger velocity ratios and the growth rates of Mode II remains unaltered with different velocity ratios.

To have the largest growth rates in both modes for a binary coaxial subsonic jet at Mach number of $M = 0.6558$ the following characteristics must be achieve: For the inner mode, the heavier species, oxygen, must be placed in the slower jet stream together with the smallest velocity ratio of $h = 0.5$ and the largest radii ratio of $\Gamma = 4$ which decrease the confinement effects. For the outer mode, the heavier species must be located in the slower stream together with the smallest velocity ratio of $h = 0.5$ and with the lesser radii ratio of $\Gamma = 2$ which allows having the two unstable modes.

Using High Order Simulations (HOS) of the Euler equation as second way to analyses the stability characteristics of coaxial binary jets, the main results of the LST were simulated in order to view different effects neglected by this theory, as: nonlinearities as modes interact, the used of realistic velocity and and species profiles not based on canonical equations for the base flow and the visualization of the growth of the instabilities.

One important result of this section was the visualization of the Kelvin-Helmholtz structures of both unstable modes of the homogeneous coaxial jet. In previous studies, only the LST was used to study the coaxial jets with these particular velocity profiles. It is interesting to visualize the iteration between the two unstable modes when the growth of inner mode is favored with the lowest velocity ration $h = 0.5$ and the radii ratio $\Gamma = 2.0$, which leads the outer mode to breakdown. Unfortunately, this case is not possible to be evaluated for the binary system due to the smaller amplification rates of the inner mode, ever smaller than homogeneous cases.

The LST has shown that there are different cases where the growth rates of the binary coaxial jet mode may be important to allow the mixing between the species. However as was shown using HOS not all unstable modes promote the mixing between the species.

Other important result of the HOS was to show that not all unstable modes, in special Mode I, with apparent important growth rates calculated with LST, have larger vortical structures which promote the mixing between the species. If the inner mode amplification rates are smaller than $-k_i = 0.1$, these unstable modes grow very little and are not important to the mix of the oxygen and the hydrogen. In these cases the mix between the species depends exclusively on the growth of outer mode, Mode II. The outer mode transport the species situated in the inner jet when the grow of the vortical structures of the outer shear layer reach the inner stream.

The results of HOS of $O_2 - H_2$ configuration allowed to propose that there was one case with a radii ratio of $\Gamma = 1.5$ that favored the gas mixture. In this case, Mode II induces the mixing by growing inwards towards the inner jet, as the distance between the shear layer is reduced the instabilities of the second mode reaches the inner jet stream.

High order simulations of the $H_2 - O_2$ cases with its different velocity ratios and radii ratios allows to evidence by the mass fraction contours that these cases are the most appropriated to mix the oxygen and the hydrogen by the larger development of the vortical structures of the outer mode. As have been seen in LST results the most unstable case of this configuration for Mode II are reached with $h = 0.5$ and $\Gamma = 2.0$ showing how the outer mode transport the hydrogen situated in the inner jet.

To confirm the principles of absolute stability present in $H_2 - O_2$ cases, observed both with LST and HOS it is necessary to conduct and absolute stability analysis. This together with others ideas, in order to improved the study of stability characteristic of binary coaxial jets will be left as future works in the final section.

7.2   Future Works

In this final section the future works that allows the improvement of the stability study of coaxial binary jets will be explore. This future research topics are suggested by the necessity to enhance the results attained and to explore the developed tools in other research areas.

- Low Mach number coaxial binary jets: In this work it had been shown the inertial and the compressible effects on binary coaxial jets, however the diffusion effects both of momentum and the species would have a important role in the stability characteristics of a low speed coaxial jet. This implies in the development of a Low Mach number code or application of a Preconditioning scheme which also allows to does not use the coflow in HOS.

- Acoustics properties of binary high speed coaxial jets. It was shown by Perrault-Joncas and Maslowe (2008) that acoustic effects do not play an important role on coaxial homogeneous jets above of Mach=0.8. Simulation a this speed implies in the use of the appropriated non reflecting boundary condition in the LST code and in the HOS. The acoustic modes do not

decrease in an exponential form at the boundaries.

- Azimuthal perturbation over binary coaxial jets. This work has shown the characteristics of axisymmetric coaxial jets, but the azimuthal perturbation were neglected. To have one more dimension implies in a higher computation cost of the simulation. Today the code is implemented in a supercomputer which allows to work with three-dimensional effects. This dimension also allows to study the breakdown of the vortices in the non-linear interference cases between the two unstable modes of a coaxial jet.

- Combustion process between species in a coaxial jet. Once the stability characteristic with non reacting binary coaxial jets were study an important topic of research is the combustion process between two species in high pressure regime. The aim is to studied the possible interference between the hydrodynamic and acoustics characteristic with the flame in the combustion chamber of a rocked engine.

REFERENCES

BALESTRA, G.; GLOOR, M.; KLEISER, L. Absolute and convective instabilities of heated coaxial jet flow. **Physics of Fluids**, v. 27, n. 5, p. 054101, 2015. 6

BERLAND, J.; BOGEY, C.; BAILLY, C. Low-dissipation and low-dispersion fourth-order runge–kutta algorithm. **Computers and Fluids**, Elsevier, v. 35, n. 10, p. 1459–1463, 2006. 71

BOGEY, C.; BAILLY, C. A family of low dispersive and low dissipative explicit schemes for flow and noise computations. **Journal of Computational Physics**, Elsevier, v. 194, n. 1, p. 194–214, 2004. 73

CRIGHTON, D.; GASTER, M. Stability of slowly diverging jet flow. **Journal of Fluid Mechanics**, v. 77, n. 2, p. 397–413, 1976. 44

CROW, S. C.; CHAMPAGNE, F. H. Orderly structure in jet turbulence. **Journal of Fluid Mechanics**, v. 48, n. 3, p. 547–591, 1971. Available from: <https://www.cambridge.org/core/article/div-class-title-orderly-structure-in-jet-turbulence-div/8ACC163296714512826DC7F67EBFF91F>. 5, 44

FEDIOUN, I.; LARDJANE, N. Temporal linear stability analysis of three-dimensional compressible binary shear layers. **AIAA journal**, v. 43, n. 1, p. 111–123, 2005. 7

GLOOR, M.; OBRIST, D.; KLEISER, L. Linear stability and acoustic characteristics of compressible, viscous, subsonic coaxial jet flow. **Physics of Fluids**, v. 25, n. 8, 2013. ISSN 10706631. 5, 6, 32, 36

HAIDN, O. J. Advanced rocket engines. **Advances on Propulsion Technology for High-Speed Aircraft**, v. 1, p. 6–1, 2008. 1

KOZUSKO, F.; GROSCH, C. E.; JACKSON, T. L.; KENNEDY, C. A.; GATSKI, T. B. The structure of variable property, compressible mixing layers in binary gas mixtures. **Physics of Fluids**, v. 8, n. 7, p. 1945–1953, 1996. Available from: <https://doi.org/10.1063/1.869103>. 6

KOZUSKO, F.; LASSEIGNE, D. G.; GROSCH, C. E.; JACKSON, T. L. The stability of compressible mixing layers in binary gases. **Physics of Fluids**, v. 8, n. 7, p. 1954–1963, 1996. Available from: <https://doi.org/10.1063/1.868974>. 6, 7, 58, 59, 63, 66

KUNDU, P. K.; DOWLING, D. R.; TRYGGVASON, G.; COHEN, I. M. **Fluid mechanics**. [S.l.: s.n.], 2015. 14

LAW, C. K. **Combustion physics**. [S.l.: s.n.], 2010. 17

LEES, L.; LIN, C. C. Investigation of the stability of the laminar boundary layer in a compressible fluid. **NACA Technical Note**, v. 1115, 1946. Available from: <http://authors.library.caltech.edu/457/>. 26

MANCO, J. A. A. **Condições de contorno não reflexivas para simulação numérica direta de instabilidade de kelvin-helmhotz em escoamento compressível**. Master Thesis (Dissertação Mestrado em Combustão e Propulsão) — Instituto Nacional de Pesquisas Espaciais (INPE), São José dos Campos, 2014. 7, 73

MANCO, J. A. A.; FREITAS, R. B.; FERNANDES, L. M.; MENDONCA, M. T. Stability of compressible mixing layers modified by wakes and jets. **Procedia IUTAM**, v. 14, p. 129 – 136, 2015. 7

MASON, J. C.; HANDSCOMB, D. C. **Chebyshev polynomials**. [S.l.: s.n.], 2002. 37

MICHALKE, A. Survey on jet instability theory. **Progress in Aerospace Sciences**, v. 21, p. 159 – 199, 1984. ISSN 0376-0421. Available from: <http://www.sciencedirect.com/science/article/pii/0376042184900058>. 5, 32

MONKEWITZ, P. A.; SOHN, K. Absolute instability in hot jets. **AIAA journal**, v. 26, n. 8, p. 911–916, 1988. 5

MORELAND, K. Diverging color maps for scientific visualization. In: BEBIS, G.; BOYLE, R.; PARVIN, B.; KORACIN, D.; KUNO, Y.; WANG, J.; PAJAROLA, R.; LINDSTROM, P.; HINKENJANN, A.; ENCARNAÇÃO, M. L.; SILVA, C. T.; COMING, D. (Ed.). **Advances in Visual Computing**. Berlin, Heidelberg: [s.n.], 2009. p. 92–103. ISBN 978-3-642-10520-3. 79

MORRIS, P. J. The instability of high speed jets. **International Journal of Aeroacoustics**, v. 9, n. 1, p. 1–50, 2010. ISSN 1475-472X. 32

_____. _____. **International Journal of Aeroacoustics**, v. 9, n. 1, p. 1–50, 2010. ISSN 1475-472X. 33

PAPAMOSCHOU, D. New method for jet noise reduction in turbofan engines. **AIAA journal**, v. 42, n. 11, p. 2245–2253, 2004. 44

PERRAULT-JONCAS, D.; MASLOWE, S. A. Linear stability of a compressible coaxial jet with continuous velocity and temperature profiles. **Physics of Fluids**, v. 20, n. 7, p. 1–10, 2008. ISSN 10706631. xv, 5, 6, 7, 32, 43, 44, 45, 50, 51, 55, 78, 98

SALEMI, L.; MENDONCA, M. T. Spatial and temporal linear stability analysis of binary compressible shear layer. In: **Proceedings 38th FLUIDS DYNAMICS AIAA CONFERENCE**. Seattle, USA: [s.n.], 2008. (AIAA paper 2008-3841), p. 1–23. 7

SALEMI, L. C. **Análise de Estabilidade Linear de Camada de Mistura Compressível Binária**. 216 p. Master Thesis (Dissertação Mestrado em Combustão e Propulsão) — Instituto Nacional de Pesquisas Espaciais (INPE), São José dos Campos, 2006. 7

SCHUMAKER, S.; DRISCOLL, J. Mixing lengths of coaxial jets in a rocket combustor configuration using acetone plif. In: **Proceedings 43rd JOINT PROPULSION CONFERENCE & EXHIBIT AIAA/ASME/SAE/ASEE**. [S.l.: s.n.], 2007. p. 55–90. 5

SCHUMAKER, S. A.; DRISCOLL, J. F. Mixing properties of coaxial jets with large velocity ratios and large inverse density ratios. **Physics of Fluids**, v. 24, n. 5, p. 55–101, 2012. 5

TALAMELLI, A.; GAVARINI, I. Linear instability characteristics of incompressible coaxial jets. **Flow, Turbulence and Combustion**, v. 76, n. 3, p. 221–240, Apr 2006. ISSN 1573-1987. Available from: <https://doi.org/10.1007/s10494-006-9015-9>. 5

TAM, C. K.; FAN, J. Numerical boundary conditions for computational aeroacoustics benchmark problems. In: **Proceedings. SECOND COMPUTATIONAL AEROACOUSTIC (CAA) WORKSHOP ON BENCHMARK PROBLEMS**. [S.l.: s.n.]. v. 1, p. 191–219. 73

TAM, C. K. W.; WEBB, J. C. Dispersion-relation-preserving schemes for computational acoustics. **Computational Physics**, v. 107, n. 184, p. 262–281, September 1993. 71

TANI, H.; TERAMOTO, S.; OKAMOTO, K. Effects of injector geometry on cryogenic shear coaxial jets at supercritical pressures. **Journal of Propulsion and Power**, v. 31, n. 3, p. 883–888, 2015. 5

TREFETHEN, L. N. **Spectral Methods in Matlab**. [S.l.: s.n.], 2000. 184 p. ISSN 0586-7614. ISBN 9780898714654. 40

WASISTHO, B.; GEURTS, B. J.; KUERTEN, J. G. M. Simulation techniques for spacially evolving instabilities in compressible flow over a flat plate. **Computers and Fluids**, v. 26, n. 7, p. 713–739, March 1997. 71, 72

YU, M. H.; MONKEWITZ, P. A. The effect of nonuniform density on the absolute instability of two dimensional inertial jets and wakes. **Physics of Fluids A: Fluid Dynamics**, v. 2, n. 7, p. 1175–1181, 1990. Available from: <https://doi.org/10.1063/1.857618>. 60

APPENDIX A - CYLINDRICAL COORDINATES

The direct and inverse transformation between cylindrical and cartesian of coordinates expressed by:

$$r = \sqrt{x^2 + y^2} \quad x = r cos(\theta), \tag{A.1}$$

$$\theta = tan^{-1}\left(\frac{y}{x}\right) \quad y = r sin(\theta), \tag{A.2}$$

$$z = z \qquad z = z. \tag{A.3}$$

A position vector in cylindrical coordinates is given:

$$\mathbf{p} = r\mathbf{e}_r + z\mathbf{e}_z. \tag{A.4}$$

The unit vectors in cylindrical coordinates in function of cartesian coordinates are:

$$\mathbf{e}_r = \frac{\mathbf{r}}{|\mathbf{r}|} = \frac{x\mathbf{e}_i + y\mathbf{e}_j}{|\mathbf{r}|} = cos(\theta)\mathbf{e}_i + sin(\theta)\mathbf{e}_j, \tag{A.5}$$

$$\mathbf{e}_\theta = \mathbf{e}_r \times \mathbf{e}_z = cos(\theta)\mathbf{e}_i \times \mathbf{e}_z + sin(\theta)\mathbf{e}_j \times \mathbf{e}_z = cos(\theta)\mathbf{e}_j - sin(\theta)\mathbf{e}_i \tag{A.6}$$

and

$$\mathbf{e}_z = \mathbf{e}_k. \tag{A.7}$$

A differential of line in cylindrical coordinates can be is defined by:

$$d\mathbf{p} = d(r\mathbf{e}_r + z\mathbf{e}_z) = \mathbf{e}_r dr + r d(\mathbf{e}_r) + \mathbf{e}_z dz + z d(\mathbf{e}_z), \tag{A.8}$$

expanding,

$$dp = \mathbf{e}_r dr + r \left(\frac{\partial \mathbf{e}_r}{\partial r} dr + \frac{\partial \mathbf{e}_r}{\partial \theta} d\theta + \frac{\partial \mathbf{e}_r}{\partial z} dz \right) + \mathbf{e}_z dz + z \left(\frac{\partial \mathbf{e}_z}{\partial r} dr + \frac{\partial \mathbf{e}_z}{\partial \theta} d\theta + \frac{\partial \mathbf{e}_z}{\partial z} dz \right)$$

$$\text{(A.9)}$$

and simplified

$$d\mathbf{p} = \mathbf{e}_r dr + r \left(\frac{\partial \mathbf{e}_r}{\partial \theta} d\theta \right) + \mathbf{e}_z dz \qquad \text{(A.10)}$$

$$\frac{\partial \mathbf{e}_r}{\partial \theta} = -sin(\theta)\mathbf{e}_i + cos(\theta)\mathbf{e}_j = \mathbf{e}_\theta. \qquad \text{(A.11)}$$

Using the definition of the $\mathbf{e}_\theta$ unit vectors A.6,

$$d\mathbf{p} = \mathbf{e}_r dr + \mathbf{e}_\theta r d\theta + \mathbf{e}_z dz, \qquad \text{(A.12)}$$

which show that $\mathbf{e}_\theta$ is the derivative of $\mathbf{e}_r$ in the θ direction. With this definition is possible to defined the gradient operator in cylindrical coordinates.

Now using a scalar field α, where the gradient will be applied, its differential is written:

$$d\alpha = \frac{\partial \alpha}{\partial r} dr + \frac{\partial \alpha}{\partial \theta} d\theta + \frac{\partial \alpha}{\partial z} dz, \qquad \text{(A.13)}$$

but $d\alpha$ also can defined by:

$$d\alpha = \nabla \cdot d\mathbf{p}. \qquad \text{(A.14)}$$

As using the cylindrical coordinates the gradient operation must be unaltered, them:

$$\nabla(r, \theta, z) \cdot d\mathbf{p} = \frac{\partial \alpha}{\partial r} dr + \frac{\partial \alpha}{\partial \theta} d\theta + \frac{\partial \alpha}{\partial z} dz, \qquad \text{(A.15)}$$

that same as

$$\nabla_r dr + \nabla_\theta r d\theta + \nabla_z dz = \frac{\partial \alpha}{\partial r} dr + \frac{\partial \alpha}{\partial \theta} d\theta + \frac{\partial \alpha}{\partial z} dz. \tag{A.16}$$

Therefore, the gradient operator in cylindrical coordinate is defined by:

$$\nabla(r,\theta,z) = \mathbf{e}_r \frac{\partial \alpha}{\partial r} + \mathbf{e}_\theta \frac{1}{r} \frac{\partial \alpha}{\partial \theta} + \mathbf{e}_z \frac{\partial \alpha}{\partial z}. \tag{A.17}$$

In the same way the divergent operator in cylindrical coordinates can be defined as:

$$\nabla(r,\theta,z) \cdot \boldsymbol{\alpha} = \left(\mathbf{e}_r \frac{\partial}{\partial r} + \mathbf{e}_\theta \frac{1}{r} \frac{\partial}{\partial \theta} + \mathbf{e}_z \frac{\partial}{\partial z} \right) \cdot (\mathbf{e}_r \alpha_r + \mathbf{e}_\theta \alpha_\theta + \mathbf{e}_z \alpha_z) \tag{A.18}$$

As the base vectors are function of the position, the definition is different:

$$\nabla(r,\theta,z) \cdot \boldsymbol{\alpha} = \left(\mathbf{e}_r \frac{\partial}{\partial r} + \mathbf{e}_\theta \frac{1}{r} \frac{\partial}{\partial \theta} + \mathbf{e}_z \frac{\partial}{\partial z} \right) \cdot (\alpha_r \mathbf{e}_r + \alpha_\theta \mathbf{e}_\theta + \alpha_z \mathbf{e}_z,), \tag{A.19}$$

opening

$$\begin{aligned} \nabla(r,\theta,z) \cdot \boldsymbol{\alpha} = &\mathbf{e}_r \cdot \frac{\partial(\alpha_r \mathbf{e}_r)}{\partial r} + \mathbf{e}_r \cdot \frac{\partial(\alpha_\theta \mathbf{e}_\theta)}{\partial r} + \mathbf{e}_r \cdot \frac{\partial(\alpha_z \mathbf{e}_z)}{\partial r} \\ &+ \frac{\mathbf{e}_\theta}{r} \cdot \frac{\partial(\alpha_r \mathbf{e}_r)}{\partial \theta} + \frac{\mathbf{e}_\theta}{r} \cdot \frac{\partial(\alpha_\theta \mathbf{e}_\theta)}{\partial \theta} + \frac{\mathbf{e}_\theta}{r} \cdot \frac{\partial(\alpha_z \mathbf{e}_z)}{\partial \theta} \\ &+ \mathbf{e}_z \cdot \frac{\partial(\alpha_r \mathbf{e}_r)}{\partial z} + \mathbf{e}_z \cdot \frac{\partial(\alpha_\theta \mathbf{e}_\theta)}{\partial z} + \mathbf{e}_z \cdot \frac{\partial(\alpha_z \mathbf{e}_z)}{\partial z}. \end{aligned} \tag{A.20}$$

The Jacobian matrix of the unit vector is also a important operator using in the Navier-Stokes equation and related the all directional derivatives. It can be defined as:

$$\mathbf{J} = \frac{\partial(\mathbf{e}_r, \mathbf{e}_\theta, \mathbf{e}_z)}{\partial(r,\theta,z)} = \begin{bmatrix} \dfrac{\partial \mathbf{e}_r}{\partial r} & \dfrac{\partial \mathbf{e}_\theta}{\partial r} & \dfrac{\partial \mathbf{e}_z}{\partial r} \\ \dfrac{\partial \mathbf{e}_r}{\partial \theta} & \dfrac{\partial \mathbf{e}_\theta}{\partial \theta} & \dfrac{\partial \mathbf{e}_z}{\partial \theta} \\ \dfrac{\partial \mathbf{e}_r}{\partial z} & \dfrac{\partial \mathbf{e}_\theta}{\partial z} & \dfrac{\partial \mathbf{e}_z}{\partial z} \end{bmatrix} = \begin{bmatrix} 0 & 0 & 0 \\ \mathbf{e}_\theta & -\mathbf{e}_r & 0 \\ 0 & 0 & 0 \end{bmatrix} \tag{A.21}$$

Then, using the value of the derivatives in A.20 is getting:

$$\nabla(r, \theta, z) = \frac{1}{r} \left(\frac{\partial(r\alpha_r)}{\partial r} + \frac{\partial \alpha_\theta}{\partial \theta} + \frac{\partial(r\alpha_z)}{\partial z} \right). \tag{A.22}$$

Another important definition useful to transform the Navier-Stokes equation in cartesian coordinates to cylindrical coordinates is the vector product:

$$\nabla \mathbf{u} = \begin{bmatrix} \mathbf{e}_r \dfrac{\partial \alpha}{\partial r} \\[2mm] \mathbf{e}_\theta \dfrac{1}{r} \dfrac{\partial \alpha}{\partial \theta} \\[2mm] \mathbf{e}_z \dfrac{\partial \alpha}{\partial z} \end{bmatrix} \begin{bmatrix} \mathbf{e}_r u & \mathbf{e}_\theta v & \mathbf{e}_z w \end{bmatrix} = \begin{bmatrix} \mathbf{e}_r \dfrac{\partial(\mathbf{e}_r u)}{\partial r} & \mathbf{e}_r \dfrac{\partial(\mathbf{e}_\theta v)}{\partial r} & \mathbf{e}_r \dfrac{\partial(\mathbf{e}_z w)}{\partial r} \\[2mm] \mathbf{e}_\theta \dfrac{1}{r} \dfrac{\partial(\mathbf{e}_r u)}{\partial \theta} & \mathbf{e}_\theta \dfrac{1}{r} \dfrac{\partial(\mathbf{e}_\theta v)}{\partial \theta} & \mathbf{e}_\theta \dfrac{1}{r} \dfrac{\partial(\mathbf{e}_z w)}{\partial \theta} \\[2mm] \mathbf{e}_z \dfrac{\partial(\mathbf{e}_r u)}{\partial z} & \mathbf{e}_z \dfrac{\partial(\mathbf{e}_\theta v)}{\partial z} & \mathbf{e}_z \dfrac{\partial(\mathbf{e}_z w)}{\partial z} \end{bmatrix}, \tag{A.23}$$

that define the velocity tensor as:

$$\nabla \mathbf{u} = \begin{bmatrix} \mathbf{e}_r \mathbf{e}_r \dfrac{\partial u}{\partial r} & \mathbf{e}_r \mathbf{e}_\theta \dfrac{\partial v}{\partial r} & \mathbf{e}_r \mathbf{e}_z \dfrac{\partial w}{\partial r} \\[2mm] \mathbf{e}_\theta \dfrac{1}{r} \dfrac{\partial(\mathbf{e}_r u)}{\partial \theta} & \mathbf{e}_\theta \dfrac{1}{r} \dfrac{\partial(\mathbf{e}_\theta v)}{\partial \theta} & \mathbf{e}_\theta \mathbf{e}_z \dfrac{1}{r} \dfrac{\partial w}{\partial \theta} \\[2mm] \mathbf{e}_z \mathbf{e}_r \dfrac{\partial u}{\partial z} & \mathbf{e}_z \mathbf{e}_\theta \dfrac{\partial v}{\partial z} & \mathbf{e}_z \mathbf{e}_z \dfrac{\partial w}{\partial z} \end{bmatrix}. \tag{A.24}$$

expanding and simplifying:

$$\nabla \mathbf{u} = \begin{bmatrix} \dfrac{\partial u}{\partial r} & \dfrac{\partial v}{\partial r} & \dfrac{\partial w}{\partial r} \\[2mm] \left(\dfrac{1}{r} \dfrac{\partial u}{\partial \theta} - \dfrac{v}{r} \right) & \left(\dfrac{1}{r} \dfrac{\partial v}{\partial \theta} + \dfrac{u}{r} \right) & \dfrac{1}{r} \dfrac{\partial w}{\partial \theta} \\[2mm] \dfrac{\partial u}{\partial z} & \dfrac{\partial v}{\partial z} & \dfrac{\partial w}{\partial z} \end{bmatrix}. \tag{A.25}$$

Similarly their transposed is given by:

$$(\nabla \mathbf{u})^T = \begin{bmatrix} \dfrac{\partial u}{\partial r} & \left(\dfrac{1}{r}\dfrac{\partial u}{\partial \theta} - \dfrac{v}{r}\right) & \dfrac{\partial u}{\partial z} \\[3mm] \dfrac{\partial v}{\partial r} & \left(\dfrac{1}{r}\dfrac{\partial v}{\partial \theta} + \dfrac{u}{r}\right) & \dfrac{\partial v}{\partial z} \\[3mm] \dfrac{\partial w}{\partial r} & \dfrac{1}{r}\dfrac{\partial w}{\partial \theta} & \dfrac{\partial w}{\partial z} \end{bmatrix} \tag{A.26}$$

A.1   Stress Tensor Cylindrical Coordinates

The Navier-Stokes stress tensor is given by

$$\boldsymbol{\tau} = -\lambda(\nabla \cdot \mathbf{u})\boldsymbol{I} + \mu\left(\nabla\mathbf{u} + (\nabla\mathbf{u})^T\right) \tag{A.27}$$

or in matrix form by:

$$\boldsymbol{\tau} = \begin{bmatrix} \tau_{rr} & \tau_{r\theta} & \tau_{rz} \\[2mm] \tau_{\theta r} & \tau_{\theta\theta} & \tau_{\theta z} \\[2mm] \tau_{zr} & \tau_{z\theta} & \tau_{zz} \end{bmatrix} \tag{A.28}$$

As the vectors operator change in cylindrical coordinates, the stress tensor too and their terms are expressed as:

$$(\nabla \cdot \mathbf{u})\boldsymbol{I} = \left[\frac{1}{r}\left(\frac{\partial(ru)}{\partial r} + \frac{\partial v}{\partial \theta} + \frac{\partial(rw)}{\partial z}\right)\right]\begin{bmatrix} 1 & 0 & 0 \\ 0 & 1 & 0 \\ 0 & 0 & 1 \end{bmatrix} \tag{A.29}$$

$$\tau_{rr} = \lambda\left[\frac{1}{r}\left(\frac{\partial(ru)}{\partial r} + \frac{\partial v}{\partial \theta} + \frac{\partial(rw)}{\partial z}\right)\right] + 2\mu\frac{\partial u}{\partial r} \tag{A.30}$$

$$\tau_{\theta\theta} = \lambda\left[\frac{1}{r}\left(\frac{\partial(ru)}{\partial r} + \frac{\partial v}{\partial \theta} + \frac{\partial(rw)}{\partial z}\right)\right] + 2\mu\left(\frac{1}{r}\frac{\partial v}{\partial \theta} + \frac{u}{r}\right) \tag{A.31}$$

$$\tau_{zz} = \lambda\left[\frac{1}{r}\left(\frac{\partial(ru)}{\partial r} + \frac{\partial v}{\partial \theta} + \frac{\partial(rw)}{\partial z}\right)\right] + 2\mu\frac{\partial w}{\partial z} \tag{A.32}$$

$$\tau_{r\theta} = \tau_{\theta r} = \mu \left(\frac{1}{r}\frac{\partial u}{\partial \theta} + \frac{\partial v}{\partial r} - \frac{v}{r} \right) \tag{A.33}$$

$$\tau_{rz} = \tau_{zr} = \mu \left(\frac{\partial w}{\partial r} + \frac{\partial u}{\partial z} \right) \tag{A.34}$$

$$\tau_{\theta z} = \tau_{z\theta} = \mu \left(\frac{1}{r}\frac{\partial w}{\partial \theta} + \frac{\partial v}{\partial z} \right) \tag{A.35}$$

A quantity important to define in cylindrical coordinates and using in the conservation energy equation is the double dot product between the stress tensor and the gradient of the velocity, given by:

$$\begin{aligned}
\boldsymbol{\tau} : \nabla \mathbf{u} = {}& \tau_{rr}\frac{\partial u}{\partial r} + \tau_{\theta\theta}\left(\frac{1}{r}\frac{\partial v}{\partial \theta} + \frac{u}{r} \right) + \tau_{zz}\frac{\partial w}{\partial z} + \\
& \tau_{\theta r}\left(\frac{1}{r}\frac{\partial u}{\partial \theta} + \frac{\partial v}{\partial r} - \frac{v}{r} \right) + \tau_{\theta z}\left(\frac{1}{r}\frac{\partial w}{\partial \theta} + \frac{\partial v}{\partial z} \right) + \\
& \tau_{rz}\left(\frac{\partial w}{\partial r} + \frac{\partial u}{\partial z} \right).
\end{aligned} \tag{A.36}$$

Finally, a important vector operator that will be used is the Laplace operator ∇^2 applied to a scalar quantity. It is defined as:

$$\nabla^2 \alpha = \frac{1}{r}\frac{\partial \left(r\dfrac{\partial \alpha}{\partial r} \right)}{\partial r} + \frac{1}{r^2}\frac{\partial^2 \alpha}{\partial \theta^2} + \frac{\partial^2 \alpha}{\partial z^2} \tag{A.37}$$

APPENDIX B - MATRIX FORM OF LINEAR NAVIER-STOKES EQUATIONS

The linear Navier-Stokes equation in cylindrical coordinates in two dimension for a parallel flow can be represented as:

$$
\frac{\partial \mathbf{u}'}{\partial t} + \mathbf{A}\frac{\partial \mathbf{u}'}{\partial r} + \mathbf{B}\frac{\partial \mathbf{u}'}{\partial z} + \mathbf{C}\mathbf{u}' +
$$
$$
\frac{1}{Re}\left(\mathbf{D}\frac{\partial^2 \mathbf{u}'}{\partial r^2} + \mathbf{E}\frac{\partial^2 \mathbf{u}'}{\partial z^2} + \mathbf{F}\frac{\partial^2 \mathbf{u}'}{\partial r\partial z} + \mathbf{G}\frac{\partial \mathbf{u}'}{\partial r} + \mathbf{H}\frac{\partial \mathbf{u}'}{\partial z} + \mathbf{I}\mathbf{u}'\right)
$$
$$
+\frac{\gamma_0\gamma_f - 1}{Re}\left(\mathbf{J}\frac{\partial^2 \mathbf{u}'}{\partial r^2} + \mathbf{K}\frac{\partial^2 \mathbf{u}'}{\partial z^2} + \mathbf{L}\frac{\partial \mathbf{u}'}{\partial r} + \mathbf{M}\frac{\partial \mathbf{u}'}{\partial z} + \mathbf{N}\right) + \qquad \text{(B.1)}
$$
$$
\frac{\gamma_j(\gamma_0\gamma_f - 1)}{Pe}\left(\mathbf{O}\frac{\partial^2 \mathbf{u}'}{\partial r^2} + \mathbf{P}\frac{\partial^2 \mathbf{u}'}{\partial z^2} + \mathbf{Q}\frac{\partial \mathbf{u}'}{\partial r} + \mathbf{R}\frac{\partial \mathbf{u}'}{\partial z} + \mathbf{S}\right)
$$
$$
+\frac{1}{Pe}\left(\mathbf{T}\frac{\partial^2 \mathbf{u}'}{\partial r^2} + \mathbf{U}\frac{\partial^2 \mathbf{u}'}{\partial z^2} + \mathbf{V}\frac{\partial \mathbf{u}'}{\partial r} + \mathbf{W}\frac{\partial \mathbf{u}'}{\partial z} + \mathbf{X}\right) = 0.
$$

The matrices that composes it system are

$$
\mathbf{A} = \begin{bmatrix} 0 & \bar\rho & 0 & 0 & 0 & 0 \\ 0 & 0 & 0 & 1/\bar\rho & 0 & 0 \\ 0 & 0 & 0 & 0 & 0 & 0 \\ 0 & \bar\gamma P & 0 & 0 & 0 & 0 \\ 0 & 0 & 0 & 0 & 0 & 0 \\ 0 & 0 & 0 & 0 & 0 & 0 \end{bmatrix}
\mathbf{B} = \begin{bmatrix} \bar W & 0 & \bar\rho & 0 & 0 & 0 \\ 0 & \bar W & 0 & 0 & 0 & 0 \\ 0 & 0 & \bar W & 1/\bar\rho & 0 & 0 \\ 0 & 0 & \bar\gamma P & \bar W & 0 & 0 \\ 0 & 0 & 0 & 0 & \bar W & 0 \\ 0 & 0 & 0 & 0 & 0 & \bar W \end{bmatrix}
\mathbf{C} = \begin{bmatrix} 0 & C_\rho & 0 & 0 & 0 & 0 \\ 0 & 0 & 0 & 0 & 0 & 0 \\ 0 & d\bar W/dr & 0 & 0 & 0 & 0 \\ 0 & C_u & 0 & 0 & 0 & 0 \\ 0 & d\bar Y_1/dr & 0 & 0 & 0 & 0 \\ 0 & d\bar Y_2/dr & 0 & 0 & 0 & 0 \end{bmatrix}
$$

$$\text{(B.2)}$$

$$
\mathbf{D} = \begin{bmatrix} 0 & 0 & 0 & 0 & 0 & 0 \\ 0 & D_u & 0 & 0 & 0 & 0 \\ 0 & 0 & \bar\mu & 0 & 0 & 0 \\ 0 & 0 & 0 & 0 & 0 & 0 \\ 0 & 0 & 0 & 0 & 0 & 0 \\ 0 & 0 & 0 & 0 & 0 & 0 \end{bmatrix}
\mathbf{E} = \begin{bmatrix} 0 & 0 & 0 & 0 & 0 & 0 \\ 0 & \bar\mu & 0 & 0 & 0 & 0 \\ 0 & 0 & E_w & 0 & 0 & 0 \\ 0 & 0 & 0 & 0 & 0 & 0 \\ 0 & 0 & 0 & 0 & 0 & 0 \\ 0 & 0 & 0 & 0 & 0 & 0 \end{bmatrix}
\mathbf{F} = \begin{bmatrix} 0 & 0 & 0 & 0 & 0 & 0 \\ 0 & 0 & F_w & 0 & 0 & 0 \\ 0 & F_u & 0 & 0 & 0 & 0 \\ 0 & 0 & 0 & 0 & 0 & 0 \\ 0 & 0 & 0 & 0 & 0 & 0 \\ 0 & 0 & 0 & 0 & 0 & 0 \end{bmatrix}
$$

$$\text{(B.3)}$$

$$\mathbf{G} = \begin{bmatrix} 0 & 0 & 0 & 0 & 0 & 0 \\ 0 & G_u & 0 & 0 & 0 & 0 \\ 0 & 0 & G_w & 0 & 0 & 0 \\ 0 & 0 & 0 & 0 & 0 & 0 \\ 0 & 0 & 0 & 0 & 0 & 0 \\ 0 & 0 & 0 & 0 & 0 & 0 \end{bmatrix} \mathbf{H} = \begin{bmatrix} 0 & 0 & 0 & 0 & 0 & 0 \\ 0 & 0 & H_w & 0 & 0 & 0 \\ 0 & H_u & 0 & 0 & 0 & 0 \\ 0 & 0 & 0 & 0 & 0 & 0 \\ 0 & 0 & 0 & 0 & 0 & 0 \\ 0 & 0 & 0 & 0 & 0 & 0 \end{bmatrix} \quad \text{(B.4)}$$

$$\mathbf{I} = \begin{bmatrix} 0 & 0 & 0 & 0 & 0 & 0 \\ 0 & I_u & 0 & 0 & 0 & 0 \\ 0 & 0 & 0 & 0 & 0 & 0 \\ 0 & 0 & 0 & 0 & 0 & 0 \\ 0 & 0 & 0 & 0 & 0 & 0 \\ 0 & 0 & 0 & 0 & 0 & 0 \end{bmatrix} \mathbf{J} = \mathbf{K} = \begin{bmatrix} 0 \end{bmatrix} \quad \text{(B.5)}$$

$$\mathbf{L} = \begin{bmatrix} 0 & 0 & 0 & 0 & 0 & 0 \\ 0 & 0 & 0 & 0 & 0 & 0 \\ 0 & 0 & 0 & 0 & 0 & 0 \\ 0 & 0 & L_w & 0 & 0 & 0 \\ 0 & 0 & 0 & 0 & 0 & 0 \\ 0 & 0 & 0 & 0 & 0 & 0 \end{bmatrix} \mathbf{M} = \begin{bmatrix} 0 & 0 & 0 & 0 & 0 & 0 \\ 0 & 0 & 0 & 0 & 0 & 0 \\ 0 & 0 & 0 & 0 & 0 & 0 \\ 0 & L_w & 0 & 0 & 0 & 0 \\ 0 & 0 & 0 & 0 & 0 & 0 \\ 0 & 0 & 0 & 0 & 0 & 0 \end{bmatrix} \mathbf{N} = \begin{bmatrix} 0 \end{bmatrix} \quad \text{(B.6)}$$

$$\mathbf{O} = \begin{bmatrix} 0 & 0 & 0 & 0 & 0 & 0 \\ 0 & 0 & 0 & 0 & 0 & 0 \\ 0 & 0 & 0 & 0 & 0 & 0 \\ 0 & 0 & 0 & O_p & 0 & 0 \\ 0 & 0 & 0 & 0 & 0 & 0 \\ 0 & 0 & 0 & 0 & 0 & 0 \end{bmatrix} \mathbf{P} = \begin{bmatrix} 0 & 0 & 0 & 0 & 0 & 0 \\ 0 & 0 & 0 & 0 & 0 & 0 \\ 0 & 0 & 0 & 0 & 0 & 0 \\ 0 & 0 & 0 & P_p & 0 & 0 \\ 0 & 0 & 0 & 0 & 0 & 0 \\ 0 & 0 & 0 & 0 & 0 & 0 \end{bmatrix} \mathbf{Q} = \begin{bmatrix} 0 & 0 & 0 & 0 & 0 & 0 \\ 0 & 0 & 0 & 0 & 0 & 0 \\ 0 & 0 & 0 & 0 & 0 & 0 \\ 0 & 0 & 0 & Q_{p1}+Q_{p2} & Q_{y1} & 0 \\ 0 & 0 & 0 & 0 & 0 & 0 \\ 0 & 0 & 0 & 0 & 0 & 0 \end{bmatrix}$$
$$\text{(B.7)}$$

$$\mathbf{R} = \begin{bmatrix} 0 \end{bmatrix} \quad \mathbf{S} = \begin{bmatrix} 0 & 0 & 0 & 0 & 0 & 0 \\ 0 & 0 & 0 & 0 & 0 & 0 \\ 0 & 0 & 0 & 0 & 0 & 0 \\ 0 & 0 & 0 & 0 & 0 & 0 \\ 0 & 0 & 0 & S_{p1}+S_{p2} & 0 & 0 \\ 0 & 0 & 0 & 0 & 0 & 0 \end{bmatrix} \quad \mathbf{T} = \begin{bmatrix} 0 & 0 & 0 & 0 & 0 & 0 \\ 0 & 0 & 0 & 0 & 0 & 0 \\ 0 & 0 & 0 & 0 & 0 & 0 \\ 0 & 0 & 0 & 0 & 0 & 0 \\ 0 & 0 & 0 & 0 & D_{1m} & 0 \\ 0 & 0 & 0 & 0 & 0 & D_{2m} \end{bmatrix} \tag{B.8}$$

$$\mathbf{U} = \mathbf{T} \tag{B.9}$$

$$\mathbf{V} = \begin{bmatrix} 0 & 0 & 0 & 0 & 0 & 0 \\ 0 & 0 & 0 & 0 & 0 & 0 \\ 0 & 0 & 0 & 0 & 0 & 0 \\ 0 & 0 & 0 & 0 & 0 & 0 \\ V_\rho & 0 & 0 & 0 & V_y & 0 \\ V_\rho & 0 & 0 & 0 & 0 & V_y \end{bmatrix} \quad \mathbf{W} = \begin{bmatrix} 0 \end{bmatrix} \quad \mathbf{X} = \begin{bmatrix} 0 & 0 & 0 & 0 & 0 & 0 \\ 0 & 0 & 0 & 0 & 0 & 0 \\ 0 & 0 & 0 & 0 & 0 & 0 \\ 0 & 0 & 0 & 0 & 0 & 0 \\ X_\rho & 0 & 0 & 0 & 0 & 0 \\ X_\rho & 0 & 0 & 0 & 0 & 0 \end{bmatrix} \tag{B.10}$$

In the above matrices were used the following definition:

$$C_\rho \equiv d\bar{\rho}/dr + \bar{\rho}/r \tag{B.11}$$

$$C_u \equiv \frac{\bar{\gamma}_f \bar{p}}{r} \tag{B.12}$$

$$D_u \equiv \bar{\lambda} + 2\bar{\mu} \tag{B.13}$$

$$E_w \equiv \bar{\lambda} + 2\bar{\mu} \tag{B.14}$$

$$E_{spe} \equiv \left(\frac{1}{Le_1} \bar{\mathcal{D}}_{1m} \bar{c}_{p1} - \frac{1}{Le_2} \bar{\mathcal{D}}_{2m} \bar{c}_{p2} \right) \tag{B.15}$$

$$F_u \equiv \bar{\mu} + \bar{\lambda} \tag{B.16}$$

$$F_w \equiv \bar{\lambda} + \bar{\mu} \tag{B.17}$$

$$G_u \equiv 2\frac{\bar{\lambda}}{r} + 2\frac{\partial \bar{\mu}}{\partial r} + \frac{\partial \bar{\lambda}}{\partial r} + 2\frac{1}{r}\bar{\mu} \tag{B.18}$$

$$G_w \equiv \frac{\partial \bar{\mu}}{\partial r} + \frac{1}{r}\bar{\mu} \tag{B.19}$$

113

$$H_u \equiv \frac{\partial \bar{\mu}}{\partial r} + \frac{1}{r}\bar{\mu} + \bar{\lambda}\frac{1}{r} \tag{B.20}$$

$$H_w \equiv \frac{\bar{\lambda}}{r} + \frac{\partial \bar{\lambda}}{\partial r} \tag{B.21}$$

$$I_u \equiv \frac{1}{r}\frac{\partial \bar{\lambda}}{\partial r} \tag{B.22}$$

$$L_w \equiv M_u \equiv \bar{\mu}\frac{\partial \bar{W}}{\partial r} \tag{B.23}$$

$$O_p \equiv P_p \equiv \frac{\bar{k}}{\bar{\rho}R} \tag{B.24}$$

$$Q_{p1} \equiv \frac{1}{\bar{\rho}R}\left(\frac{\partial \bar{k}}{\partial r} + \frac{\bar{k}}{r}\right) \tag{B.25}$$

$$Q_{p2} \equiv E_{spe}\frac{1}{R}\frac{\partial \bar{Y}_1}{\partial r} \tag{B.26}$$

$$Q_{Y_1} \equiv \bar{\rho}\frac{\partial}{\partial r}\left(\frac{\bar{p}}{\bar{\rho}R}\right)E_{spe} \tag{B.27}$$

$$S_\rho \equiv \frac{\partial}{\partial r}\left(\frac{\bar{p}}{\bar{\rho}R}\right)E_{spe}\frac{\partial \bar{Y}_1}{\partial r} \tag{B.28}$$

$$S_{pi} \equiv \bar{\rho}E_{spe}\frac{\partial \bar{Y}_i}{\partial r}\frac{\partial}{\partial r}\left(\frac{1}{R\bar{\rho}}\right) \tag{B.29}$$

$$V_\rho \equiv \frac{\bar{\mathcal{D}}_{mi}}{\bar{\rho}}\frac{\partial \bar{Y}_i}{\partial r} \tag{B.30}$$

$$V_y \equiv \frac{\bar{\mathcal{D}}_{mi}}{\bar{\rho}}\frac{\partial}{\partial r}\bar{\rho} + \frac{\partial}{\partial r}\bar{\mathcal{D}}_{mi} + \frac{1}{r}\bar{\mathcal{D}}_{mi} \tag{B.31}$$

$$X_\rho \equiv \left(\bar{\mathcal{D}}_{mi}\frac{1}{\bar{\rho}}\frac{\partial^2}{\partial r^2}\bar{Y}_i + \frac{1}{\bar{\rho}}\left(\frac{\partial}{\partial r}\bar{\mathcal{D}}_{mi} + \frac{1}{r}\bar{\mathcal{D}}_{mi}\right)\frac{\partial}{\partial r}\bar{Y}_i\right) \tag{B.32}$$